

X-ray spectroscopic investigations of small size-selected Fe_nV_m adsorbates

Dissertation
zur Erlangung des Doktorgrades
an der Fakultät für Mathematik, Informatik und
Naturwissenschaften
Fachbereich Physik
der Universität Hamburg

vorgelegt von
Fridtjof Kielgast

Hamburg
2022

Gutachter der Dissertation:

PD Dr. Michael Martins

Prof. Dr. Nils Huse

Zusammensetzung der Prüfungskommission:

PD Dr. Michael Martins

Prof. Dr. Nils Huse

Prof. Dr. Michael Potthoff

Prof. Dr. Michael Rübhausen

Prof. Dr. Ralf Röhlsberger

Vorsitzende(r) der Prüfungskommission:

Prof. Dr. Michael Potthoff

Datum der Disputation:

29.03.2022

Vorsitzender des Fach-Promotionsausschusses PHYSIK: Prof. Dr. Wolfgang J. Parak

Leiter des Fachbereichs Physik: Prof. Dr. Günter H. W. Sigl

Dekan der Fakultät MIN: Prof. Dr. Heinrich Graener

X-ray spectroscopics investigation of small size-selected Fe_nV_m adsorbates

Abstract

In the course of this work, the electronic and magnetic properties of atomically small, size-selected Fe and V adsorbates deposited onto a non-magnetic Cu(001) substrate were investigated *in situ*. The size of the investigated adsorbates ranged from 1 to 3 atoms and elementally pure as well as alloy clusters were measured. X-ray absorption spectroscopy (XAS) and the X-ray magnetic circular dichroism (XMCD) were chosen as measurement techniques, ensuring non-destructive and element selective determination of the adsorbates' electronic structure and their respective magnetic moments. For the magnetic measurements, the adsorbates were studied in an external magnetic field of 7 T.

For all of the adsorbates, a weak interaction with the substrate was found and for the pure adsorbates an evolution of the electronic structure from atomic to bulk like could be observed through the disappearance of multiplet features in the absorption spectra. Adatoms of both elements showed a preference for their magnetic moments to align parallel to the sample surface. For Fe_3 , this preferred magnetization switched to perpendicular to the surface. Furthermore, the respective magnitudes of the magnetic moments were subject to strong size effects.

For the V_2 adsorbate, a strongly anisotropic absorption signal was observed and for the V_3 trimer, a switch of the magnetization direction with respect to the magnetic field could be seen depending on the angle between the X-ray photons and the sample surface. Possible explanations of both these effects were discussed.

A similar change in the magnetization direction was present for the Fe_1V_1 alloy dimer, which was explained as the result of a non-collinear spin flop phase via a simple theoretical model.

As a byproduct of this work, a photon induced effect on the absorption spectra was seen and a tentative explanation was given.

Röntgenspektroskopische Untersuchungen an kleinen massenselektierten Fe_nV_m Adsorbaten

Zusammenfassung

Im Zuge dieser Arbeit wurden die elektronischen und magnetischen Eigenschaften massenselektierter Fe und V Adsorbate auf einer nichtmagnetischen Cu(100) Oberfläche untersucht. Die Adsorbate hatten dabei eine Größe zwischen einem und drei Atomen und die Untersuchungen fanden *in situ* sowohl an elementreinen als auch an Legierungsclustern statt. Als Messmethode kamen Röntgenabsorptionsspektroskopie (XAS) sowie Röntgenzirkulardichroismus (XMCD) zum Einsatz. Dies ermöglichte die zerstörungsfreie und elementselektive Bestimmung der elektronischen Struktur sowie der jeweiligen magnetischen Momente jedes Elements der Legierung. Zum Zweck der magnetischen Untersuchungen fanden die Messungen in einem äußeren magnetischen Feld von 7 T statt.

Alle Adsorbate zeigten eine schwache Wechselwirkung mit der Substratoberfläche und es konnte, mit Hilfe des Verschwindens von Multiplettstrukturen in den Absorptionsspektren, jeweils eine Entwicklung der elektronischen Eigenschaften von atomartigen hinzu festkörperähnlichen Systemen beobachtet werden. Einzelne Adatome beider Materialien zeigten eine bevorzugte Ausrichtung ihres magnetischen Moments parallel zur Probenoberfläche. Im Falle des Fe_3 Adsorbates änderte sich diese Vorzugsrichtung hin zu einer senkrecht auf der Probe stehenden. Des Weiteren wurden starke Größeneffekte in den Größen der magnetischen Momente der reinen Adsorbate gemessen.

Im Falle des V_2 Adsorbates war eine starke Anisotropie im Absorptionsspektrum auffällig und bei dem V_3 Trimer konnte, in Abhängigkeit vom Einfallswinkel der Röntgenstrahlen auf der Probe, ein Richtungswechsel der Magnetisierung bezüglich des äußeren Feldes beobachtet werden. Für beide Effekte wurden mögliche Ursachen erläutert.

Für den Fe_1V_1 Legierungsdimer wurde ein ähnlicher Richtungswechsel gemessen und in diesem Fall konnte dieser mit Hilfe eines einfachen theoretischen Modells einer nichtkollinearen Spin-Flop-Phase zugeordnet werden.

Im Zuge der Messungen in dieser Arbeit wurde ein photoneninduzierter Effekt in den Absorptionsspektren entdeckt und eine mögliche Erklärung wurde über dessen Herkunft gegeben.

Contents

1. Introduction	1
2. Theoretical Background	5
2.1. Magnetism	5
2.1.1. Magnetic moments of an electron	5
2.1.2. Magnetism in the free atom	6
2.1.3. Magnetism in solids	7
2.1.4. Ferro-, Antiferro- and Ferrimagnetism	9
2.1.5. Magnetocrystalline anisotropy	10
2.1.6. Spin Flop	11
2.2. X-ray absorption spectroscopy	13
2.2.1. X-ray magnetic circular dichroism	17
2.2.1.1. Sum Rules	19
2.2.2. Angle dependency	21
2.2.3. Branching ratio	23
2.3. Crystal Fields	25
2.3.1. Point Charge Model	25
2.3.2. Spin crossover	29
3. Experimental Setup	31
3.1. Cluster Creation and Deposition	31
3.2. High Field Magnet Chamber	36
3.2.1. Cryostat Improvements	37
3.3. P04 Beamline	40
3.3.1. Spectra "On the fly"	43
3.4. Data Treatment	44
4. Results and Discussion	49
4.1. Homometallic adsorbates	49
4.1.1. $\text{Fe}_{1,2,3}$	49
4.1.2. $\text{V}_{1,2,3}$	58
4.2. X-ray induced spectral changes	69
4.3. Alloy adsorbates	74
4.3.1. Fe_1V_1	74
4.3.2. Fe_1V_2	82
5. Summary and Perspective	89

Contents

A. Wigner 3-j symbols	93
Bibliography	95
Acknowledgements	107

1. Introduction

"What happens when you cut a permanent magnet in half? And what if you do it repeatedly, until you reach atomically small sizes? Would it still be a permanent magnet?"

While these questions appear simple, they contain an important thought namely at what stage do certain properties of materials start to emerge and are these properties the same over the whole size range. The search to answer these questions has been at the heart of the study of atoms and clusters and the answer is that it is not so easy to tell. While the properties of macroscopic materials tend to evolve smoothly and predictably with the system size, the same can not be said at very small size scales. Rather, a material's properties can vary quite dramatically when a single atom is added or removed [1] and it is, at the moment, impossible to make reliable predictions on the properties, magnetic, electronic, geometric or otherwise, at system sizes of a few atoms (and even at a few hundreds of atoms). This in turn makes investigations into these systems so important, as experimentally determined properties of atoms and clusters can serve as valuable benchmarks to improve the predictive strength of the numerous theoretical models and help to better understand the interplay between different fundamental effects.

The cluster focused research is, of course, much more than a philosophical quest to the foundation of physics, it has important applications in the modern world. The scientific advancement of the past decades has led to a size reduction in virtually any technological device. For example, the capabilities of the enormous early computers are nowadays matched, and surpassed, by devices that can be carried around easily. The continuation of this trend will at some point necessarily cross over into the aforementioned size regime. Therefore, the search for novel, atomically small, material systems with tailored properties is a matter of general interest in technological and industrial applications. As an example, increasing the information density of storage media makes it necessary to find clusters that can serve as permanent magnets with a well defined magnetization that can be read and written with ease and keeps a stable state for a long time, all of which should happen at ambient temperature and pressure. To help in this endeavour, the present thesis will focus on the size-dependent magnetic properties of small clusters.

The investigation into these size effects is furthermore added to the well-established practice of combining different elements to get the most out of their individual strengths, and possibly find new ones. Cluster research in this regard adds "a third dimension" [2] to the periodic table, namely that of size. The addition of single atoms of a specific material might alter a cluster's response to certain conditions significantly. The interplay between different materials becomes especially important considering that, while a free cluster might have desirable properties, it is still necessary to integrate it into a device, which most often means that it has to be deposited onto a surface. The interplay between the substrate's geometry, its electronic structure and that of the deposited cluster influence both substrate and cluster, giving rise to new compound effects. For example, Brune *et al.* have shown that depositing Co atoms on a Pt(111) surface

leads to a strong increase in the Co magnetic moment and the appearance of a large magnetic anisotropy perpendicular to the sample surface [3]. Recently, Donati *et al.* also managed to show a magnetic remanence for single atoms of Ho on a MgO(100) surface [4].

Combining size, substrate and possible alloying with another material gives a vast parameter space to investigate. It is therefore necessary to restrict oneself to specific material combinations at any time and for this work it was chosen to stay within the $3d$ transition metals. The only known elements that show a permanent magnetic moment in the bulk are Fe, Co and Ni, all of which are $3d$ elements. This has led to this class of materials being studied intensely, which opens up many ways to compare to and to build on preexisting work. It is also in $3d$ transition metals that a large number of interactions, such as the exchange interaction and crystal field effects, are present at comparable energy scales which leads to a complex behaviour, hindering theoretical predictions [5].

An especially intriguing example of such complex behaviour are bulk alloys of $\text{Fe}_{1-x}\text{V}_x$, where in a V content range from $x \approx 30$ at% to 60 at%, the so-called σ -phase can be found [6]. This type of tetragonal phase is defined by a complex structure, comprising 30 atoms in a unit cell and of the roughly 50 cases of binary alloy systems where this phase has been found so far, σ -FeV and σ -FeCr are the only two that have well documented magnetic properties. It is interesting to note, that they both consist of a ferromagnet and an antiferromagnet. They have both been found to behave as reentrant magnet systems which, upon lowering of the temperature, undergo a transition from a paramagnetic to a ferromagnetic state and end up as a spin glass [7]. Of the two, FeV was chosen as the focus of this work, for one because the portion of the σ -phase in its phase diagram is bigger than for FeCr [6] and secondly because of the fewer isotopes of V, making it more suited for the present experiment. To take a closer look into the fundamental coupling between the two elements of this alloy, adsorbate systems with atomic amounts of the respective constituents were mass selected and deposited onto a Cu(001) surface, the choice of which is motivated by its sp -like density of states at the Fermi edge and the low-lying d -bands (see e.g. [8]). This provides the possibility for a weak substrate-adsorbate hybridization and is therefore important to ensure that the measured properties are mostly intrinsic to the adsorbate. It has been shown by Pacchioni *et al.* for Fe adatoms that Cu(111) fulfills this criterion quite well, reinforcing the present choice [9].

X-ray absorption spectroscopy (XAS) was chosen as a tool for the determination of the electronic properties of the alloy systems, seeing as the element specificity of X-ray transitions makes it a well-suited technique to investigate samples comprised of several different elements. To this end, beamtimes at the soft X-ray beamline P04 at the PETRA III storage ring at DESY were performed, where the adsorbates were produced *in situ* in an ultrahigh vacuum (UHV) sputter source with an added mass selector magnet. The decision for PETRA III was taken due to the high brilliance of the storage ring, translating to a high photon flux and allowing for fast measurements. This is important given that residual gases in the experimental setup can lead to rapid oxidization of the samples, thereby altering their electronic structure. Furthermore, the soft X-ray regime was used for the investigations, as the transitions into the unoccupied $3d$ levels of both Fe and V lie within that energy range and it is exactly these orbitals that mainly determine the electronic and magnetic response of these materials.

Additionally, P04 allows for the use of circular polarized light, leading to the absorption signal becoming sensitive to the magnetic moments of the probed elements in a process known

as X-ray magnetic circular dichroism (XMCD). This way, it was possible to determine the magnetic properties of both elements separately and, via theoretically derived sum rules [10, 11], determine their respective magnetic moments due to orbital and spin momentum.

Chapter 2 opens with a short glimpse into the fundamentals of the effects and experimental techniques encountered in this work. It is by no means exhaustive, but covers the basics so that the main results of this work can be understood without having to resort to external literature too often. Chapter 3 introduces the experimental apparatus, the sample preparation and the measurement process at the base of this work. Also, some upgrades to the experiment are presented. Chapter 4 presents the results of the absorption measurements and puts them into the context of earlier work, both experimental and theoretical. The thesis is concluded by a short summary in Chapter 5, which also gives a few impulses on possible experimental and theoretical developments in the future.

2. Theoretical Background

This chapter shall give a brief introduction into the theoretical foundations relevant to this work, namely the magnetism of adsorbates, the spin-dependent X-ray absorption and the influence of the surface geometry on the electronic states of the adsorbates.

The treatment of these topics will be kept brief and the reader shall be directed to more extensive literature, if desired.

2.1. Magnetism

2.1.1. Magnetic moments of an electron

Classically, the magnetic moment arising due to the orbital motion of an electron with charge $-e$ and mass m_e around a nucleus is given by: [12]

$$\begin{aligned}\vec{m}_l &= -\frac{e\mu_0}{2m_e}\vec{l} \\ \vec{m}_l &= -\frac{\mu_B}{\hbar}\vec{l}\end{aligned}\quad (2.1.1)$$

With the vacuum permeability μ_0 , the orbital momentum \vec{l} of the electron and where the Bohr magneton was defined as $\mu_B = \mu_0 e \hbar / (2m_e)$. In a quantum mechanical sense, only the component of the orbital momentum along a given axis can be measured. For an arbitrary z-axis this gives:

$$\langle m_l^z \rangle = -\frac{\mu_b}{\hbar} \langle l_z \rangle \quad (2.1.2)$$

It should be noted that $\langle l_z \rangle$ is given in units of \hbar . Similarly to this, yet without a classical analogue, the electron has a spin magnetic moment, whose component in z-direction is:

$$\langle m_s^z \rangle = -g_S \frac{\mu_b}{\hbar} \langle s_z \rangle \quad (2.1.3)$$

Where g_S is the electron g -factor, assumed to be equal to two for the rest of this work. Combining these two expressions, the total magnetic moment of an electron has a z-component:

$$\langle m_{tot}^z \rangle = \langle m_s^z \rangle + \langle m_l \rangle = -\frac{\mu_B}{\hbar} (2\langle s_z \rangle + \langle l_z \rangle) \quad (2.1.4)$$

And the energy of a magnetic moment in an external magnetic field is given by: [13]

$$\begin{aligned}
 E &= -\vec{m} \cdot \vec{B} \\
 &= \frac{\mu_B}{\hbar} \vec{B} \cdot (2\vec{s} + \vec{l})
 \end{aligned}
 \tag{2.1.5}$$

Where in the second step, the magnetic moment of an electron was inserted.

2.1.2. Magnetism in the free atom

Since atoms are made up of more than one electron, it is important to consider expressions for the spin and orbital magnetic moments that arise in such a case. In general for both orbital and spin, the total momentum of all the n electrons making up an atom is simply the vector sum of all the individual electrons' momenta:

$$\begin{aligned}
 \vec{L} &= \sum_{i=1}^n \vec{l}_i \\
 \vec{S} &= \sum_{i=1}^n \vec{s}_i
 \end{aligned}
 \tag{2.1.6}$$

Where all the electrons in completely filled orbitals can be neglected, since their momenta will always sum to zero. However, not all possible combinations of total orbital and spin momentum are equally likely. This comes from the fact, that due to the Pauli principle, the spin part of a wavefunction influences the spatial part and that the orbital momentum is a measure of how the electrons move around the nucleus. So both quantities are influenced by the spatial motion of the electrons, and hence can not be viewed as separate entities. This effect is known as spin-orbit coupling and it leads to spin and orbital moment adding up to a total angular momentum:

$$\vec{J} = \vec{L} + \vec{S}
 \tag{2.1.7}$$

This way of coupling the spin and orbital motion of the electrons, first adding all the individual momenta of one kind and then adding the resulting vectors, is known as Russel-Saunders coupling or *LS*-coupling. It is valid in the case that the spin-orbit coupling is weak and can be considered a small perturbation. For the $3d$ electrons of the light materials in this work, this is fulfilled. Another way to include the spin-orbit coupling would be to first couple \vec{l}_i and \vec{s}_i for each individual electron, giving \vec{j}_i and then summing over all electrons. This is known as *jj*-coupling and is usually the case for a strong spin-orbit coupling, e.g. in heavy atoms and close to the nucleus.

The magnetic moment associated with this total momentum is then given by:

$$\langle m_J^z \rangle = -\frac{g_J}{\hbar} \langle J_z \rangle
 \tag{2.1.8}$$

Where the Landé factor g_J is: [13]

$$g_J = \frac{3}{2} + \frac{S(S+1) - L(L+1)}{2J(J+1)} \quad (2.1.9)$$

Here S , L and J are the many-electron quantum numbers. In the case of LS -coupling, the ground state configuration of a many-electron atom can be found by applying Hund's rules (in decreasing order of importance): [13]

1. The spin momentum S is maximized. Because of the Pauli exclusion principle, electrons with the same spin can not be in the same place. By maximizing the spin, the Coulomb repulsion between electrons is minimized.
2. The orbital momentum L is maximized. This leads to an increased spreading of the electronic wavefunctions, reducing Coulomb repulsion in the process.
3. For a less than half filled shell, $J = |L - S|$. Similarly, $J = L + S$ if the shell is more than half full. This minimizes the spin-orbit energy.

The third rule is however only valid if the spin-orbit coupling is the strongest interaction in the system after the Coulomb interaction. This is not necessarily given in the case of e.g. crystal fields.

2.1.3. Magnetism in solids

The magnetic moments of all the atoms in a solid add up to a collective magnetic moment and, in order to have an intensive quantity, the magnetization \vec{M} is defined as the sum of the magnetic moments in a given volume divided by its size:

$$\vec{M} = \frac{1}{V} \sum_V \vec{m} = \frac{N}{V} \vec{m} = n \vec{m} \quad (2.1.10)$$

Where N equal magnetic moments were assumed and n is the density of magnetic moments. In an external magnetic field \vec{H} , the magnetic moments of a solid's atoms will align in the external magnetic field (cf. (2.1.5)), creating a magnetization and a magnetic field such that the total magnetic field in the solid will be given by:

$$\vec{B} = \mu_0 (\vec{H} + \vec{M}) = \mu_0 (1 + \chi) \vec{H} \quad (2.1.11)$$

Here, χ is the magnetic susceptibility and it is assumed that the material is linearly related to the external field, i.e. that $\vec{M} = \chi \vec{H}$.¹ Based on the value of χ , two general classes of materials can be distinguished.

If $\chi < 0$, the material is called diamagnetic and its magnetization will be aligned antiparallel to an external field. All materials have a diamagnetic effect, but it is several orders of magnitudes smaller than other magnetic effects and hence only apparent if those effects are absent.

If $\chi > 0$, the material is called paramagnetic. The internal magnetic moments will align parallel to the external field. In the absence of an external field, the internal magnetic moments

¹In free space, $\vec{M} = 0$ and $\vec{B} = \mu_0 \vec{H}$, this is why an external field will be denoted by \vec{B} in this work.

will be generally unaligned and the resulting magnetization will be zero. The magnetization of a paramagnetic material is given by the Brillouin function: [13]

$$\frac{M}{M_s} = B_J(x) = \frac{2J+1}{2J} \coth\left(\frac{2J+1}{2J}x\right) - \frac{1}{2J} \coth\left(\frac{1}{2J}x\right) \quad (2.1.12)$$

With

$$\begin{aligned} M_s &= n g_J \mu_B J \\ x &= \frac{g_J \mu_B J B}{k_B T} \end{aligned} \quad (2.1.13)$$

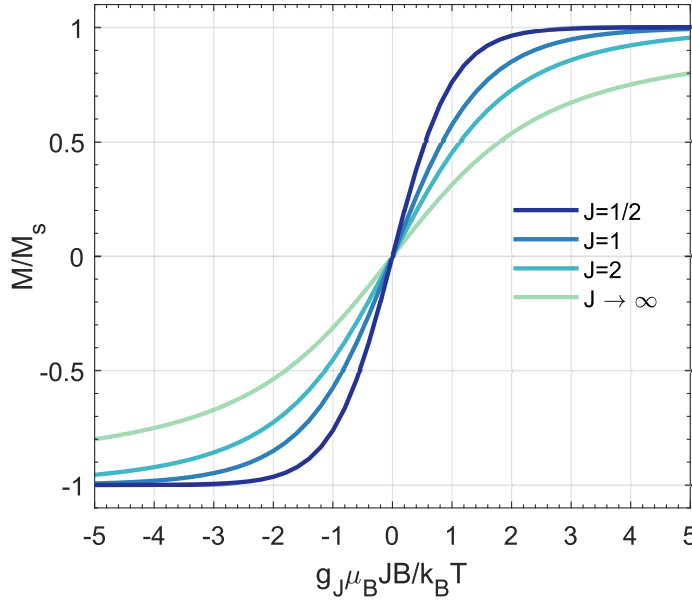


Fig. 2.1.: Graph of the magnetization of a paramagnetic material in an external magnetic field given by the Brillouin function (2.1.12) for different values of the total angular momentum. In the limit that J tends to infinity, the behaviour of a classic system is recovered.

Where M_s is the saturation magnetization and k_B is the Boltzmann constant. Fig. 2.1 shows the behaviour of the paramagnetic magnetization as a function of x for different values of J . In the limit that J tends towards infinity, the behaviour of a classical magnetic moment in an external magnetic field is retrieved. A paramagnetic material then has a susceptibility given by:

$$\chi = \frac{C}{T} = \frac{\mu_0 n J(J+1) g_J^2 \mu_B^2}{3 k_B T} \quad (2.1.14)$$

C is called the Curie constant.

2.1.4. Ferro-, Antiferro- and Ferrimagnetism

There exists a third class of materials, namely those whose magnetization remains without an applied external field. This is called a spontaneous magnetization and it comes in three different kinds, which are schematically shown in Fig. 2.2

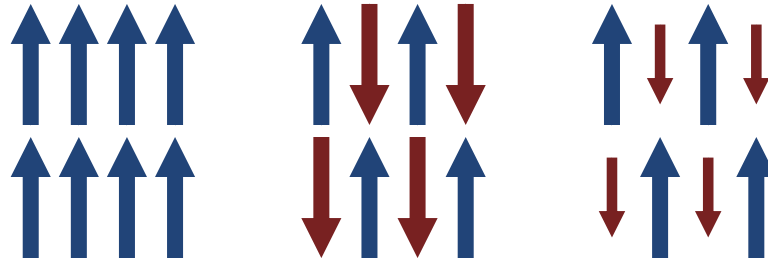


Fig. 2.2.: Sketch of the order of magnetic moments in a ferromagnet (left), an antiferromagnet (middle) and a ferrimagnet (right).

In a ferromagnet, the magnetic moments are aligned parallel to each other even in the absence of a magnetic field (cf. the left panel in Fig. 2.2). The origin of this rigid order² lies in the exchange interaction between the electrons. The exchange interaction is a quantum mechanical effect arising due to the Coulomb interaction and the Pauli principle. In a two electron system where the spins are either aligned parallel or antiparallel, it can be shown that the state with parallel spins is energetically favourable (cf. for example [13]). This can again be explained intuitively by saying that for antisymmetric (antiparallel) spins, the spatial part of the many-electron wavefunction must be symmetric, this reduces the mean spatial distance between the electrons, increasing the Coulomb repulsion in the process. If the spins are parallel, the electrons are generally further apart. This energy difference is quantified in the so-called Heisenberg Hamiltonian:

$$\hat{\mathcal{H}} = - \sum_{i,j} J_{ij} \vec{S}_i \cdot \vec{S}_j \quad (2.1.15)$$

Where J_{ij} is the exchange constant between two neighbouring spins i and j . If only next neighbour interactions are included, J_{ij} can usually be taken to be isotropic and replaced by J . A ferromagnetic exchange is characterized by $J > 0$. The susceptibility has been found to be temperature dependent and it follows the Curie-Weiss law above a critical temperature, known as the Curie temperature T_C , which as a material constant:

$$\chi = \frac{C}{T - T_C} \quad (2.1.16)$$

If $J < 0$ however, the spins in question will align preferably antiparallel to each other. This antiferromagnetic exchange leads to a rigid ordering with each spin of one direction being preferably surrounded by spins of the opposite direction (cf. middle panel in Fig. 2.2). The resulting magnetization is zero as all magnetic moments cancel. Similarly to the ferromagnetic

²Usually, not all the magnetic moments are aligned throughout the whole material. However there are large domains of aligned moments and the magnetization of different domains can point in different directions.

case, the susceptibility of an antiferromagnet is constant (and zero) below a critical, material dependent, temperature known as the Néel temperature T_N and is inversely proportional to the temperature above it:

$$\chi = \frac{C}{T + T_N} \quad (2.1.17)$$

While for electrons on the same atom it is usually favourable to have spins aligned parallel and a positive exchange constant, in the case of exchange interaction between electrons on neighbouring atoms, this does not have to be the case. The formation of bonds between the atoms leads to a larger spatial spread of the electronic wavefunction, lowering the energy in the process.³ If the combination of the wavefunctions is bonding, i.e. both wavefunctions have equal sign, then the spatial part of the resulting wavefunction is symmetric and is energetically favoured over the case of an antibonding combination, where the wavefunction is antisymmetric. The bonding orbital spatially necessarily leads to an antisymmetric combined spin orbital, and hence negative exchange constant.

An antiferromagnet can be viewed as the combination of two ferromagnetic lattices that are of equal magnetization and aligned opposite of each other, cancelling each other. If however the magnetization of one of the lattices is smaller than the other, there will be a remaining magnetization of the material. This is known as ferrimagnetism and can schematically be seen on the right side of Fig. 2.2. A reason for this could be that the material consists of several different elements, each one potentially carrying a different magnetic moment. Although ferrimagnetism also produces a magnetization in the absence of an external field, it should not be confused with ferromagnetism, since not all magnetic moments are aligned in the same direction. Since the susceptibility of the material is then a result of the susceptibilities of each lattice, the temperature dependence can be rather complex, with the possibility that one lattice dominates at lower temperatures but the other one at higher temperatures.

2.1.5. Magnetocrystalline anisotropy

Magnetization measurements on known ferromagnetic materials like Fe, Co and Ni have shown that not all crystal directions are equally easy to be magnetized (e.g. [14]). This magnetic anisotropy was linked to the crystal directions of the material and has since been known as magnetocrystalline anisotropy (MCA). It leads to directions called "easy axes" in which the magnetization process is favoured and "hard axes" in which the magnetization takes more energy. Van Vleck linked the MCA to the electric potential of the crystal nuclei influencing the orbital motion of the electrons and the spin-orbit coupling then translating this influence to the spin momentum of the electrons.

The first few anisotropy energy terms arising for different crystal systems are given by: [13, 15]

³This follows from the simple treatment of a particle in a box.

$$\begin{aligned}
E_{ani}^{cubic}/V &= K_1 \left(\frac{1}{4} \sin^2 2\phi \sin^2 \theta + \cos^2 \theta \right) \sin^2 \theta + \frac{K_2}{16} \sin^2 2\phi \sin^2 2\theta \sin^2 \theta \\
E_{ani}^{hexagonal}/V &= K_1 \sin^2 \theta + K_2 \sin^4 \theta + K_3 \cos^6 6\phi \\
E_{ani}^{tetragonal}/V &= K_1 \sin^2 \theta + K_2 \sin^4 \theta + K_3 \sin^4 \theta \sin 2\phi
\end{aligned}
\tag{2.1.18}$$

Here V is the volume of the crystal, the K_i are called anisotropy constants and θ and ϕ are the elevation and azimuth angle, as defined in the spherical coordinates. For hexagonal (tetragonal) systems, the z-direction was defined as the stacking direction of the hexagonally close packed (square) planes. The expressions for both, the hexagonal and tetragonal case have a $\sin^2 \theta$ dependence in their lowest term, which they have in common with all systems that have a single axis of high symmetry. Ignoring higher order terms, this is generalized as an uniaxial anisotropy.

The anisotropy constants have the dimension of energy density and their values lie in the range of 10^2 – 10^8 J/m³ or equivalently 10^{-8} – 10^{-2} eV/atom [13], where very high anisotropy constants of ~ 10 meV/atom and ~ 60 meV/atom were found for a single Pt atom on an MgO(100) surface and a Co atom on a Pt(111) surface respectively [16, 17]. Generally, the anisotropy for systems with reduced symmetry, such as thin films, surfaces or adsorbates, is higher than for extended crystals (e.g. [18]).

2.1.6. Spin Flop

If a sufficiently strong magnetic field is applied parallel to the magnetization of a material with $J < 0$ below the critical temperature, the energy gained from the magnetic moments aligning with the field will at some point dominate the exchange interaction and the anisotropy of the crystal and all the magnetic moments will align. Depending on the material in question, this transition can however either be abrupt or there is a possible intermediate phase where at a specific field strength, the magnetic moments of both sublattices will snap away from the easy axis and form a canted arrangement. This is known as the spin flop transition and shall be explained in the following.

Based on the work of Radwański on the so-called two magnetic sublattices model [19], one can write the overall energy of a compound $A_x B_y$ as follows:

$$\begin{aligned}
E &= -B (m_A \cos(\alpha_A + \theta) + m_B \cos(\alpha_B - \theta)) \\
&\quad - J_{A-B} m_A m_B \cos(\alpha_A + \alpha_B) \\
&\quad + x K_{uni}^A \sin^2 \alpha_A + y K_{uni}^B \sin^2 \alpha_B
\end{aligned}
\tag{2.1.19}$$

Here, $m_{A,B}$ are the magnitudes of respective magnetic moments of the sublattices and B is the strength of the external magnetic field. J_{A-B} is the exchange coupling strength between the magnetic sublattices. Furthermore, it is assumed that every sublattice is subject to an uniaxial anisotropy, expressed in the respective anisotropy constants $K_{uni}^{A,B}$. These anisotropy terms are

also proportional to x and y , the stoichiometric factors of the respective sublattices. In their work, the respective angles of the magnetic moments ($\alpha_{A,B}$) and of the magnetic field (θ) are defined in respect to the easy axis of the lattice, i.e. the surface normal (cf. the left panel in Fig. 2.3).

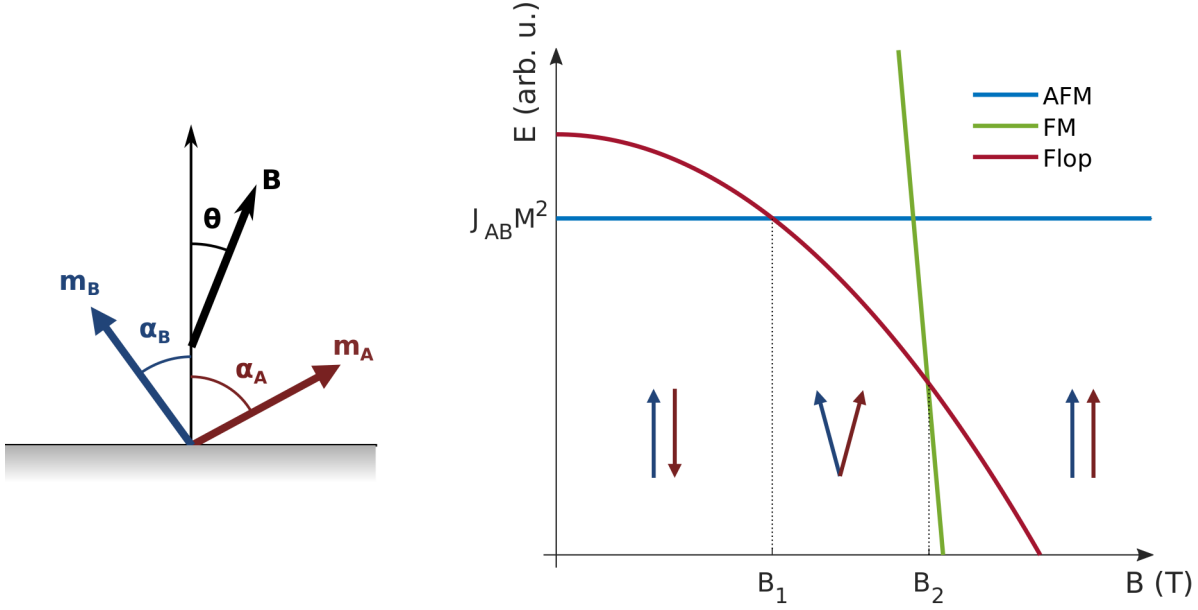


Fig. 2.3.: (Left) Schematic of the angles used in the two magnetic sublattices model. (Right) comparison of the energies of the antiferromagnetic phase (AFM), the ferromagnetic phase (FM) and the spin flop phase (Flop) of the two sublattices model in case of a pure antiferromagnetic material. Also included are the field values B_1 and B_2 where the phase switches from AFM to Flop and from Flop to FM, respectively.

For the special case of a pure antiferromagnet and a magnetic field applied along the easy axis, $m_A = m_B = m$, $K_{uni}^A = K_{uni}^B = K$, $\theta = 0$ and $x = y = 1$, this simplifies to:

$$E = -mB(\cos \alpha_A + \cos \alpha_B) - J_{AB}m^2 \cos(\alpha_A + \alpha_B) + K(\sin^2 \alpha_A + \sin^2 \alpha_B) \quad (2.1.20)$$

For the antiferromagnetic phase, the magnetic moments are aligned antiparallel and along the easy axis, so $\alpha_A = 0$ and $\alpha_B = \pi$. Similarly, for the ferromagnetic phase, $\alpha_A = \alpha_B = 0$. (2.1.20) then reads:

$$\begin{aligned} E_{AFM} &= J_{AB}m^2 \\ E_{FM} &= -2mB - J_{AB}m^2 \end{aligned} \quad (2.1.21)$$

Since both magnetic moments are the same for an antiferromagnet, the angles these moments form with the magnetic field will be equal ($\alpha_A = \alpha_B = \alpha$). The energy will then be given by:

$$\begin{aligned}
 E_{Flop} &= -2mB \cos \alpha - J_{AB}m^2 \cos 2\alpha + 2K \sin^2 \alpha \\
 \frac{\partial E_{Flop}}{\partial \alpha} &= 2mB \sin \alpha + 4J_{AB}m^2 \sin \alpha \cos \alpha + 4K \sin \alpha \cos \alpha
 \end{aligned}
 \tag{2.1.22}$$

One minimum of E_{Flop} is found for $\alpha = n\pi$, where n is an integer, corresponding to the ferromagnetic solution. The other minimum is found when:

$$\alpha = \arccos \left(-\frac{mB}{2(J_{AB}m^2 + K)} \right)
 \tag{2.1.23}$$

Inserting (2.1.23) into (2.1.22) yields an unwieldy expression, that is quadratic in the applied magnetic field. Plotting the expression for the energies of all three phases as a function of the magnetic field (cf. right panel in Fig. 2.3), reveals that, indeed, above a certain field B_1 the spin flop phase becomes energetically favourable compared to the antiferromagnetic phase. The magnetic moments will abruptly enter a canted state and, increasing the magnetic field further, the canting angle α will decrease up until it becomes zero or up to the field B_2 , at which point the energy of the ferromagnetic phase will be lower than the spin flop phase and the magnetic moments will abruptly align parallel to each other and the magnetic field. Independently of which of these might happen first, from that point on, the system will be in the ferromagnetic state.

Apart from the simple case treated here, (2.1.19) can usually not be minimized analytically with respect to α_A and α_B , but rather requires numerical minimization procedures.

A crucial assumption in the work of Radwański was that the magnetic moments within each sublattice are coupled rigidly and are all parallel. With this model, their calculations showed for a number of GdCo compounds the existence of a spin flop phase, given high enough magnetic fields.

2.2. X-ray absorption spectroscopy

The interaction of matter with electromagnetic waves, more specifically with X-rays, is at the heart of this work. The target in question is illuminated with monochromatic X-rays, which will be absorbed and their energy will serve to excite electrons of the target from deep lying bound states into either higher energetic, unoccupied states of the material or into the continuum, depending on the energy of the incoming X-rays. This is schematically shown in the left and middle panel of Fig. 2.4. The resulting hole left by the excited core electron is then filled by a higher energetic electron, leading to either the emission of an electron in the Auger decay process (cf. the right part of Fig. 2.4) or to the emission of a fluorescence photon. The fluorescence process is omitted from the schematic figure and further explanations, as it is several orders of magnitude less likely to occur in the present elements than the Auger process [20]. The number of Auger electrons leaving the sample is proportional to the number of core holes created by excitation processes, resonant or off-resonant, this makes the electron current at the sample a measure of the absorption strength, forming the basis of the total electron yield (TEY) detection scheme, which will be employed in this work. The electrons created by either photoexcitation

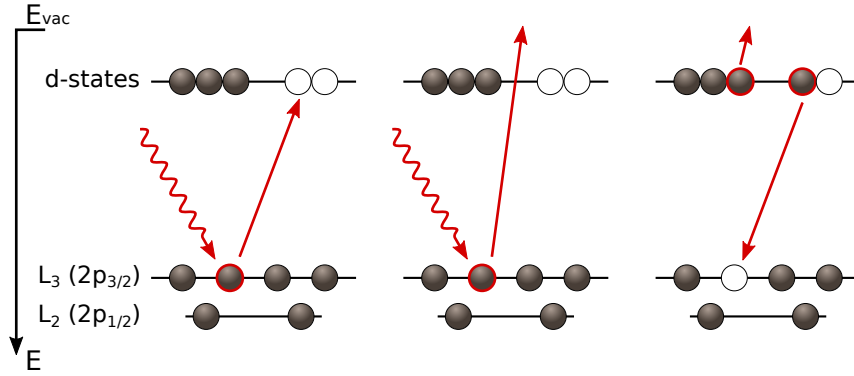


Fig. 2.4.: Schematic of the photon absorption process for the case of $2p \rightarrow 3d$ absorption. (Left) Resonant excitation in the case that energy of the incoming photon exactly matches the energy difference between an occupied p -state and an unoccupied d -state. (Middle) Off-resonant excitation in the case that the photon energy is high enough to excite the p -electron into the vacuum. (Right) After an excitation, the resulting core hole can be filled via Auger decay of a d -electron, where another d -electron gets excited into the vacuum.

or subsequent Auger processes have to leave the sample material, a process during which they undergo further scattering processes. This limits the possible depth from which these electrons can be detected. More specifically, for the soft X-ray energies of this work, the escape depths of electrons is in the order of 10-100 Å [5], which makes the TEY signal surface sensitive.

As can be seen from the left panel in Fig. 2.4, the resonant excitation of core electrons occurs in the case when the incoming photon energy matches the energy difference between the occupied core level and the unoccupied valence levels, which for the case of this work are the $2p$ and $3d$ levels, respectively. It is exactly this property of the absorption process which makes spectroscopic investigations using absorption such a powerful tool. The binding energies of the levels involved in the absorption process are specific for each element, sensitive to the chemical environment of the absorbing atom and are also subject to splitting due to the spin-orbit interaction in the core states. This can, for example, be seen for the energy levels of the three elements V, Fe and Cu which appear in this work (cf. Tab. 2.1). This element sensitivity allows X-ray absorption spectroscopy (XAS) to investigate the properties of different elements in an alloy separately and to relate changes in the absorption spectrum to changes in the electronic structure of the target elements.

Element	$K (1s)$	$L_1 (2s)$	$L_2 (2p_{1/2})$	$L_3 (2p_{3/2})$	$M_1 (3s)$	$M_2 (3p_{1/2})$	$M_3 (2p_{3/2})$
V	5465	626.7	519.8	512.1	66.3	37.2	37.2
Fe	7112	844.6	719.9	706.8	91.3	52.7	52.7
Cu	8979	1096.7	952.3	932.7	122.5	77.3	75.1

Tab. 2.1.: Binding energies in eV for the three elements appearing in this work. The values are taken from [20]. The most important energies for the present work are the L_2 and L_3 edges of Fe and V.

The transition probability per unit time of an electron from an initial state $|i\rangle$ with energy E_i to a final state $|f\rangle$ with energy E_f caused by a harmonic time-dependent perturbation $H(t) = \bar{H}_{int} e^{-i\omega t}$ is given in first order perturbation theory by Fermi's golden rule:

$$T_{i \rightarrow f} = \frac{2\pi}{\hbar} |\langle f | \bar{H}_{int} | i \rangle|^2 \rho_f(E) \delta(E_f - E_i - \hbar\omega) \quad (2.2.1)$$

With the reduced Planck constant \hbar , the angular frequency of the perturbing oscillating field ω and the density of final states $\rho_f(E)$. Use of the Dirac delta distribution makes sure that the energy between the incoming photon and the initial and final states is conserved. For a plane electromagnetic wave, the time independent part of the perturbation Hamiltonian can be written:

$$\bar{H}_{int} = \frac{e}{2m_e c} A_0 e^{i\vec{k} \cdot \vec{r}} \vec{\varepsilon} \cdot \vec{p} \quad (2.2.2)$$

With the electron's charge e , its mass m_e , the velocity of light c and A_0 the amplitude of the vector potential of the wave. \vec{k} is the wavevector of the incoming electromagnetic wave, $\vec{\varepsilon}$ is its photon polarization vector and \vec{p} is the momentum vector of all the electrons involved. If $\vec{k} \cdot \vec{r} \ll 1$, or equivalently $|\vec{r}| \ll \lambda/2\pi$, only the first term of the Taylor expansion of the exponential in (2.2.2) is kept (λ is the wavelength of the incoming photons). This is known as the dipole approximation, and is justified in light of the photon energies encountered in this work.⁴

To get from the transition probability $T_{i \rightarrow f}$ to the absorption cross section $\sigma(E)$, (2.2.1) is divided by the photon flux F_{ph} of the incoming electromagnetic wave. From [21], it is:

$$F_{ph} = \frac{A_0^2 \omega}{8\pi \hbar c} \quad (2.2.3)$$

So that the absorption cross section can be written:

$$\begin{aligned} \sigma(E) &= \frac{4\pi^2 e^2}{m_e^2 \omega c} |\langle f | \vec{\varepsilon} \cdot \vec{p} | i \rangle|^2 \rho_f(E) \delta(E_f - E_i - \hbar\omega) \\ \sigma(E) &= \frac{4\pi^2 e^2}{\hbar^2 \omega c} (E_f - E_i)^2 |\langle f | \vec{\varepsilon} \cdot \vec{r} | i \rangle|^2 \rho_f(E) \delta(E_f - E_i - \hbar\omega) \end{aligned} \quad (2.2.4)$$

Where in the last step it was made use of the fact that, $\vec{p} = im_e(E_f - E_i)/\hbar \vec{r}$ [21]. This expression shows that the absorption cross section is mainly determined by the density of final states as well as the transition matrix element between initial and final state. To evaluate the transition matrix element, the dot product $\vec{\varepsilon} \cdot \vec{r}$ can be expressed as [22]:

$$r \sqrt{\frac{4\pi}{3}} Y_q^1 = r C_q^1 \quad (2.2.5)$$

With $q = -1, 0, 1$ for incoming radiation with negative helicity, linear polarization or positive helicity, respectively. Here, Y_q^k are the spherical harmonics of degree k and order q and the C_q^k are Racah's spherical tensors, which are related to the spherical harmonics via

⁴Consider, for example, a photon energy of 1000 eV, corresponding to a wavelength of 1.24 nm. The value of $|\vec{r}|$ can be taken as the Bohr radius, which is roughly 0.05 nm.

$C_q^k = \sqrt{4\pi/(2k+1)}Y_q^k$. Expressing both the initial and the final state as atomic spin orbitals with separable radial, angular and spin parts, the matrix elements in (2.2.4) can be evaluated via:

$$\begin{aligned} & \langle R_{n_f, l_f}(r); l_f, m_{l_f}, s_f | r C_q^1 | R_{n_i, l_i}(r); l_i, m_{l_i}, s_i \rangle \\ & = \langle l_f, m_{l_f} | C_q^1 | l_i, m_{l_i} \rangle R \delta_{s_f, s_i} \\ & = (-1)^{l_f - m_{l_f}} \begin{pmatrix} l_f & 1 & l_i \\ -m_{l_f} & q & m_{l_i} \end{pmatrix} \langle l_f || C^1 || l_i \rangle R \delta_{s_f, s_i} \end{aligned} \quad (2.2.6)$$

Where R is the radial integral and δ_{s_f, s_i} is the Kronecker delta between the spin of the two states, making sure that no spin flip occurs ($\Delta s = 0$). Also, the Wigner-Eckart theorem (cf. for example [23, 24]) was used in the second step to split the matrix element into a reduced matrix element $\langle l_f || C^1 || l_i \rangle$ and a Wigner 3- j symbol, which contains all the angular information of the integral. For Racah's spherical tensors, the reduced matrix elements can be calculated via [23]:

$$\langle l_f || C^k || l_i \rangle = (-1)^{l_f} \sqrt{(2l_f + 1)(2l_i + 1)} \begin{pmatrix} l_f & k & l_i \\ 0 & 0 & 0 \end{pmatrix} \quad (2.2.7)$$

The advantage of this notation lies in the fact that the 3- j symbols replace general integrals over angular coordinates, meaning that they can be reused for a lot of calculations, reducing work in the process. Also, just by looking at it it can be gauged if a 3- j symbol vanishes. A general formula for the calculation of the 3- j symbols is given in Appendix A, along with a number of conditions that must be met, lest the symbol vanishes. In particular for this integral, it must be satisfied that $l_f = l_i \pm 1$ and $m_{l_f} = m_{l_i} + q$.

Starting from a $2p$ core state ($l_i = 1$), as is the case in this work, dipole radiation therefore allows transitions into states with $l_f = 0$ and $l_i = 2$, i.e. s -states and d -states. Since the magnetic properties of the $3d$ elements of interest in this work are mostly determined by their d -electrons [5], the contributions to the absorption signal stemming from the $p \rightarrow s$ transitions have to be removed in order to get the absorption strengths related solely to the $p \rightarrow d$ transitions. Fortunately, the contributions from $p \rightarrow s$ make up at most 5 % of the total absorption intensity in the case of $2p$ states [25]. This is mostly due to the d -states being more strongly localized on the nucleus and hence the overlap between $2p$ and $3d$ orbitals being stronger than between $2p$ and $4s$ states.

Based on the general expression of 3- j symbols in Appendix A, a compact form for (2.2.6) and (2.2.7) in the case of a $l \rightarrow l + 1$ transition, such as the $2p \rightarrow 3d$ transition, can be found [22]:

$$\begin{aligned}
 \langle l+1, m_l-1 | C_{-1}^1 | l, m_l \rangle &= -\sqrt{\frac{(l-m_l+2)(l-m_l+1)}{2(2l+3)(2l+1)}} R \\
 \langle l+1, m_l | C_0^1 | l, m_l \rangle &= \sqrt{\frac{(l-m_l+1)(l+m_l+1)}{(2l+3)(2l+1)}} R \\
 \langle l+1, m_l+1 | C_1^1 | l, m_l \rangle &= -\sqrt{\frac{(l+m_l+2)(l+m_l+1)}{2(2l+3)(2l+1)}} R
 \end{aligned}
 \tag{2.2.8}$$

2.2.1. X-ray magnetic circular dichroism

Besides information on the transition matrix elements and the density of unoccupied states, the use of circular polarized light carrying a helicity of $q = \pm 1$ can give insight into the magnetic properties of the target material. The effect behind this is known as X-ray magnetic circular dichroism (XMCD) and was first described theoretically by Erskine and Stern for the $M_{2,3}$ edges of Ni [26]. Experimental confirmations came from Schütz *et al.* for the K -edge of Fe in 1987 [27] and from Chen *et al.* for the $L_{2,3}$ edges of Ni in 1990 [28]. To better understand this effect, it is helpful to examine the $2p \rightarrow 3d$ absorption process in a one-electron picture.

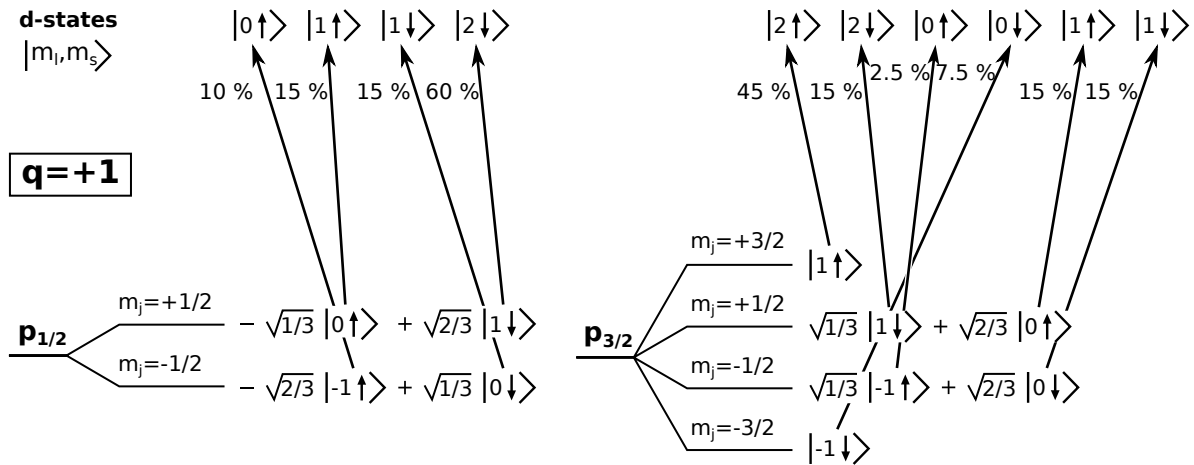


Fig. 2.5.: Schematic of the transition processes from the spin-orbit split p -states into d -states upon absorption of a circularly polarized photon with helicity $q=+1$. The transition probabilities are indicated for each particular transition. (Left) For the $2p_{1/2}$ states, i.e. the L_2 edge. (Right) For the $2p_{3/2}$ states, i.e. the L_3 edge.

Since the $2p$ states are close to the nucleus, the spin-orbit interaction between them is of great importance, leading to a jj -coupling (cf. 2.1.2) and the splitting of the degenerate states into a $2p_{1/2}$ (L_2) and $2p_{3/2}$ (L_3) manifold, formed by combining the uncoupled atomic states according to the respective Clebsch-Gordan coefficients. In a first step, the circularly polarized light carrying an angular momentum of $\pm\hbar$ (depending on the helicity q) excites electrons from

either of these manifolds. Due to the conservation of angular momentum, the photons angular momentum is transferred to the excited electron and because of the spin-orbit coupling, some of the angular momentum is transformed into a spin polarization of the electrons. This can be seen from evaluating the matrix elements of all the possible transitions from the spin-orbit split states into degenerate d -states using (2.2.8). The results of these calculations are summarized in Fig. 2.5, where it can be seen that absorption of a photon with $q = +1$ leads to the excitation of 75 % of electrons with "spin-down" and 25 % with "spin-up" at the L_2 edge. Since the coupling of orbital and spin momentum is opposite at the L_3 edge, it is unsurprising that for the L_3 edge the same photon helicity leads to the excitation of 62.5 % of "spin-up" electrons versus 37.5 % of "spin-down" electrons. It should be noted that the spin orientations at this step are relative to the helicity of the incoming photon. In the case that the absorbed photon has a helicity of -1, the percentages of the spin polarization would invert for each edge.

At this point it is a good idea to define the handedness of circular polarized light used in this work. It can either be defined from the point of view of the photon source or the photon receiver. The latter definition, which defines right (left) circularly polarized light as having a negative (positive) helicity $q = -1$ ($q = +1$) and is known as the optical convention, is employed in this work. This is in contrast to earlier works on this topic (cf. for example [22]) but will become clearer when talking about the source of X-ray radiation (cf. 3.3).

The magnetic properties of the target enter in the second step. The electron-electron exchange interaction in the $3d$ -states leads to a splitting into spin bands and, in the case of an unequal number of spins of either orientation, lowers the energy of one of the spin bands (majority spins) while raising the energy of the other spin band (minority spins). This can be seen schematically on the left side of Fig. 2.6. Since the excited, spin-polarized, photoelectrons can only end up in the band with equal spin orientation (due to $\Delta s = 0$), they then serve as a probe of the density of states of the spin-split bands, which is lowered for the majority band. Looking at (2.2.4), this leads to a weakened absorption at the L_3 edge and increased absorption at the L_2 edge in the case of a photon with a polarization vector parallel to the direction of the majority band. In the case that the photon polarization vector is antiparallel to the spin direction in the majority spin band, the absorption signal is increased at the L_3 edge and decreased at the L_2 edge. As this effect is greatest in the case of the electron spins being aligned to a common axis, it is customary to use an external magnetic field in order to align the electron spins more effectively.

By measuring the absorption across both L -edges, once with the photon polarization vector and majority spin direction parallel and once antiparallel, and taking the difference of both signals, i.e. $I_{\downarrow\downarrow} - I_{\uparrow\downarrow}$ ⁵, one arrives at the XMCD signal, which is a measure of the spin imbalance in the final states. As can be seen from the areas on the right side of Fig. 2.6, this difference is negative at the L_3 edge and positive at the L_2 edge, as is expected from the different spin-orbit coupling in the respective $2p$ manifolds. Similarly to the spin momentum, unequal occupation of valence states with differing orbital momentum leads to different absorption strengths, since photons with helicity 1 (-1) can only lead to transitions with $\Delta m_l = +1$ ($\Delta m_l = -1$). Since the sum over both areas in Fig. 2.6 contains the contributions of all the excited electrons, there is no net spin polarization and hence no information on the spin imbalance in the valence bands. Thus, summing the XMCD signal over both excitation edges gives the orbital imbalance.

⁵This is the same way it was defined e.g. in [22, 28]

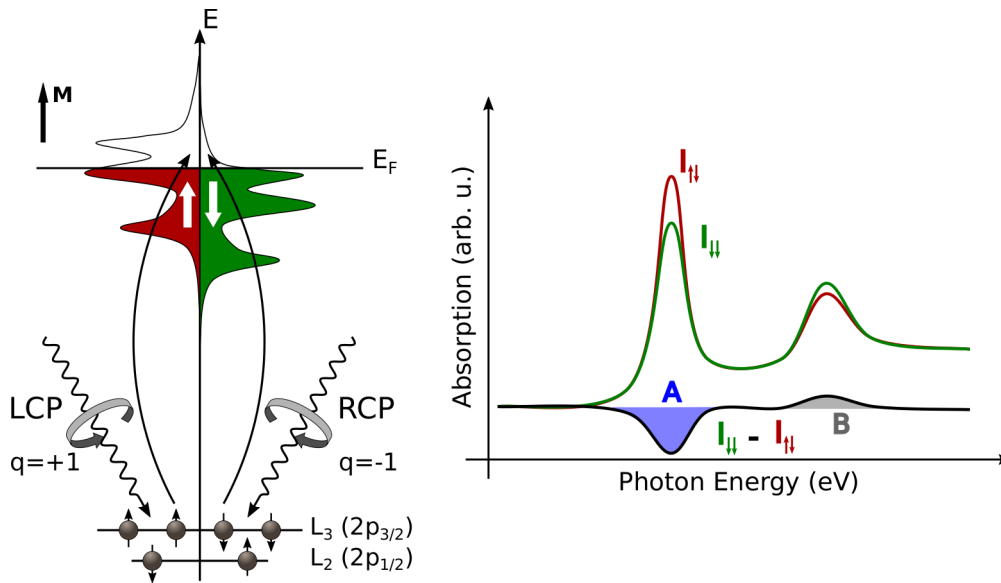


Fig. 2.6.: (Left) Schematic of the two step model of XMCD in the one-electron picture. The circularly polarized light induces a spin polarization in the photoelectrons and the magnetization of the sample shifts the relative position of majority and minority spin bands. (Right) The resulting absorption spectra, in the case of the photon spin being parallel to the spin of the majority electrons ($I_{\downarrow\downarrow}$) and the photon spin being antiparallel to the spin of the majority electrons ($I_{\uparrow\downarrow}$), show differences at the respective absorption edges. The areas under the difference spectrum are labelled.

In general it can be said that the strength of the XMCD depends on the number of spin polarized electrons and the occupation imbalance of electrons with different momentum orientations in the valence band. This can be summarized as:

$$I_{XMCD} = I_{\downarrow\downarrow} - I_{\uparrow\downarrow} = \sigma^+ - \sigma^- \propto \vec{\varepsilon} \cdot \vec{M} \quad (2.2.9)$$

Where the second definition is done for brevity's sake. From (2.2.9) it can be seen that either switching majority spin direction or the direction of the polarization vector has the same effect on the XMCD, since the strength of the XMCD effect depends on the relative direction of these quantities. The same can be seen from (2.2.8), where exchanging m with $-m$ for a given photon helicity has the same effect as going from $q = +1$ to $q = -1$ while keeping m_l fixed.

2.2.1.1. Sum Rules

While the XMCD signal is already very useful by itself, in that it can give insight into the strength of spin and orbital momentum imbalances in the valence states of a material, it became even more powerful by the introduction of the theoretical results known as the sum rules. Using spherical tensor and graphical methods, Carra, Thole *et al.* were able to derive relationships between the respective areas under the XMCD edges and the expectation values of the orbital and spin momentum operator [10, 11]. For the $2p \rightarrow 3d$ process relevant to this work, they read:

$$\langle L_z \rangle = 2n_h \hbar \frac{\int_{L_2+L_3} (\sigma^+ - \sigma^-) dE}{\int_{L_2+L_3} (\sigma^+ + \sigma^- + \sigma^0) dE} \quad (2.2.10)$$

$$\langle S_z \rangle + \frac{7}{2} \langle T_z \rangle = \frac{3}{2} n_h \hbar \frac{\int_{L_3} (\sigma^+ - \sigma^-) dE - 2 \int_{L_2} (\sigma^+ - \sigma^-) dE}{\int_{L_2+L_3} (\sigma^+ + \sigma^- + \sigma^0) dE} \quad (2.2.11)$$

Where n_h is the number of unoccupied electrons in the valence states, or for this work in particular, the number of d -holes. In addition to the spin-dependent absorption cross sections σ^\pm , there also appears the absorption independent of the spin, known as the white line and denoted by σ^0 . For the entirety of this work, it is going to be expressed as $\sigma_0 = (\sigma_+ + \sigma_-)/2$. Thus, the sum rules can be rewritten:

$$\langle L_z \rangle = \frac{4}{3} n_h \hbar \frac{\int_{L_2+L_3} (\sigma^+ - \sigma^-) dE}{\int_{L_2+L_3} (\sigma^+ + \sigma^-) dE} \quad (2.2.12)$$

$$\langle S_z \rangle + \frac{7}{2} \langle T_z \rangle = n_h \hbar \frac{\int_{L_3} (\sigma^+ - \sigma^-) dE - 2 \int_{L_2} (\sigma^+ - \sigma^-) dE}{\int_{L_2+L_3} (\sigma^+ + \sigma^-) dE} \quad (2.2.13)$$

The expectation value of the spin momentum $\langle S_z \rangle$ is combined with $\langle T_z \rangle$, the expectation value of the magnetic dipole operator. This operator is given by [5, 29]

$$\begin{aligned} \vec{T} &= \vec{S} - 3\hat{r}(\hat{r} \cdot \vec{S}) \\ &= \frac{1}{2}(\underline{Q}^\dagger - \underline{Q}^\downarrow) \cdot \hat{S} \end{aligned} \quad (2.2.14)$$

with \underline{Q} the quadrupole tensor of the charge in the valence states and \hat{S} the unit vector in the direction of the magnetization. This means that $\langle T_z \rangle$ is a measure of anisotropy of the charge density in the valence states, effectively coupling the spin of the valence orbitals to their respective charge distribution. It should be noted that the second equality only holds in the case that the spin-orbit contribution to the magnetic dipole term can be neglected. For the $3d$ metals in this work, this is generally true [29].

The $\langle T_z \rangle$ term vanishes from the equation for the spin moment in the case of a crystal of cubic symmetry, if measurements along all three cartesian axes are summed or if the photon angle of

incidence corresponds to the "magic angle" of 54.7° [5]. However, none of this was the case in this work, and the sum of the two contributions was evaluated.

Using (2.1.2) and (2.1.3), naming the areas under XMCD curve according to Fig. 2.6 and defining the area under the sum of the two spectra as C , the sum rules can be rewritten into:

$$\begin{aligned} m_L &= -\frac{4}{3}n_h \frac{A+B}{C} \mu_B \\ m_S^{eff} &= -2n_h \frac{A-2B}{C} \mu_B \end{aligned} \tag{2.2.15}$$

The superscript for the spin moment was introduced as a reminder of the contribution of the dipole magnetic term. The sum rules as stated here cover only the $2p \rightarrow 3d$ transition and hence it has to be assured that e.g. the dipole allowed $p \rightarrow s$ transitions are removed from σ^\pm . While the $p \rightarrow s$ transitions should not show any spin imbalance and hence the areas A and B should not suffer from such contributions, for the determination of area C , this is very important. The contribution of these excitation processes, as well as those into higher conduction states, are modelled as a sharp step function for each respective L -edge, leading to a double step function. To account for the experimental resolution, the sharp steps should be convoluted with a Gaussian function, ultimately leading to the continuum step being the sum of two error functions. Another possibility to model these transitions is by convoluting the steps with a Lorentzian, simulating the lifetime of the core hole. This would lead to the transitions being modelled as the sum of two arctangent functions. In any case, the placement of these steps should be such that the respective inflection points of each step corresponds to the inflection points of the $L_{2,3}$ peaks [21]. The subtraction of this continuum step is also important for the correct determination of the branching ratio between the two L -edges (cf. 2.2.3).

$$\frac{m_L}{m_S^{eff}} = \frac{2}{3} \frac{A+B}{A-2B} \tag{2.2.16}$$

Since the number of valence holes n_h is not accessible experimentally, it is therefore advantageous to use the ratio between the two magnetic moments as a way to compare measurements between different magnetic systems. As evidenced by (2.2.16), this ratio only depends on quantities that can be measured in an XMCD experiment and furthermore it is independent of the area under the white line, which eliminates a potential source of errors.

2.2.2. Angle dependency

In the context of this work it is especially important to talk about the angular evolution of the XAS and XMCD signals. Relations between the photon angle of incidence and the transition matrix elements of $s \rightarrow p$ transitions [21] and more general ones [30] have been established in the course of the years and in general it can be stated that a dipole excitation of an electron from a core state to a particular valence state is sensitive to the spatial form of the valence state. This can be described as a kind of "search light effect" in that the electrons excited by the dipole electric field are ejected in a direction parallel to said field and that the absorption

strength depends on whether or not the unoccupied valence state can take in electrons coming from that direction [5].

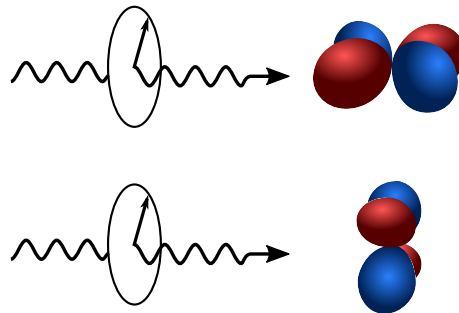


Fig. 2.7.: Schematic example of the angular dependence of X-ray absorption strength. The upper case leads to a weak signal, since the electric field lies in a plane perpendicular to the plane of the orbital. For the lower case, one would expect a higher absorption signal.

More specifically, the absorption into an unoccupied d -orbital is strongest if the electric field lies in the plane of the orbital⁶. Given that the electric field is perpendicular to the photon wavevector, this implies that e.g. for a photon beam moving in the z -direction the electron excitation is strongest into the d_{xy} and $d_{x^2-y^2}$ orbitals while it is weak into the d_{xz} and d_{yz} orbitals. This is sketched in Fig. 2.7.

It was shown by Stöhr, that this effect can be traced back to the expectation values of the charge quadrupole tensor \underline{Q} of the valence state (cf. (2.2.14) and [5, 31]), and that for any given direction, the sum of the contributions of the d -orbitals to the total absorption is equal if the orbitals are equally likely to be the final state of an excitation. Intuitively, this result makes sense since one would not expect an angular dependence of the absorption strength in an isolated atom where all the d -states are degenerate and not fully occupied. If however some of the valence states are fully occupied, then there will be no excitation into those states and the absorption will show an angular dependency, becoming weaker at angles corresponding to excitations into these orbitals. Another possibility is to break the degeneracy of the valence states by an external field e.g. the crystal field created by neighbouring atoms. This lowers the energy of some orbitals with respect to others, splitting the absorption line and giving it an angular dependence in the process. It can thus be said that the photon angle of incidence in an absorption probes the contribution of non-degenerate orbitals with different spatial orientations, revealing insight into the occupancy of the states and the geometric environment of the probed atom.

In addition to gauging the contribution of different valence states, changing the incidence angle of the X-rays on the sample can have a directly measurable effect on the magnetic moments gained from use of the sum rules (2.2.15). In a magnetic field strong enough to align all the electron spins, the measured spin moment should be independent of the direction of light incidence, since it would just measure the difference between spins parallel and antiparallel to

⁶This excludes d_{z^2} , which does not have a plane per se. The angular dependence is more complicated in that case.

the magnetic field. It is only through the dipole magnetic moment, and hence the anisotropic charge density in Q (cf. (2.2.14)), that the spin gains its angle dependence [5, 29].

For the orbital magnetic moment, the angle dependence stems from the spin-orbit interaction. Real-valued atomic valence orbitals will always contain an equal number of spherical harmonics with m_l and $-m_l$, leading to no net orbital motion or momentum. The spin-orbit coupling serves to couple these orbitals and breaks the the symmetry of the different orbital motions. If the spin-orbit coupling is not isotropic, this induces an anisotropic orbital motion in the resulting orbitals, and leads to different orbital magnetic moments in the valence orbitals [18]. This means that the determination of the spin moment via the sum rules for different light incidences can give insight into the anisotropy of charge, spin and orbital moments of the valence bands.

2.2.3. Branching ratio

Another way to gain insight into the electronic structure of materials with the help of XAS, comes in the form of the branching ratio. It is given by ratio of the area under the L_3 peak and the area under the complete spin-independent spectrum:⁷:

$$B = \frac{\int_{L_3} (\sigma^+ + \sigma^-) dE}{\int_{L_2+L_3} (\sigma^+ + \sigma^-) dE} \quad (2.2.17)$$

As can be seen from (2.2.17), this is a measure of the intensity of $l \rightarrow l + 1$ transitions originating from one of the two spin-orbit split manifolds of the core state. Statistically, it would be expected that for a state of total angular momentum $j = l \pm s$, the relative intensity is given by [32]:

$$B_0 = \frac{2j + 1}{2(2l + 1)} \quad (2.2.18)$$

Which evaluates to 2/3 (1/3) for the $2p_{3/2}$ ($2p_{1/2}$) states in this work. However, significant deviations from B_0 were found for the absorption spectra of $3d$ materials [33, 34] and Thole *et al.* were able to show for atomic $p \rightarrow d$ transitions that, indeed, the branching ratio should be calculated via [35]:

$$B_j(\Psi) = B_0 \mp \frac{1}{3(10 - n)} \langle \Psi | \sum_i \vec{l}_i \cdot \vec{s}_i | \Psi \rangle \quad (2.2.19)$$

With the wavefunction of the initial state Ψ , the number of electrons in the valence band before the excitation n and \mp corresponding to $j = l \pm s$. This shows, that for atomic systems, the transition intensity of a given L -edge depends on the angular expectation value of the spin-orbit interaction and leads to the formulation of the rule, that many-electron states with higher spin have a higher branching ratio than states with low spin and that the branching ratio is highest

⁷Another definition of the branching ratio is often used in the literature, namely the area under the L_3 peak divided by the area under L_2 peak, however the former definition will be used in this work

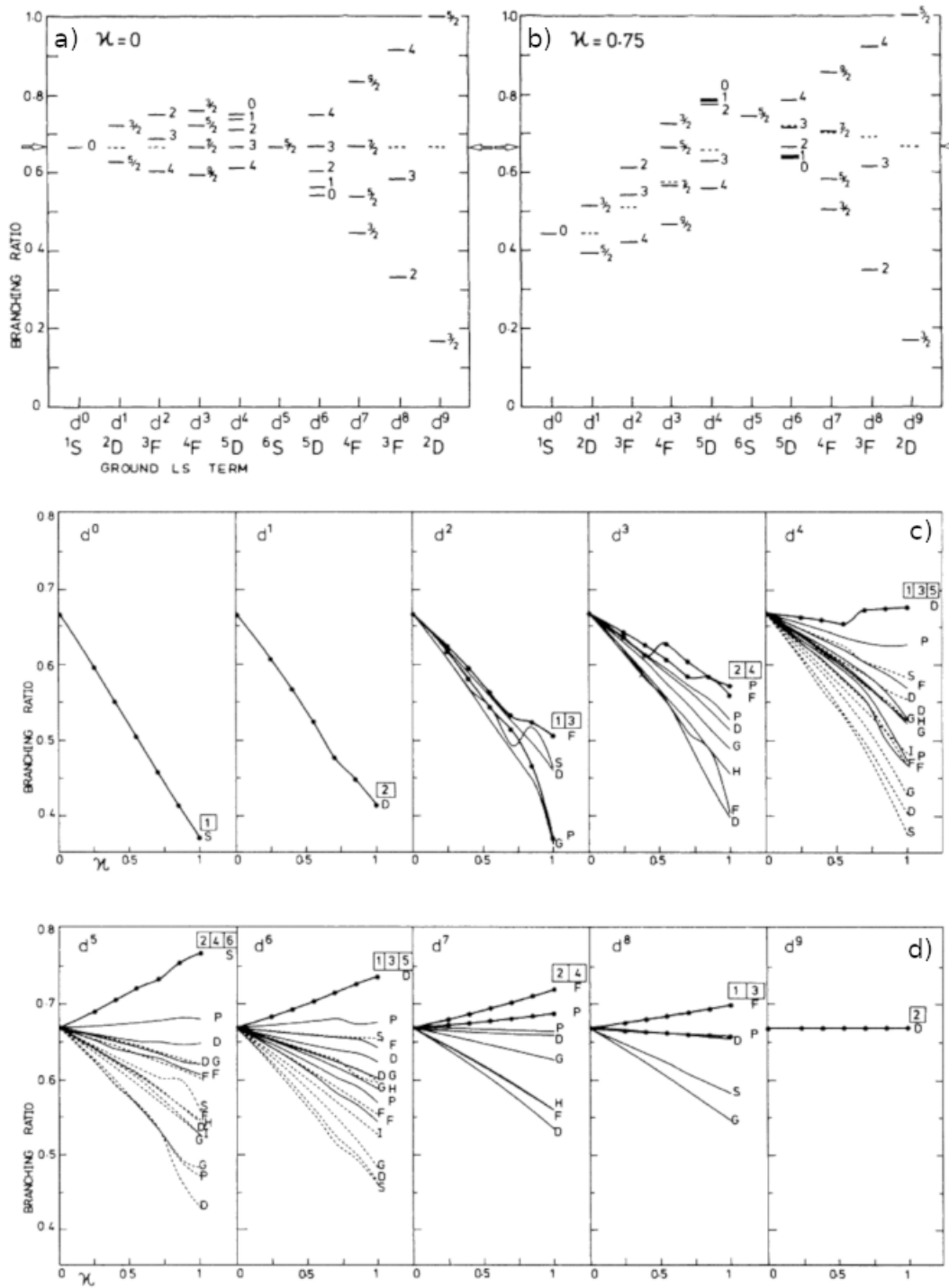


Fig. 2.8.: Branching ratios of the different total angular momentum levels of the d^n ground state terms for a) $\kappa = 0$ and b) $\kappa = 0.75$. Shown in c) and d) are average branching ratios of the d^n terms as a function of κ . The numbers indicate the spin multiplicity $2S + 1$ and the spin of the depicted states decreases from lines with markers, to continuous lines to dashed lines. Taken from [35].

for the ground state term obtained by Hund's rules. This can be seen from the calculations for the ground state terms of the d^n configurations in panels a) and b) of Fig. 2.8 [35].

In addition to this, the branching ratio is also influenced by the electrostatic interaction between the $2p$ and $3d$ states. These interactions are quantified by κ , which gives the amount of reduction of the atomic Slater integrals [36]. $\kappa = 1$ then signifies the unreduced atomic Slater integrals, valid for an atom with two electrons. $\kappa = 0$ is most appropriate for a large amount of hybridization of the orbitals, which occurs in $4d$ and $5d$ metals and for $3d$ materials, a κ of roughly 0.75 has proven effective in calculations.

The calculations of the branching ratios have become more sophisticated since those first papers by Thole *et al.* (cf. for example [37, 38]) but it is still possible to identify ground states of differing spin just by using (2.2.17) without the need for involved calculations. As the branching ratio depends on the area under the experimental absorption curves, removal of the step function resulting from transitions into continuum states is essential to achieve correct results.

2.3. Crystal Fields

2.3.1. Point Charge Model

Following the work of Rao and Waber [39], the effect of the crystal surface on the electronic states of the approaching adatom is represented by a collection of point charges at the lattice points of the surface. Restricting the calculations to the five nearest neighbours of the approaching atom, Fig. 2.9 shows the fourfold symmetric (001) surface of fcc Cu. The form of the crystal field operator is that of a sum of Coulomb terms between the approaching electron and the lattice point charges.

$$V_{CF}(\vec{r}) = -Ze^2 \sum_{i=0}^N \frac{1}{|\vec{r} - \vec{r}_i|} \quad (2.3.1)$$

Here, the coordinate origin moves with the adatom, h is the height of the adatom above the surface, \vec{r}_i is the vector connecting the i -th point charge to the origin and the distance parameter d is equal to half the lattice constant of Cu. The surface electrons are delocalized between the atoms, which leads to a slight lack of negative charge on each atom. This is taken in to account by giving the lattice points a positive charge of Ze . The coordinates of the lattice points are collected in the first three columns of Tab. 2.2.

While it is perfectly reasonable to deduce the form of the crystal field operator from this, there is a way that lends itself to generalization and along the way, simplifies the calculation. Starting with expanding $1/r$ -type potential in terms of spherical harmonics (e.g. [40]):

$$V_{CF}(\vec{r}) = -Ze^2 \sum_{k=0}^{\infty} \frac{4\pi}{2k+1} \sum_{q=-k}^k \sum_{i=0}^N \frac{r_{<}^k}{r_{>}^{k+1}} Y_q^{k*}(\theta_i, \phi_i) Y_q^k(\theta, \phi) \quad (2.3.2)$$

Here, $r_{<}$ ($r_{>}$) is the smaller (larger) of r and r_i . The distance between the approaching adatom and the surface atoms is generally larger than the point at which the potential is evaluated, therefore $r_{<} = r$ and $r_{>} = |\vec{r}_i|$. The parameters θ_i and ϕ_i are determined by converting the

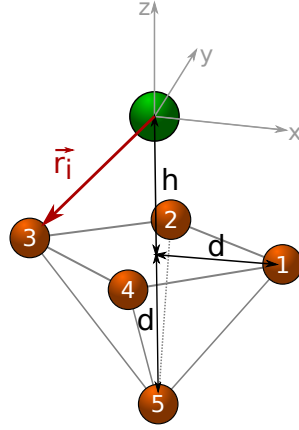


Fig. 2.9.: Schematic representation of the point charge model of an adatom approaching a four-fold symmetric surface and its nearest neighbours. The distance parameter d is equal to half the lattice constant for a fcc lattice and each atom of the crystal carries a charge of $+Ze$.

i	x_i	y_i	z_i	$ \vec{r}_i $	$\cos \theta_i$	ϕ_i
1	d	0	$-h$	$R_1 = \sqrt{h^2 + d^2}$	$\beta = -\frac{h}{R_1}$	0
2	0	d	$-h$	R_1	β	$\frac{\pi}{2}$
3	$-d$	0	$-h$	R_1	β	π
4	0	$-d$	$-h$	R_1	β	$-\frac{\pi}{2}$
5	0	0	$-h-d$	$R_2 = h + d$	-1	0

Tab. 2.2.: Cartesian coordinates (first three columns) and parameters in spherical coordinates (latter three columns) of the five point charges in Fig. 2.9.

coordinates of each lattice point into spherical coordinates and are tabulated in the latter three columns of Tab. 2.2. Defining a new function B_q^k , using $Y_q^{k*} = (-1)^q Y_{-q}^k$, and switching to Racah's spherical tensors (cf. 2.2), it follows:

$$V_{CF}(\vec{r}) = \sum_{k=0}^{\infty} \sum_{q=-k}^k B_q^k(r) C_q^k(\theta, \phi) \quad (2.3.3)$$

where

$$B_q^k(r) = (-1)^{q+1} Z e^2 r^k \sqrt{\frac{(k+q)!}{(k-q)!}} \sum_{i=1}^N \frac{e^{-iq\phi_i}}{|\vec{r}_i|^{k+1}} P_{-q}^k(\cos \theta_i) \quad (2.3.4)$$

With the parameters from Tab. 2.2 as well as the identities $e^{iq0} = 1$, $e^{iq\pi} = (-1)^q$ and $e^{iqx} + e^{-iqx} = 2 \cos qx$, it is then:

$$B_q^k(r) = (-1)^{q+1} Z e^2 r^k \sqrt{\frac{(k+q)!}{(k-q)!}} \left(\frac{1}{R_1^{k+1}} P_{-q}^k(\beta) \left(1 + (-1)^q + 2 \cos q \frac{\pi}{2} \right) + \frac{1}{R_2^{k+1}} P_{-q}^k(-1) \right) \quad (2.3.5)$$

Using a perturbation theory approach, the new levels can be obtained by calculating the matrix elements of the perturbation operator, in this case the crystal field, in the basis of the unperturbed d -states and diagonalizing the resulting matrix.

$$\langle l, m_l | V_{CF} | l', m_l' \rangle = \sum_{k=0}^{\infty} \sum_{q=-k}^k B_q^k \langle l, m_l | C_q^k(\theta, \phi) | l', m_l' \rangle \quad (2.3.6)$$

Making use of the last step in (2.2.6) and (2.2.7), this can be rewritten as the product of two 3- j symbols. For the matrix elements between two d -electrons, $l = l' = 2$ and the 3- j symbol in Eq. (2.2.7) vanishes if k is odd or if $k > 4$. This leaves the cases where $k = 0, 2, 4$. Furthermore, Eq. (2.3.5) restricts the range of values that q may take due to the symmetry the cosine function and the associated Legendre polynomials. In fact, the only non-vanishing B_q^k have $q = -4, 0, 4$. With these informations, the crystal field operator then simplifies to:

$$V_{CF}(\vec{r}) = B_0^0 + B_0^2(r)C_0^2(\theta, \phi) + B_0^4(r)C_0^4(\theta, \phi) + B_4^4(r) \left(C_4^4(\theta, \phi) + C_{-4}^4(\theta, \phi) \right) \quad (2.3.7)$$

With the crystal field parameters being of the form:

$$B_0^0 = -4Ze^2 \left(\frac{1}{R_1} + \frac{1}{4R_2} \right) \quad (2.3.8a)$$

$$B_0^2 = -2Ze^2 \left(\frac{3\beta^2 - 1}{R_1^3} + \frac{1}{2R_2^3} \right) \langle r^2 \rangle_{3,2} \quad (2.3.8b)$$

$$B_0^4 = -Ze^2 \left(\frac{35\beta^4 - 30\beta^2 + 3}{2R_1^5} + \frac{1}{R_2^5} \right) \langle r^4 \rangle_{3,2} \quad (2.3.8c)$$

$$B_4^4 = -\frac{\sqrt{70}}{4R_1^5} Ze^2 (1 - \beta^2)^2 \langle r^4 \rangle_{3,2} = B_{-4}^4 \quad (2.3.8d)$$

Finally, the matrix elements from Eq. (2.3.6) can be written as:

$$\begin{aligned} \langle l, m_l | V_{CF} | l, m_l' \rangle &= 5(-1)^{m_l} B_0^0 \begin{pmatrix} 2 & 0 & 2 \\ 0 & 0 & 0 \end{pmatrix} \begin{pmatrix} 2 & 0 & 2 \\ -m_l & 0 & m_l' \end{pmatrix} \\ &+ 5(-1)^{m_l} B_0^2 \begin{pmatrix} 2 & 2 & 2 \\ 0 & 0 & 0 \end{pmatrix} \begin{pmatrix} 2 & 2 & 2 \\ -m_l & 0 & m_l' \end{pmatrix} \\ &+ 5(-1)^{m_l} B_0^4 \begin{pmatrix} 2 & 4 & 2 \\ 0 & 0 & 0 \end{pmatrix} \begin{pmatrix} 2 & 4 & 2 \\ -m_l & 0 & m_l' \end{pmatrix} \\ &+ 5(-1)^{m_l} B_4^4 \begin{pmatrix} 2 & 4 & 2 \\ 0 & 0 & 0 \end{pmatrix} \left[\begin{pmatrix} 2 & 4 & 2 \\ -m_l & -4 & m_l' \end{pmatrix} + \begin{pmatrix} 2 & 4 & 2 \\ -m_l & 4 & m_l' \end{pmatrix} \right] \quad (2.3.9) \end{aligned}$$

The values for the relevant 3- j symbols can be found in Appendix A. The eigenvalues of the resulting matrix are the energy levels of the irreducible representations of the C_{4v} point group. They can be found in Eq. (2.3.10).

$$E_{b_1} = B_0^0 - \frac{2}{7}B_0^2 + \frac{1}{21}B_0^4 + \frac{\sqrt{70}}{21}B_4^4 \quad (2.3.10a)$$

$$E_e = B_0^0 + \frac{1}{7}B_0^2 - \frac{4}{21}B_0^4 \quad (2.3.10b)$$

$$E_{a_1} = B_0^0 + \frac{2}{7}B_0^2 + \frac{6}{21}B_0^4 \quad (2.3.10c)$$

$$E_{b_2} = B_0^0 - \frac{2}{7}B_0^2 + \frac{1}{21}B_0^4 - \frac{\sqrt{70}}{21}B_4^4 \quad (2.3.10d)$$

The crystal field parameters B_q^k can be related to Dq , Ds and Dt of Ballhausen via [41]:

$$B_0^2 = -7Ds \quad (2.3.11a)$$

$$B_0^4 = 21(Dq - Dt) \quad (2.3.11b)$$

$$B_4^4 = 21\sqrt{\frac{5}{14}}Dq \quad (2.3.11c)$$

So that in the end, the expressions for the energy levels of the representations can be written:

$$E_{b_1} = B_0^0 + 6Dq + 2Ds - Dt \quad (d_{x^2-y^2}) \quad (2.3.12a)$$

$$E_e = B_0^0 - 4Dq - Ds + 4Dt \quad (d_{xz}, d_{yz}) \quad (2.3.12b)$$

$$E_{a_1} = B_0^0 + 6Dq - 2Ds - 6Dt \quad (d_{z^2}) \quad (2.3.12c)$$

$$E_{b_2} = B_0^0 - 4Dq + 2Ds - Dt \quad (d_{xy}) \quad (2.3.12d)$$

Where the d -orbitals corresponding to each of the irreducible representations are indicated in parenthesis. The evolution of these energy expressions with the height of the adatom above the surface is shown in Fig. 2.10. The values for $\langle r^2 \rangle_{3,2}$ and $\langle r^4 \rangle_{3,2}$ are free parameters and can be determined via Hartree-Fock calculations, by fitting to experimental data or from evaluating the radial parts of the hydrogenic d -functions. The third approach was chosen, making use of the fact that for hydrogenic radial wavefunctions $R_{n,l}$, the expectation values $\langle r^k \rangle_{n,l}$ can be computed via the Kramers relation [42]:

$$(k+1)\frac{Z^2}{n^2}\langle r^k \rangle_{n,l} - (2k+1)Za_0\langle r^{k-1} \rangle_{n,l} + \frac{k}{4}[(2l+1)^2 - k^2]a_0^2\langle r^{k-2} \rangle_{n,l} = 0 \quad (2.3.13)$$

Because the $R_{n,l}$ are normalized, i.e. $\langle r^0 \rangle_{n,l} = 1$, the recursion can be started at $k=0$ and in the end we have for $\langle r^2 \rangle_{n,l}$ and $\langle r^4 \rangle_{n,l}$ [43]:

$$\begin{aligned} \langle r^2 \rangle_{n,l} &= \left(\frac{a_0}{Z}\right)^2 \frac{n^2}{2} [5n^2 - 3l(l+1) + 1] \\ \langle r^4 \rangle_{n,l} &= \left(\frac{a_0}{Z}\right)^4 \frac{n^4}{8} [63n^4 - 35n^2(2l^2 + 2l - 3) + 5l(l+1)(3l^2 + 3l - 10) + 12] \end{aligned} \quad (2.3.14)$$

With the Bohr radius a_0 .

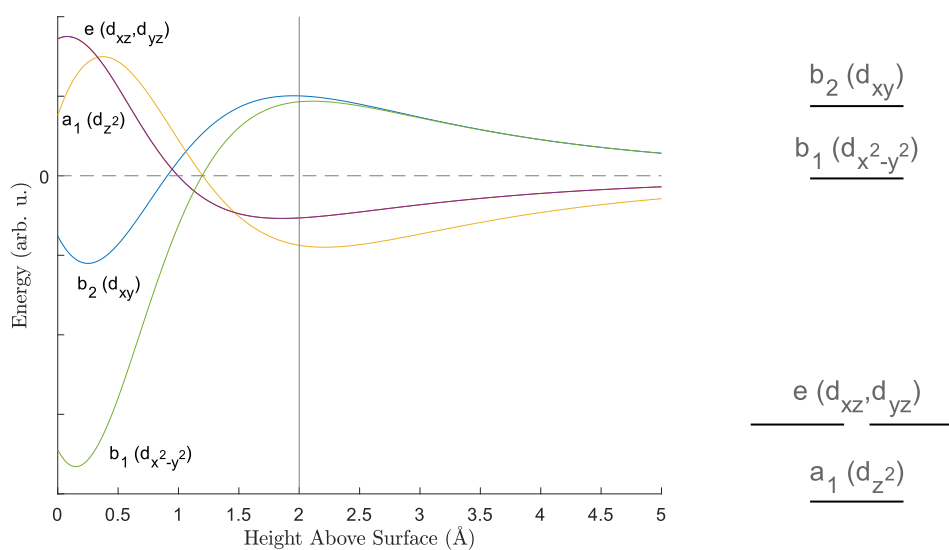


Fig. 2.10.: (Left) Results of Eq. (2.3.12) for the approaching atoms d -electrons, with the constant shift B_0^0 removed. The d -orbital designation in parenthesis shows, which symmetry each irreducible representation follow. (Right) Energy level diagram, taken as a cut through the curves on the left at $h=2 \text{ \AA}$ (cf. vertical bar). The level separations are not to energetic scale.

2.3.2. Spin crossover

While for the free atom, the electrons will follow Hund's rules and occupy the d -orbitals in a way to maximize spin and orbital momentum of a degenerate d^n configuration (cf. 2.1.2). The same does not necessarily hold for electrons if the degeneracy is lifted. Measurements by Cambi and Szegő have shown that the magnetic susceptibility of organometallic complexes containing $3d$ transition metals will deviate substantially from the free atom case [44]. The reason for this is that in the case of coordinated metal ions, regardless of orbital momentum, the first d -electron will occupy the orbital lowest in energy. The remaining electrons will then fill up the higher orbitals (or irreducible representations, to keep with the terminology of group theory), where the filling pattern depends on the energetic separation of the orbitals, and hence the nature of the crystal field. If the crystal field splitting between irreducible representations is higher than the energy required to pair opposing spins, the electrons will preferably fill lower lying crystal field orbitals, leading to a state of lower spin multiplicity. A textbook example of this are transition metals in octahedral (O_h) environments and the appearance of so called high spin states and low spin states for $d^4 - d^7$ [13, 45].

There is, however, nothing particularly unique about the octahedral environment, and other geometries do allow for these type of spin states [46, 47]. Starting, for example, from the energy level scheme in Fig. 2.10 and filling always the lowest possible irreducible representation, one arrives the configurations shown in Tab. 2.3. A possible splitting into a high spin and a low spin state already appears for d^2 and persists up until d^8 . Furthermore, for d^5 and d^6 there are actually three states of different spin, meaning that there is also an intermediate spin state. It should be noted, that the listed configurations are of course not the only ones possible for each

number of d -electrons, e.g. one could create an $(a_1)^1(e)^2$ configuration with $S = 0$ simply by having one of the the electrons be of opposite spin. The shown configurations are however the energetically favorable ones, given the respective spin pairing energy and the crystal field strength.

d^n	configuration	S
d^1	$(a_1)^1$	1/2
d^2	$(a_1)^2, (a_1)^1(e)^1$	0,1
d^3	$(a_1)^2(e)^1, (a_1)^1(e)^2$	1/2,3/2
d^4	$(a_1)^2(e)^2, (a_1)^1(e)^2(b_1)^1$	1,2
d^5	$(a_1)^2(e)^3, (a_1)^2(e)^2(b_1)^1, (a_1)^1(e)^2(b_1)^1(b_2)^1$	1/2,3/2,5/2
d^6	$(a_1)^2(e)^4, (a_1)^2(e)^3(b_1)^1, (a_1)^2(e)^2(b_1)^1(b_2)^1$	0,1,2
d^7	$(a_1)^2(e)^4(b_1)^1, (a_1)^2(e)^3(b_1)^1(b_2)^1$	1/2,3/2
d^8	$(a_1)^2(e)^4(b_1)^2, (a_1)^2(e)^4(b_1)^1(b_2)^1$	0,1
d^9	$(a_1)^2(e)^4(b_1)^2(b_2)^1$	1/2
d^{10}	$(a_1)^2(e)^4(b_1)^2(b_2)^2$	0

Tab. 2.3.: Possible electron configurations and resulting total spin S of n d -electrons in the crystal field of C_{4v} symmetry depicted in Fig. 2.9.

Keeping the the nature of the ligand or crystal field fixed, the energetics of such a system can be influenced by external stimuli, leading to the switching of the spin state in a process known as spin crossover (SCO). Reported stimuli are e.g. temperature [48], pressure [49], irradiation with light ("light induced spin state trapping", LIESST)[50] and, more specifically, with soft X-rays ("soft X-ray excited spin state trapping", SOXIESST) [51–53].

3. Experimental Setup

3.1. Cluster Creation and Deposition

The entirety of the experiments in this work are performed in an ultrahigh vacuum (UHV) environment, owing to the fact that contact with ambient air would rapidly lead to oxidation of the substrate or the adsorbates, resulting in altered electronic and magnetic properties (cf. for example [54]). The base pressure was kept at around 10^{-8} mbar in this, the sputter portion of the setup and was reduced to around 5×10^{-10} mbar in the measurement chamber via the use of differential pumping and bakeout procedures to get rid of residual water in the setup.

The main working horse of this thesis is ICARUS, the **I**onic **C**lusters by **A**rgon **s**pUtering **S**ource [55, 56], a photograph and schematic sketch of which can be seen in Fig. 3.1. The main idea behind ICARUS is to create sputter fragments from a chosen bulk target and afterwards use a dipole magnetic field to select the sputter fragments according to their mass-to-charge ratio. The production process of the mass-selected, deposited adsorbates can be split into three parts that shall in the following be treated separately. The descriptions will be kept short and the reader will be referred to the cited work for more in-depth explanations.

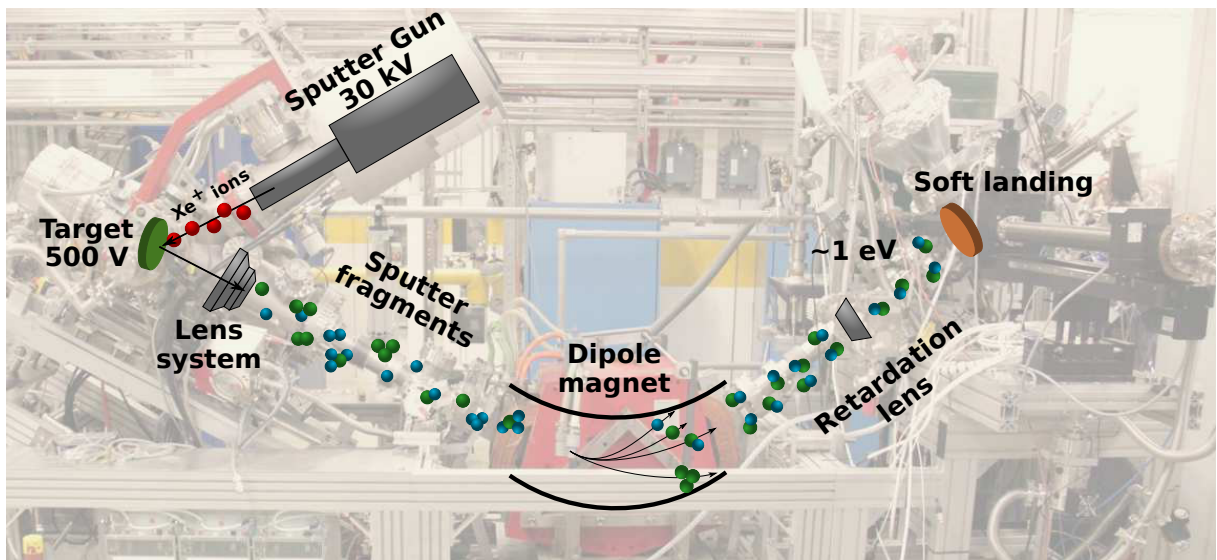


Fig. 3.1.: Picture of the ICARUS setup while mounted at the beamline P04 at PETRA III with the overlay schematically showing the different steps involved in creating mass-selected, deposited clusters.

Fragment Creation

The cluster creation process starts with a rare gas plasma, in the case of this thesis based on Xe. The high voltage of the setup translates to Xe^+ ions with a kinetic energy of around 30 keV. These ions are then focused to a narrow beam and accelerated towards a given sputter target. This target can be chosen rather arbitrarily to suit the experimental needs, and there have been studies performed on clusters from pure targets, e.g. [57], as well as from alloy targets, e.g. [58–60]. Due to the high voltage in the plasma, the Xe^+ ions impinge on the target with a high kinetic energy with the subsequent energy transfer to the target leading to the ablation of fragments from the bulk target. For the present work, the sputter target was a FeV alloy with a 1:1 atom ratio and a purity higher than 99.9 %.

In this so-called sputtering process, a multitude of fragments are created, with the yield of fragments of mass m following a power law $Y(m) \propto m^{-\beta}$. The exponent β varies greatly with the specific sputtering conditions, i.e. the sputter gas, gas pressure, target material etc. It has for example been shown that for Cu targets, $\beta = 2.4$ for an Ar^+ plasma but for a Xe^+ plasma $\beta = 1.0$ [56], meaning that a heavier sputter gas leads to a higher yield of bigger clusters. This is why, contrary to the name of ICARUS, Xe was chosen as a sputter gas in this work rather than Ar.

To ensure that the positively charged sputter fragments leave the interaction region, the sputter target is set to a voltage of $U_{acc} = +500 \text{ V}$ and via a system of electrostatic lenses, the beam of fragments is focused and shaped to ensure optimal passage through the apparatus, especially the upcoming dipole magnet.

Size Selection

The separation process in the ICARUS setup is based on the Lorentz force, enforcing a circular trajectory for charged particles. More specifically, for a magnetic field that is perpendicular to the direction of motion of the particles, equating the expression for the Lorentz force and the centripetal force of the particles gives:

$$\begin{aligned} qevB &= \frac{mv^2}{r} \\ \frac{m}{qe} &= \frac{Br}{v} \end{aligned} \quad (3.1.1)$$

With m , q and v the mass, charge and velocity of the fragments, B the strength of the dipole magnetic field and r the bending radius of the dipole magnet. As the sputter fragments are accelerated by the electric field exerted from the target, their velocity can be gained from the relation:

$$\frac{1}{2}mv^2 = qeU_{acc} \quad (3.1.2)$$

Combining these two equations gives the final expression for the mass-to-charge ratio of the sputter fragments as function of the experimental parameters:

$$\frac{m}{qe} = \frac{B^2 r^2}{2U_{acc}} \quad (3.1.3)$$

Wucher *et al.* have shown that sputter processes such as the one presented in this work lead mainly to the formation of fragments with a single positive charge $q = +1$ [61]. With the bending radius of the dipole magnet fixed and the acceleration voltage set beforehand, this gives a direct relationship between the mass of the sputter fragments that are able pass through the dipole magnet and the applied magnetic field. By scanning the magnetic field strength, it is then possible to obtain spectra of the intensity of a fragment of a given mass, as can be seen in Fig. 3.2. The particular mass spectrum shown was not taken with the dipole magnet of ICARUS but rather at the photon-ion spectrometer at PETRA III (PIPE), which is equipped with the same type of mass selection magnet [62].

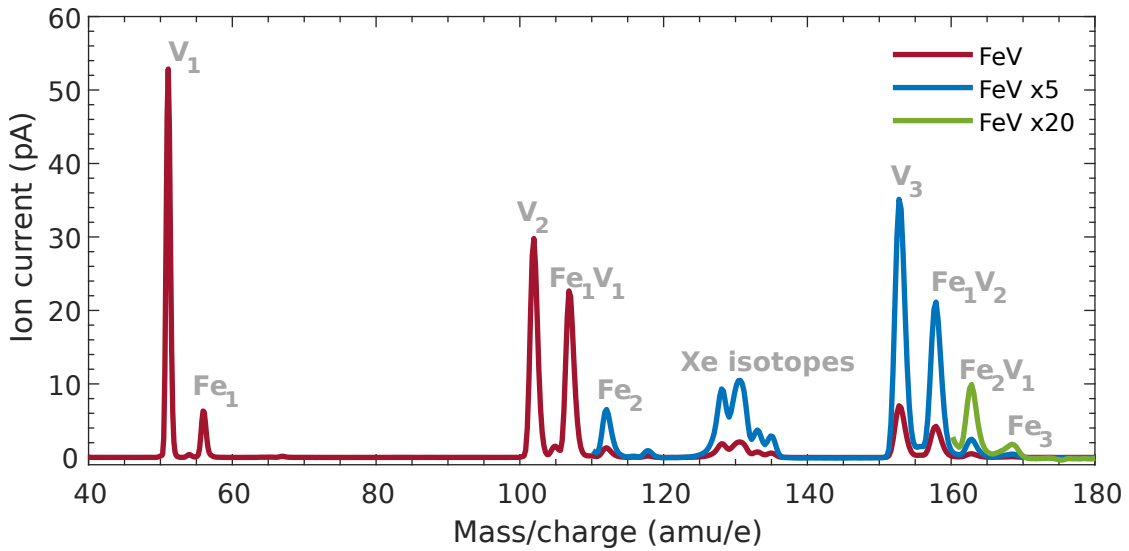


Fig. 3.2.: Exemplary mass spectrum of the size-selected clusters gained from sputtering a FeV target with Xe^+ ions.

Keeping the magnetic field strength at a value matching one of the peaks in Fig. 3.2 allows only one species of fragment through, which forms the basis of the size-dependent deposition of clusters and hence measurements of this work. The dipole magnet was designed to be double focusing, such that a particular point at the entrance of the magnet gets mapped onto a particular point at the exit of the magnet. This is to ensure that the beam of now mass-selected clusters remains focused.

Deposition

At this point, the mass-selected fragments still have their initial kinetic energy of 500 eV and a collision at this energy would damage the substrate as well as lead to fragmentation of the clusters. To avoid this, the substrate is set to a positive bias voltage so as to decelerate the oncoming clusters until they have ~ 1 eV/atom of kinetic energy. At the same time, the cluster

beam is focused further to reach a diameter of ~ 1 mm on the substrate. The reason for this becomes clearer upon examination of the deposition time.

The flux of incoming clusters is measured via the drain current I_c it induces in the, otherwise electrically isolated, substrate. To ensure that the adsorbates stay well separated on the surface, only a small amount of clusters are deposited on the surface, in the present thesis this amount was set to 3% of a monolayer (ML) of substrate. In general, the coverage is expressed as the ratio of adsorbate atoms to surface atoms $\Theta_c = N_{ads}/N_{surf}$. For a cluster with n atoms the number of adsorbate atoms is equal to n times the number of clusters (N_c) that impinge on the substrate. Using the definition of electrical current as charge per unit of time and with the knowledge that each cluster has a charge of $+e$, N_c is written as $N_c = I_c \cdot t_{dep}/e$, with the deposition time t_{dep} . Thus, the number of adsorbate atoms is:

$$N_{ads} = \frac{n I_c t_{dep}}{e} \quad (3.1.4)$$

On the other hand, the number of surface atoms is equal to the surface area (A) times the atom density at the surface (σ), which for the (001) surface of a fcc metal such as Cu with the lattice parameter a_{Cu} is $\sigma = 2/a_{Cu}^2$. $A = \pi/4 \cdot d^2$ because the deposition takes place in a circular spot with diameter d , so that finally the coverage can be written:

$$\Theta_c = \frac{2 I_c t_{dep} n a_{Cu}^2}{\pi e d^2} \quad (3.1.5)$$

Or, by isolating t_{dep} :

$$t_{dep} = \Theta_c \pi \frac{d^2}{2 a_{Cu}^2} \frac{e}{I_c n} \quad (3.1.6)$$

Which shows that for a given substrate geometry and desired coverage, the deposition time decreases with increasing cluster current and with increased cluster size. This also shows that it is sensible to reduce the spot size on the sample, so as to keep the deposition time short and minimize the risk of oxidization or unstable cluster flux. For the adsorbates in the present work, the deposition times ranged from ~ 5 minutes for the monomers up to roughly an hour for the trimers.

To make sure that there are neither residues of previous depositions nor molecules of gas adsorbed on the Cu crystal's (001) surface, it is treated with several sputter cycles before each deposition. Each sputter cycle consists of a 30 minute bombardment with Ar^+ ions with a kinetic energy of 1.4 keV and a subsequent heating to roughly 900 K for 3 minutes to ensure that the surface anneals back to its ideal structure. The sample temperature is monitored via a type K thermocouple spot welded to the sample crystal and the surface structure is regularly checked with low energy electron diffraction (LEED).

As the kinetic energy of the incoming fragments is still high enough to cause damage to the substrate and the cluster, a soft landing scheme is employed to further dissipate the kinetic energy [63]. To this end, the substrate is cooled down using liquid He and subsequently dosed with a rare gas, in this case 30 s in an atmosphere of $1-2 \times 10^{-2}$ mbar of Kr, that forms a multilayer matrix on the surface. The incoming clusters collide with the rare gas matrix and in the process lose some of their kinetic energy while coming in contact with the substrate. Fedrigo

et al. have shown such a scheme to strongly reduce fragmentation of deposited clusters [64]. A schematic representation of this soft landing process is shown on the left side of Fig. 3.3.

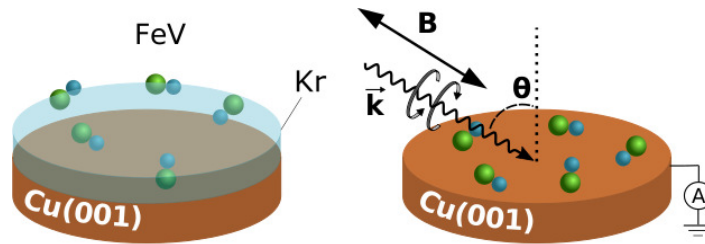


Fig. 3.3.: Schematic of the soft landing process. The FeV dimers, having an energy of ~ 1 eV are colliding with the Kr matrix on the Cu crystal and losing kinetic energy in the process (left). After removing the Kr matrix by flash heating to 120 K, the clusters in contact with the crystal are irradiated with circularly polarized light and subject to a magnetic field (right). θ denotes the photon incidence angle relative to the surface normal.

In addition to providing the necessary temperature for the rare gas to adsorb on the substrate and form the multilayer matrix, the cooling of the Cu crystal has additional uses. For one, the low temperatures are essential in suppressing the diffusion of the adsorbates on the surface and possible agglomeration because of this. It has been shown that such a diffusion process follows an Arrhenius-type law [65] and that at low temperatures the diffusion is essentially blocked, ensuring that the adsorbates keep their size and hence properties. Also, the low temperature stabilizes the alignment of the magnetic moment of the adsorbates, as can be seen from the expression of the magnetization of a paramagnetic system which is a function of the inverse temperature (cf. (2.1.14)).

The optimization of the cluster current is first performed on a metallic pin with a diameter of 1 mm, simulating the cluster spot of the same size on the sample. To ensure that the potential landscape at this pin is comparable to the sample crystal, the pin is surrounded by a ring of the same material and size as the sample. This whole configuration is electrically isolated from the rest of the sample holder system and placed 16 mm away from the sample crystal (cf. Fig. 3.4).

Once the ideal configuration of lens voltages and geometric parameters found on the pin, the sample crystal is moved into the focus spot with a shutter closed, blocking off the cluster beam. The shutter is then opened for the required deposition time, calculated with the optimized cluster current on the pin. After this, a W filament is used to flash heat the sample crystal to temperatures of about 120 K for a couple of seconds via electron bombardment. This desorbs the Kr matrix from the surface, a process which is monitored via a quadrupole mass spectrometer built into the chamber. Despite the temporary increase in temperature, the adsorbates do not aggregate on the surface [63]. This leaves the size-selected adsorbates in direct contact with the surface and ready for the measurements.

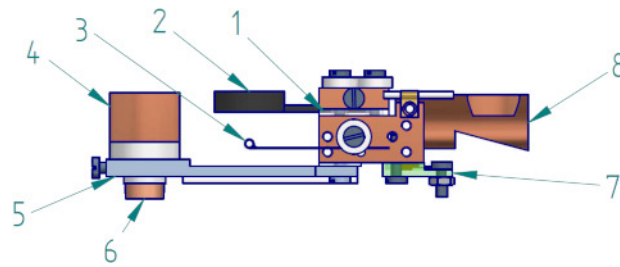


Fig. 3.4.: Schematic side view of the sample holder, courtesy of H. Meyer: (1) Sapphire plate as electrical insulator for the crystal. (2) Sample crystal. (3) W filament as heating device. (4) Ring around detection pin. (5) Bridge holding ring and pin. (6) Pin used for cluster current optimization. (7) Si diode as temperature sensor (not used during these measurements). (8) Connection to the cryostat.

3.2. High Field Magnet Chamber

In earlier measurements, the alignment of the size-selected adsorbate magnetic moments was achieved via remanent magnetic thin films of e.g. Fe or Ni (cf. [57, 58, 60, 66–68]). However, as these thin films exhibit high densities of states at the Fermi edge, they interact strongly with the adsorbates and alter the magnetic properties. In order to gain access to the more intrinsic properties of the adsorbates, even on weakly interacting substrates, a setup was devised that relies on an external magnetic field to align the magnetic moments in question. The resulting endstation was dubbed the High Field Magnet Chamber (dt. "Hochfeldkammer", HFK) and its technical properties can be found in [59].

The crucial part of the HFK setup is the 7 T fast switching magnet, consisting of two superconducting Nb_3Sn solenoids. The coils are each cooled by a separate pulse-tube refrigerator working with high purity He in a closed cycle. In contrast to bath cryostats, there is no boil-off in this setup and the main He losses occur at the moment of connecting or disconnecting the He leads, meaning that the He only has to be refilled rarely. Additionally, the high cooling power of the pulse-tube refrigerators can very effectively counter the high heat load created in the magnet coils when ramping the magnetic field. This in turn allows for magnetic field ramp rates of up to 0.26 T/s, or a full reversal from -7 T to 7 T¹ in about 53 s, without loss of superconductivity in the solenoid coils. In practice however, the ramp rate is kept slightly below this at 0.23 T/s to further reduce the risk of quenching the superconductive state. This still corresponds to a full field reversal in just over a minute, which is considerably faster than for example the 23.3 minutes field sweep time of a bath cryostat [69]. Additionally, this field reversal time is comparable to the duration of a helicity switch of the undulator at P04 at PETRA III [70], so that instead of changing the beam helicity to measure the different spectra needed for an XMCD spectrum, this can now be achieved by switching the magnetic field. This has the advantage that the parameters of the beam are kept constant, reducing potential mismatches of the respective absorption spectra, e.g through slightly shifted beam positions, slight energy deviations or small changes in the degree of circular polarization at different helicities.

Due to the temperature requirements mentioned in the previous subsection, the sample needs

¹A positive magnetic field corresponds to a field directed "downstream" with respect to the incoming photons.

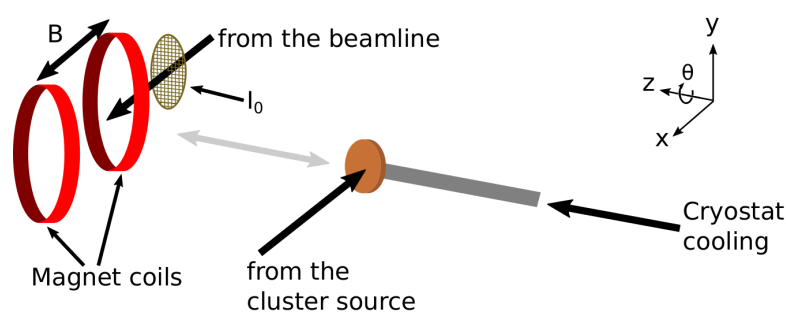


Fig. 3.5.: Schematic visualization of the endstation setup. The cryostat mounted sample holder is moved along the z-axis from the deposition position to the measurement position in the middle the magnetic solenoid pair.

to be cooled at all times. Since the experimental setup is already rather extensive and the space at beamlines is limited, it is impossible to realize the sample holder as a bath cryostat. Rather, the sample is cooled via a constant flow of liquid helium (cf. 3.2.1 for more information). Fig. 3.5 shows a rough sketch of the spatial relation between the position of cluster deposition and the measurement. The sample cryostat is mounted on a 4-axis manipulator, allowing (limited) movement in x- and y-direction as well as 360° rotation of the angle θ . Note that the angle θ is the same that is included in the right-hand side of Fig. 3.3. The variation of this angle is what allows to investigate the adsorbate electronic and magnetic structure in an angle dependent fashion. The magnetic field produced by the coil pair stays collinear to the photon beam from the beamline during the whole measurement process.

Between the end of the deposition and the beginning of the measurement, the sample is rotated by about 180° and moved roughly 0.5 m in z-direction into the crossing of the magnetic field and the synchrotron beam. The photon absorption signal is measured in total electron yield (TEY) by monitoring the drain current on the sample induced by electrons escaping the sample, either through photoexcitation or Auger decay. To this end, the sample is electrically isolated from the cryostat and the rest of the measurement setup via a sapphire plate (cf. Fig. 3.4). The optimal overlap between the adsorbate spot on the substrate and the incoming photons is found by maximizing the absorption at a peak energy specific to the adsorbate.

3.2.1. Cryostat Improvements

Theoretically, the use of liquid helium in combination with its enthalpy of vaporization should allow to cool the sample below the boiling point of He at 4.2 K [71, 72]. In reality however, additional heat load on the sample, e.g. via radiative heating from the chamber, thermal contact to the uncooled exterior as well as heat induced in the sample by the incoming X-rays lead to elevated temperatures. It is therefore of great importance to optimize the cooling of the sample-cryostat system so that any heating of the sample can be countered effectively.

The working mechanism of the flow cryostat is based on connecting one end of the cryostat line to the cryogen reservoir, in this case liquid He, and use a pump to create a vacuum at the other end of the line, thereby forcing the cryogen through the whole of the cryostat body. A schematic representation of this can be found in the upper part of Fig. 3.6. Ideally, the flow of

cryogen through the tube is such that the evaporation of the cryogen takes place right next to the sample mounting, so that further thermal energy is removed from the sample to overcome the enthalpy of evaporation of the cryogen, leading to increased cooling. Otherwise the sample would merely be cooled down through thermal contact with the cryogen in either its liquid or gaseous form.

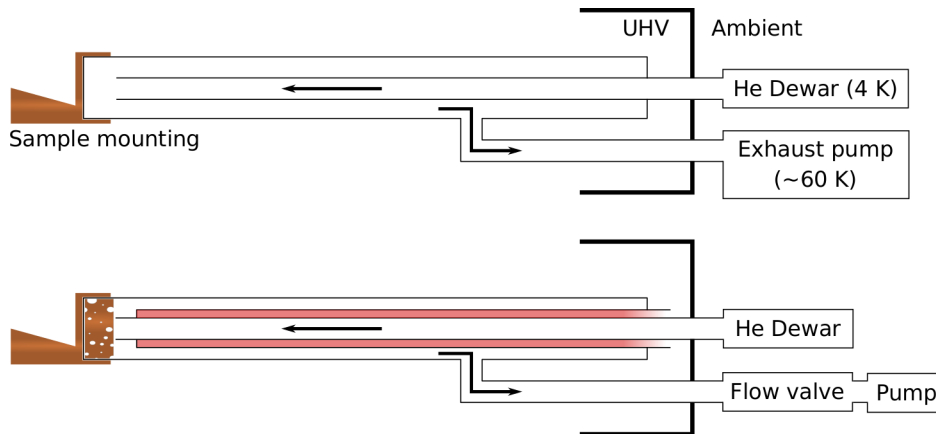


Fig. 3.6.: Schematic representation of the He flow cryostat used in the present thesis (upper part) and the updated version that was designed by Holger Meyer in the course of this work but was not yet fully tested *in operando* (lower part). The changes include a tube connected to the chamber vacuum separating the incoming and outgoing He (highlighted in red), a porous foam-like piece of Cu right next to the sample mounting for increased surface area, and a flow valve to regulate the velocity of He in the cryostat.

In order to optimize the cryogen flow, a mass flow controller (*Teledyne Hastings Instruments HFC-203*) was installed between the end of the cryostat line and the pump. By applying heat to the flowing gas and measuring its temperature before and after the heating element, the sensor of the controller is able to measure the gas flow rate. An internal valve is then operated in proportion to the difference between the measured gas flow rate and a given setpoint, thereby ensuring a constant, well-defined gas flow. To gauge the influence of the gas flow, two temperatures of the sample were measured as a function of the flow setpoint. The first temperature was recorded at the body of the sample holder (cf. (7) in Fig. 3.4) with a *Lakeshore DT-670C-DI* Si diode and the second measurement was taken with the type K thermocouple on the sample crystal itself (cf. (2) in Fig. 3.4).

The results, shown in Fig. 3.7, reveal that the temperature drops exponentially with the flow rate², which could mean that due to heat load on the cryostat, the He boils before it arrives at the point of interaction. It is however unnecessary to leave the flow unrestricted (which equals a flow of roughly 10.88 L/h of liquid He) since above 4.8 L/h the temperature only dropped about 0.2 K in the course of this test. Another interesting result of this test is that while both temperatures show very good agreement below flow rates of 1.5 L/h, the sample does not reach the base temperature of the sample holder, which is directly connected to the cryostat. While the

²The mass flow controller gives the flow as standard liters per minute (SLM) of the exhaust gas. For He, 1 SLM of gas corresponds to roughly 0.08 L/h of liquid.

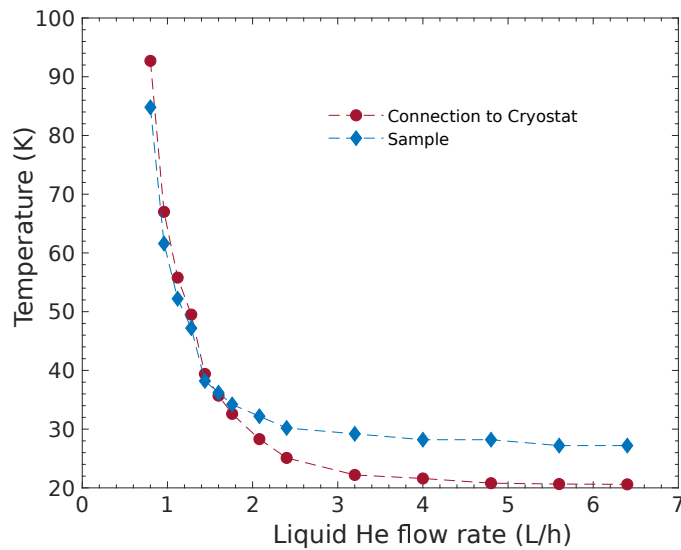


Fig. 3.7.: Sample temperature as a function of cryogen flow for the original cryostat. The red circles represent the temperature at the sample holder (cf. (7) in Fig. 3.4), taken with a Si diode. The blue diamonds show the temperature of the substrate crystal itself (cf. (2) in Fig. 3.4), taken with a type K thermocouple.

type K thermocouples are less reliable on this temperature scale, the difference is too large to be attributed to measurement uncertainty. Rather, this is an indication for the current cooling power of the cryostat not being sufficient to cool the sample effectively. It should also be noted that the measurements shown here are taken with the sample far away from the magnet bore, with the full heat radiation from the chamber impinging on it. Moving the sample into the magnet, for example to start measurements, consistently lowers both temperature readings by roughly 2 K.

Indeed, temperature readings right at the exhaust of the cryostat have revealed a temperature of roughly 60 K for the outgoing He gas. While it is generally desirable for the temperature of the outgoing cryogen to be high [71], in this case this can lead to cooling losses due to the concentric design of the tubes carrying the incoming liquid He and the outflowing gaseous He (cf. upper part of Fig. 3.6). The two are separated by a 1 mm thick stainless steel wall, resulting in significant thermal contact between them. Because of the opposite flow direction, the warmer He gas at the exhaust comes into contact with the liquid He right at the entrance of the tube and the heat transfer can lead to premature evaporation of the liquid He, thereby reducing the cooling power.

To counteract this, a new cryostat was designed, in which the liquid bearing tube is surrounded by a tube that is being evaporated along with the experimental chamber (cf. the red highlighted part in the lower half of Fig. 3.6 for a visualization). This creates an insulating vacuum between the two He species, meaning the conductive heat through the tube wall between them is replaced by radiative heat between the cold inner tube and the warm outer tube. To give an estimate of how strongly this influences the heat load on the system, one can look at the heat flow through a sheet of metal of area A and thickness L , which can be written as [71]:

$$\dot{Q}_{metal} = \frac{A}{2L} \kappa_0 (T_{high}^2 - T_{low}^2) \quad (3.2.1)$$

This is based on the assumption, that the thermal conductivity κ is a linear function of temperature, i.e. $\kappa = \kappa_0 T$. In the case of stainless steel at these low temperatures, the slope κ_0 of this line is about $1.2 \times 10^{-2} \text{ W m}^{-1} \text{ K}^{-2}$ [73]. On the other hand, the heat transfer due to radiation between two so-called grey bodies is given by [71]:

$$\dot{Q}_{rad} = \frac{\epsilon_1 \epsilon_2}{\epsilon_1 + \epsilon_2 - \epsilon_1 \epsilon_2} \sigma A (T_{high}^4 - T_{low}^4) \quad (3.2.2)$$

Again, A is the area of the radiating bodies and $\sigma = 5.670 \times 10^{-8} \text{ W m}^{-2} \text{ K}^{-4}$ is the Stefan-Boltzmann-constant. $\epsilon_{1,2}$ are the respective emissivities of the bodies, measuring the probability of a material to absorb and emit radiation ($\epsilon = 1$ corresponds to the black body). For the case that both bodies are made from the same material, their emissivities are equal and the first fraction can be approximated as $\epsilon/2$. Taking the ratio of (3.2.1) and (3.2.2) then gives:

$$\frac{\dot{Q}_{rad}}{\dot{Q}_{metal}} \approx \frac{\sigma \epsilon L}{\kappa_0} (T_{high}^2 + T_{low}^2) \quad (3.2.3)$$

Assuming a wall thickness of 1 mm, a moderately well polished stainless steel surface with $\epsilon = 0.2$ [71] and setting $T_{high} = 60 \text{ K}$ and $T_{low} = 4 \text{ K}$ gives a ratio of roughly 4×10^{-8} , showing that the new design should vastly reduce the heat load on the He entering the cryostat, thereby improving the cooling power of the cryostat.

An additional change to the cryostat design is the inclusion of a highly porous Cu foam right next to the sample mounting. This is to increase the surface area at the point of evaporation, thus increasing the amount of He evaporating close to the sample and the heat being extracted from the sample in the process.

For all of the sample preparations and measurements in this work, the old cryostat design was used and the flow controller was absent. While there have been no temperature measurements on the sample crystal directly for the new design, preliminary cooling tests have been performed, again using the Si diode for accurate thermometry at the sample mounting spot, without the sample holder itself being mounted. While the earlier version of the cryostat cooled from room temperature down to a base temperature of 8.2 K after in 20 minutes at full He flow, the improved design achieved a base temperature of 5.2 K in only 10 minutes under the same conditions. This shows that, already at the sample mounting stage, the cooling power has improved significantly and heat loads on the cryostat should be countered both more efficiently and more quickly.

3.3. P04 Beamline

All of the absorption measurements of this thesis have been performed at the variable extreme ultraviolet (XUV) beamline P04 at PETRA III, a layout of which can be found in Fig. 3.8 [70]. The PETRA III storage ring in Hamburg is a third generation synchrotron facility with an electron energy of 6 GeV and, due to its small emittance, high brilliance and photon flux [74].

The storage ring is operated in top-up mode, i.e. the electron current in the ring is kept constant within 1 %. This mode has the advantage that the average photon flux of the synchrotron is higher and the beam current is more stable, leading to higher stability in the photon beam parameters and hence more accurate experiments.

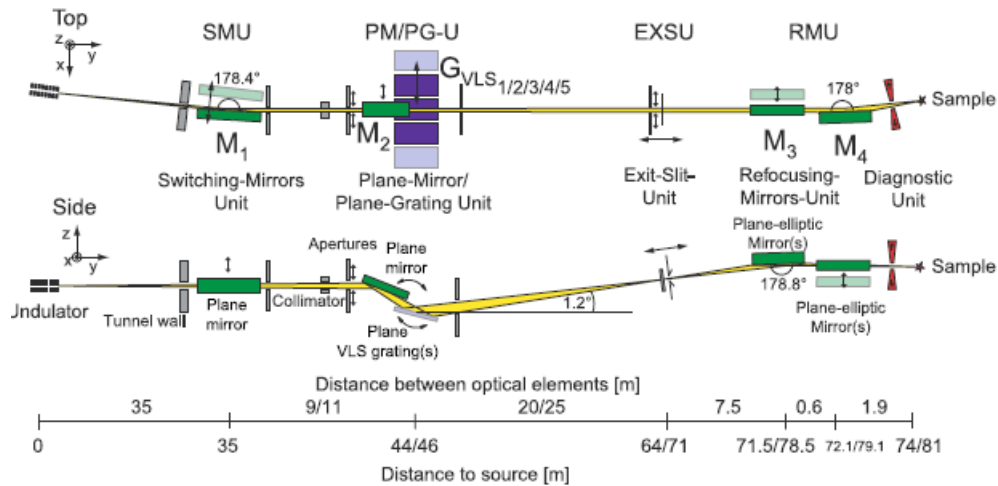


Fig. 3.8.: Layout of the XUV beamline P04 at PETRA III [70]

Starting from these good conditions, P04 uses an APPLE-II (Advanced Planar Polarized Light Emitter) undulator to generate photons in the energy range from 250 eV to 3000 eV, a range which can be covered using just the first harmonic of the undulator because of the high electron energy in the storage ring. This large range of photon energies makes it necessary to have the optics coated in two different materials (Pt and Rh), to ensure that the optics do not have significant absorption in the desired photon energy range [70]. The photon energy can be increased (decreased) via widening (narrowing) the transversal gap between the magnetic arrays of the undulator, as can be seen when looking at the first harmonic undulator equation for on-axis photon generation [75, 76].

$$\begin{aligned}
 E_{ph} &= \frac{4\pi\hbar c\gamma^2}{\lambda_u(1 + K^2/2)} \\
 K &= \frac{B_p e \lambda_u}{m_e c 2\pi} \\
 B_p &\propto \exp(-G/\lambda_u)
 \end{aligned}
 \tag{3.3.1}$$

Where γ is the Lorentz factor and depends on the electron energy in the storage ring (for 6 GeV electrons, $\gamma \approx 11820$), λ_u is the period length of the undulator, K is known as the deflection parameter of the undulator, B_p is the magnetic field strength of the undulator's magnets and G is the transversal gap between the undulator magnets. Furthermore, the APPLE-II allows to introduce a relative longitudinal shift between the opposing magnet arrays, leading to different polarization states of the resulting photons. It has recently been established that, for P04, a positive shift by $\lambda_u/4$ leads to a photon helicity of $q=-1$, i.e. right circularly polarized light

when viewed from the point of view of the observer [77]. It should be noted that there exist two definitions of circular handedness, depending on if the electromagnetic wave is observed from the point of view of the source or the receiver. In this work the latter, also known as the optical convention, is used.

While the undulator already creates radiation with a resolving power of $E_{ph}/\Delta E_{ph} \sim N_u$ [75], with N_u the number of undulator periods ($N_u = 72$ for P04), this is insufficient for useful experiments. Therefore, two variable line-space gratings are installed as monochromators in the plane-mirror/plane-grating unit (PM/PG-U) of the beamline. They have respective spacings of 400 lines/mm and 1200 lines/mm, allowing to choose between higher photon flux and higher energy resolution. The variable line spacing serves to focus the monochromatized light onto an exit slit (EXSU) with an adjustable width up to 2000 μm , where a smaller slit size corresponds to a higher energy resolution as the energy spread of the photon beam gets turned into a spatial spreading of the different photon energies by the monochromator. Again, this leads to a trade-off between energy resolution and photon flux, since blocking parts of the beam naturally decreases the amount of photons arriving at the sample. For the measurements in this work, the 1200 lines/mm grating and an exit slit of 20 μm were chosen, resulting in an energy resolution of ~ 40 meV and a photon flux of roughly 3×10^{12} photons/s in the energy range of 500-730 eV relevant to this work.

To achieve a small focal spot size on the sample, the photon beam is focused by a pair of Kirkpatrick-Baez type mirrors (RMU), one to focus in the horizontal plane and one for the vertical plane. This leads to a nominal spot size of $10 \times 10 \mu\text{m}^2$.

Even though the ring current is being kept stable, as was mentioned before, there is still incentive to record an independent signal in parallel to the sample drain current and use it to normalize the sample current. This gets rid of potential fluctuations in the ring current, instabilities in the photon beam or different reflective behaviour of the optics in the observed energy range. To this end, the absorption signal I_0 of a fine Au mesh placed roughly 1 m before the sample is also measured (cf. Fig. 3.5). The advantage of this is, that Au has no significant absorption lines close to Fe or V (cf. Tab. 2.1) and that due to its noble nature, Au does not oxidize so that its absorption spectrum is very stable over time. To ensure that the stray magnetic field does not influence the I_0 measurements, the mesh was shielded.

Just as for the sample signal, the absorption of the Au mesh was measured as the total drain current. Even in the event that each photon produces one electron of measurable current, a photon flux of 10^{12} photons/s only leads to a drain current of $\sim 10^{-7}$ A and so both signals, sample and I_0 , were passed through a *FEMTO DDP*CA-300 transimpedance amplifier. This converted the small currents into a voltage between 0-10 V and it opened up the opportunity to apply a bias voltage between -10 V and 0 V to sample and mesh, to further counter unwanted radiation effects. The voltages were then fed into a volt-frequency-converter and synchronized to the master clock of PETRA III. This allowed to record both measured signals as well as beamline parameters like the undulator and monochromator energies or the undulator shift, at exactly the same time.

3.3.1. Spectra "On the fly"

In earlier absorption experiments, it was customary to vary the photon energy in previously defined energy steps and measure each energy point for a fixed time (cf. for example [58, 60]). However, considering a spectrum with an energy range of 40 eV, taken at 0.2 meV steps and with a counting time of 3 s per energy point leads to a total acquisition time of 10 minutes for a single spectrum. In regards to the limited amount of beamtime and also to minimize the influence of residual gases on the absorption it is advantageous to reduce the measurement time of each single spectrum.

During the beamtimes presented in this work, this was achieved by running the beamline in what became known as "On the fly mode" (OTF). The energy steps of the undulator and monochromator are replaced by a continuous motion at a fixed speed and the relevant data points to the absorption measurements are then obtained by reading out all the necessary devices (sample current, I_0 current, undulator energy, monochromator energy) at a fixed rate of 5 Hz (for the present samples).

For good measurements in this mode, it has to be ensured that the respective energy positions and speeds of the undulator and the monochromator are the same, since optimal photon flux on the sample is only achieved if the monochromator is set to the energy of the photons generated in the undulator. To this end, the undulator speed is adjusted whenever it should either lag behind the monochromator or rush ahead of it. This is achieved via a proportional-integral-derivative (PID) control loop, using the energy difference between the two devices as variable. Explanations on the exact functionality of a PID controller can be found in standard textbooks on control theory (e.g. [78]) and shall not be explained in more detail here. Suffice it to say that after an initial short adjustment period, this setup allows to keep the absolute energy difference between the two devices below 0.4 eV during the measurement process even for scan speeds of 1 eV/s (cf. Fig. 3.9). This almost optimal match of the device energies results in a high photon flux.

The first few seconds of Fig. 3.9 show that the system needs some time to settle in to a stable moving configuration, which is why the measurements were set up to start roughly 10 eV before the desired energy. Once the movement of the undulator and monochromator stabilized and the actual start of the desired energy range reached, a fast shutter in the beamline is opened, allowing the photons to impinge on the sample. This fast shutter serves to minimize the photon flux on the sample, in the case it might be radiation sensitive.

Starting from this energy point, both device energies are increasing linearly with a speed of 0.4 eV/s for the pure adsorbates. This value was chosen as for a scan speed of 0.4 eV/s and a delay of $(5 \text{ Hz})^{-1} = 0.2 \text{ s}$ between readouts of the devices, the average energy separation between measured points comes out to 80 meV, which is significantly lower than for previous measurements, even though it is higher than the theoretical energy resolution of the beamline at these energies. While lower scan speeds were possible, that option was not taken at the time as the OTF mode was still in its testing phase and it was rather opted to reduce the measurement time. With these parameters, a single spectrum with a nominal energy range of 40 eV is taken in roughly 200 s so that in the time it took for one spectrum in the old measurement mode, the OTF mode could produce three spectra at a better energy resolution.

To accommodate the higher number of scans needed for the two edges in the case of the alloy

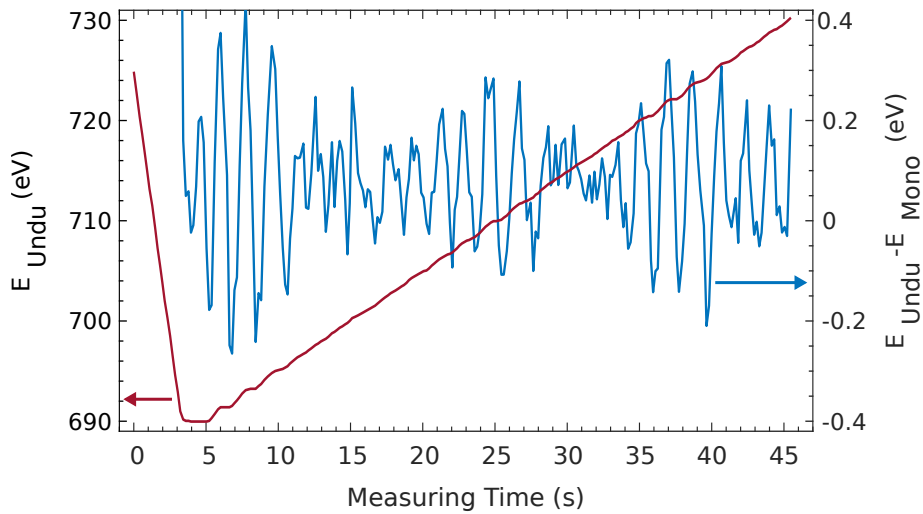


Fig. 3.9.: Temporal evolution of the undulator energy (red, left axis) and the difference between undulator and monochromator energies (blue, right axis), showcasing the success of the "On the fly mode" in keeping the moving speeds of both devices regular and keep their energies close. The scan speed was set to 1 eV/s.

samples, the scan speed was set to 1 eV/s.

Since these beamtimes, the OTF mode has been refined and it is now possible to have read-out frequencies of 50 Hz, meaning that even a scan speed of 1 eV/s produces spectra with an energy spacing of 20 meV, making full use of the energetic resolution of the beamline without sacrificing measurement speed.

3.4. Data Treatment

As mentioned earlier, the data analysis begins by normalizing the measured sample drain current by the simultaneously recorded drain of the I_0 mesh. This process gets rid of most of the unwanted instabilities in the beam, as can be seen when going from panel (a) to (b) in Fig. 3.10. The large fluctuations in the sample signal disappear and a clear falling trend of the intensity can be seen.

Given the low adsorbate coverage, this background can be seen as the absorption signal of the Cu substrate, which dominates the signal. To get rid of this influence, the supposedly flat region of the adsorbate signal is fitted with a linear function, reflecting the fact that the measurements take place far away from substrate absorption edges. This linear background is shown in Fig. 3.10 (b), together with the continuum step function (cf. 2.2.1).

With the background subtracted, cf. Fig. 3.10(c), the absorption spectrum is, in principle, ready. However, the low adsorbate coverages and external sources of noise, mechanical or electronic, make it necessary to average multiple spectra for each combination of helicity and magnetic field to increase statistics. This is especially true since the OTF measurement mode does not average over a certain time at each energy point, as was done before. An amount of 3-5 spectra was found to usually be sufficient for good statistics.

This averaging however requires all of the spectra to have a common energy axis, which the

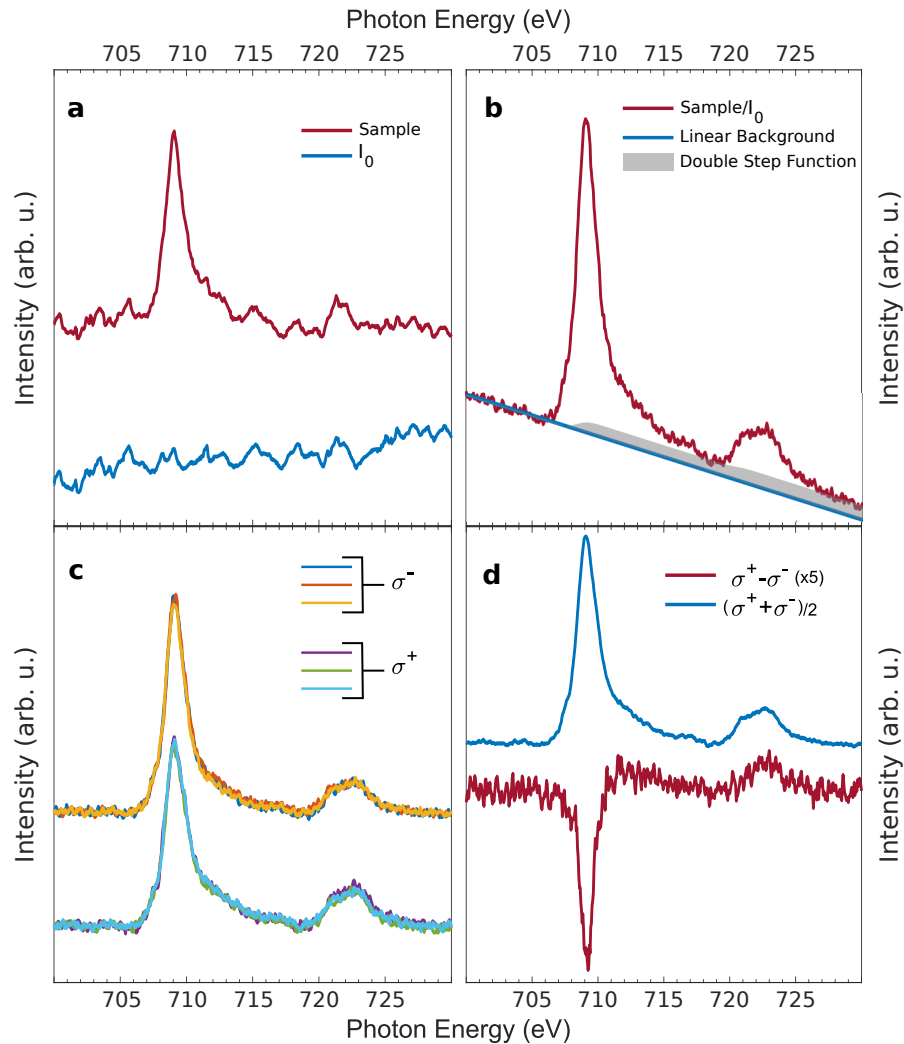


Fig. 3.10.: The different steps of the data treatment: (a) The raw signals of both the sample and the I_0 from the Au mesh. (b) The sample signal after normalization to the I_0 to get rid of beamline fluctuations. Also included are the linear background fitted to the pre- L_3 region of each sample and the double step function to model the excitation of $2p$ electrons into $4s$ states and the continuum. (c) Multiple background subtracted spectra with either the magnetic field parallel (σ^+) or antiparallel (σ^-) to the photon helicity. The two groups were vertically shifted for better visibility. (d) Final resulting XMCD and white line spectra. The XMCD signal has been multiplied by five and the two have been vertically offset for clarity.

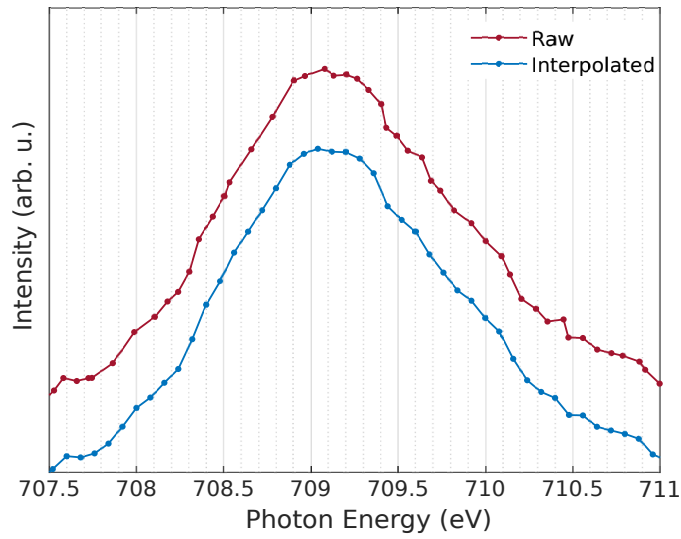


Fig. 3.11.: X-ray absorption intensity across an Fe L_3 edge, showcasing the effect of adjusting the raw data points at irregular intervals to a regular grid with fixed energy steps of the same mean size. The two spectra are vertically offset for better visibility.

somewhat statistic nature of the OTF measurement mode is not directly suited for. The exact timing of the readout processes varies slightly at each point, resulting in the energies of the data points having a statistical distribution. To counteract this, an energy grid with a spacing of 10 meV was defined and the energies and intensities of the individual data points were linearly interpolated to match the grid. This degree of oversampling was, for one, chosen so as to not introduce further errors into the spectra. Another reason for this dense energy grid was to make sure that the energetic distance of a raw data point to a "new" grid point was small enough to justify a linear interpolation. The number of data points was subsequently reduced again, to match the mean energy spacing of the raw spectra. The result of this process can be seen in Fig. 3.11, where a portion of a raw spectrum across the Fe L_3 edge and the corresponding interpolated spectrum are plotted. While it can be seen that the interpolation of the spectra does lead to a slight smoothing, this effect is in the order of less than 1 %, found by comparing the noise levels of the flat pre- L_3 region in both cases.

With the spectra now all adjusted to a common grid, they can be grouped into two categories depending on the relative direction of the external magnetic field and the photon helicity. The spectra where the sign of the undulator shift and the magnetic field are the same (opposite) are averaged to σ^+ (σ^-) and from Fig. 3.10(c) it can be seen, that spectra of the same group match very well within the noise level.

The last panel in Fig. 3.10 shows the results of taking the mean of the two averaged groups of spectra to obtain the isotropic X-ray absorption spectrum, the so-called white line, as well as the difference of the averaged groups to arrive at the XMCD spectrum. The negative XMCD signal at the L_3 edge matches the results for Ni by Chen *et al.* [28], which allows to determine the direction of the external magnetic field in the HFK. Chen *et al.* had found that subtracting the spectrum with antiparallel photon spin and majority electron spin from the spectrum with parallel photon spin and majority electron spin leads to such a negative L_3 intensity. This allows

to identify σ^+ as the case of parallel photon spin and majority electron spin. Together with the knowledge that a negative undulator shift of P04 leads to a positive photon spin [77], it can be established that a nominally positive magnetic field in the HFK is pointing "downstream", i.e. away from the undulator. This information can be useful to define absolute orientations of the magnetic moments later on.

4. Results and Discussion

4.1. Homometallic adsorbates

4.1.1. $\text{Fe}_{1,2,3}$

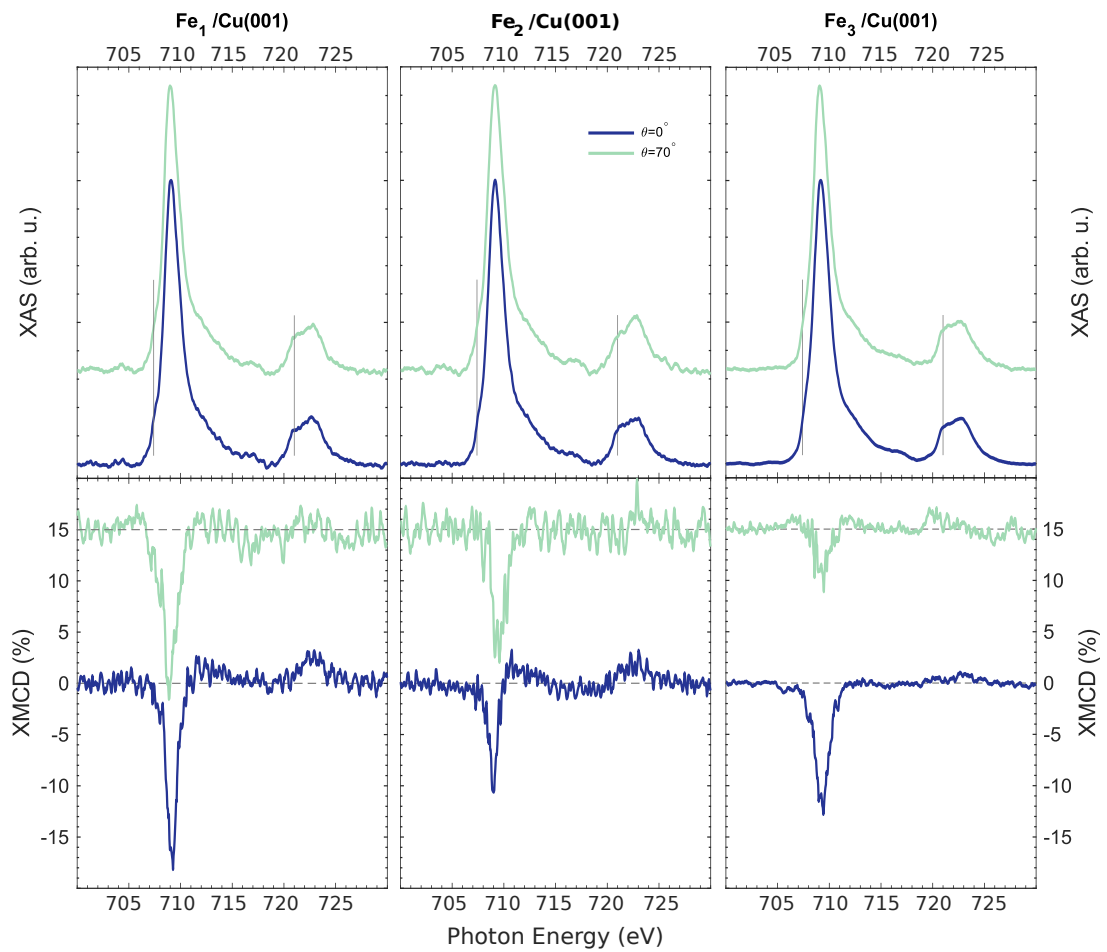


Fig. 4.1.: Background subtracted white line spectra (top row) for the Fe_1 adatom (left), the Fe_2 dimer (middle) and the Fe_3 trimer (right) for two incidence angles (see legend). The corresponding XMCD spectra in a ± 7 T field are shown in the bottom row. For better comparability, all spectra have been normalized to the L_3 peak of their respective white line and vertically offset for better clarity.

The white line spectra for each pure Fe adsorbate investigated in this work are shown in

the upper panels of Fig. 4.1, with the corresponding XMCD signals in the lower panels. The first thing of note are the spectral features at the lower energetic flanks of both L -edges (cf. vertical grey bars in the upper left panel). These so called multiplet features are the result of the Coulomb interaction of the $2p$ core hole and the $3d$ electrons and are typically found in atomic and atomic-like species [79–81]. In general, the adatom data matches the XAS of free Fe atoms [79] and free Fe_1^+ cations [80] really well. The L_3 peak position of 709.1 eV for the present adatom (cf. Tab. 4.1) does however lie higher than the values for free atoms (~ 707 eV) and the cations (~ 708 eV). This overall energetic shift has been observed for metallic adsorbates on metal surfaces before [66, 82, 83] and is explained as a result of valence electron delocalization in the initial state of the absorption process. The increased delocalization of the d -electrons brings with it a reduced Coulomb repulsion with the $2p$ core electrons, thereby increasing the effective nuclear charge experienced by these core electrons and subsequently their binding energy. This increased binding energy registers as higher excitation energy for the $2p$ electrons. This valence electron delocalization is likely also responsible for the general broadening of the spectrum with respect to the free species, as the delocalized electrons form bonds with the out-of-plane electronic states of the surface. While this implies that there is some hybridization with the surface, the clear visibility of the multiplet features shows that the degree of hybridization is still lower than it would be either in the bulk or a more strongly interacting surface, e.g. Fe (3 ML)/Cu(001) [66]. The fact that adsorbates couple weakly to Cu surface has also been reported for very small amounts of Fe which have evaporated onto a Cu(111) surface, where similar multiplet features can also be found [9].

A notable deviation of the results of $\text{Fe}_1/\text{Cu}(001)$ from the reported free atoms and cations is the apparent spin-orbit splitting of the $2p$ states, taken to be the energetic difference of the respective L_2 and L_3 maxima (cf. third column in Tab. 4.1). Both literature values for the free atom and cation match the value of 12.8 eV found for the bulk [84] quite well while for the present data, the value of 13.5 ± 0.25 eV is significantly higher. As Pacchioni *et al.* have found an apparent spin-orbit splitting matching the bulk value for Fe (0.007 ML)/Cu(111)[9], the interaction with the surface alone can not serve as an explanation for this observed divergence. It should also be noted that, taking the difference with respect to the lower energetic feature at the L_2 peak at around 720.7 eV, leads to an apparent spin-orbit splitting of 11.6 ± 0.25 eV, which puts the energetic position of the literature L_2 peak somewhat closer to the higher energetic peak found in this work. Recalling that energetic shifts are likely the result of differences in screening of the Coulomb interaction between either the core electrons and the nucleus or the core hole and the valence electrons, it appears that there are pronounced differences in screening for the $2p_{1/2}$ and the $2p_{3/2}$ electrons. A satisfactory explanation for this can however not be given at the moment.

The likeness of the Fe adatom's electronic structure to the references also reflects in the branching ratio (cf. first column in Tab. 4.1), which shows a very good agreement to the literature values of 0.85 for Fe_1^+ [80] and 0.83 for atomic Fe [79]. The fact that the experimental value found in this work matches the atomic value better could be a consequence of the charge deficiency in Fe_1^+ being neutralized by an electron from the substrate, leading to an effectively neutral Fe. All of these branching ratio values are also significantly higher than the 0.70 that Fink *et al.* and Scherz *et al.* found for bulk Fe [33, 85]. In general, the branching ratio can serve as an indicator of the spin state of the investigated element (cf. 2.2.3), which implies Fe to be

Adsorbate	B	$E(L_3)(eV)$	$\Delta E_{2p} (eV)$
Fe ₁	0.83 ± 0.04	709.1	13.5 ± 0.25
Fe ₂	0.82 ± 0.04	709.2	13.8 ± 0.25
Fe ₃	0.81 ± 0.04	709.2	13.5 ± 0.25

Tab. 4.1.: Branching ratios (B), L_3 peak position and energetic separation between the two L -edges (ΔE_{2p}) for the pure Fe adsorbates on Cu(001), extracted from the white line spectra at $\theta = 0^\circ$ in Fig. 4.1. All other incidence angles are omitted, as the values are isotropic.

in a high spin state for all the monomers in question. Furthermore it has been found that final state effects can greatly influence the branching ratio. Notably, the delocalization of d -electrons leads to increased electron mobility and hence better screening of the valence electron-core hole Coulomb interaction, distributing less spectral weight to the L_2 edge, resulting in generally reduced branching ratios in more than half filled d -shells [37, 38]. Thus, the branching ratio being high reinforces the conclusion that the adatom interacts weakly with the Cu surface. When it comes to adatoms, a similarly high branching ratio of 0.81 was found experimentally by Pacchioni *et al.* Cu(111) [9].

The XMCD signal at normal incidence shows a weak magnetic signature at the lower energetic feature of the L_3 peak, the appearance of which can reasonably be tied to the existence of a different electronic configuration in Fe (cf. 4.2). In addition to this, there is a small area of positive XMCD signal after the L_3 peak, a phenomenon that has been reported in previous experiments (e.g. [86–88]). Via the use of multipole moment analysis, van der Laan managed to relate this spectral feature to the spin polarization of the d -orbitals [89]. In contrast to this, the XMCD signal at $\theta = 70^\circ$ shows no such feature after the L_3 peak but rather has a small peak before the main L_3 peak, consistent with results from Pacchioni *et al.* for Fe (0.007 ML)/Cu(111) as well as for Fe (0.015 ML)/K, measured by Gambardella *et al.* [9, 81]. In both of these works, Fe was assumed to be in a predominantly d^7 configuration as well as being weakly bound to the respective substrate. While the current results could be explained with a high spin d^6 configuration and a very weak hybridization with the substrate, the alternative given by these literature results makes a compelling argument for Fe having 7 d -electrons.

While the magnitude of the Fe₁ XMCD seems to be almost the same for both measurement geometries, the increased width of the L_3 peak at $\theta = 70^\circ$ indicates that the magnetic moment is more strongly aligned in-plane. In contrast to this, Pacchioni *et al.* found an out-of-plane easy axis for Fe adatoms on Cu(111). Referring back to the crystal field split d -orbitals in Fig. 2.10, a reasonable root for this discrepancy lies in the C_{4v} symmetry of Cu(001). For a d^7 species, the lowest lying configurations are expected to be $(a_1)^2(e)^4(b_1)^1$, and $(a_1)^2(e)^3(b_1)^1(b_2)^1$, which would mean that the a_1 representation (corresponding to d_{z^2}) is always fully occupied, independent of spin state (cf. Tab. 2.3). For the high spin state, which is favored by the found branching ratio, the d_{xz} and d_{yz} orbitals of the e representation therefore remain as the lowest unoccupied, or partly occupied, states in case of a $2p \rightarrow 3d$ absorption process. Seeing as they are oriented out-of-plane, the motion of electrons in these orbitals gives rise to an in-plane orbital moment¹.

¹The concept of classical motion of the electrons in these orbitals is technically not correct but used here as a

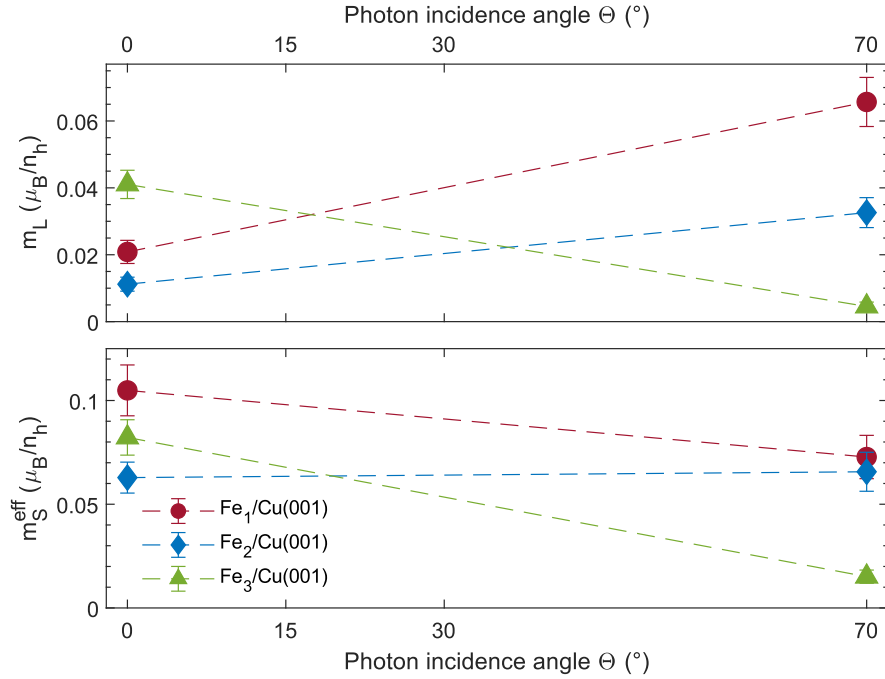


Fig. 4.2.: Orbital (upper panel) and effective spin (lower panel) magnetic moments, obtained via the sum rules, for the Fe adatom (red circle), the Fe dimer (blue diamond) and the Fe trimer (green triangle) as a function of the photon incidence angle θ .

Applying the sum rules, cf. (2.2.12), to the XMCD data of Fig. 4.1 and plotting the resulting orbital and effective spin moments as a function of the photon incidence angle leads to Fig. 4.2. Here, the in-plane orientation of the Fe₁ magnetic moment becomes much clearer, as the effective spin moment decreases for grazing incidence with the orbital moment simultaneously undergoing a significant increase. The increase of the orbital magnetic moment was already touched upon and for the spin moment it can be observed that the d_{xy} and $d_{x^2-y^2}$ orbitals, lying in-plane, are both half filled for the high spin configuration. This results in a strong difference between spin-up and spin-down occupation and a strong spin moment in normal incidence. For the out-of-plane orbitals, this difference in occupation is much less pronounced, since at least one of them is fully occupied, leading to a lower measured spin moment when investigating in grazing incidence.

While being able to gauge the evolution of m_L and m_S^{eff} separately is helpful, it should be kept in mind that, due to the current base temperature of the measurement setup, it is unlikely that the magnetic moments are in saturation and it is therefore not possible to make statements about the absolute moments. This is exacerbated by the fact that the number of d -holes (n_h) can not be obtained from the current measurements. A much more robust way to make comparisons between experiments independently of n_h , magnetic saturation or applied magnetic field, is the ratio of orbital to spin magnetic moment m_L/m_S^{eff} (cf. 2.2.1). To this end, the ratios in question for the present data were compiled in Tab. 4.2, where in addition to this, there is a (non-exhaustive) listing of ratios gathered from literature for different Fe containing systems.

For the present adatom Fe₁/Cu(001), this ratio further solidifies the in-plane magnetic moment orientation, with the ratio being more than four times the one for out-of-plane measurements.

In comparing different substrates and the resulting m_L/m_S^{eff} ratios of Fe, the general trend can be established that the ratio decreases for increasing electronic density at the Fermi edge of the substrate, as has been observed and investigated before in the works of Claude [90]. For a given substrate, comparison between m_L/m_S^{eff} from different sources can however be problematic. In the case of dilute Fe on Cu(001), there is large discrepancy between the ratios values of 0.12 found by Gambardella *et al.* [91], 0.25 ± 0.05 reported by Claude [90] and the 0.36 ± 0.04 Lehnert found for normal incidence [92], where nonetheless they all agree on an out-of-plane magnetic orientation. A possible explanation for this could lie in the fact that the respective Fe coverages of the three experiments are not consistent. Given the statistical nature of the evaporation process, these discrepancies could lead to the formation of aggregates and subsequent change in the magnetic properties. However, in the case of Fe on Cu₂N, the reported coverages are the same for Lehnert [92] and Etzkorn *et al.* [93], which would point towards the statistical distribution of adsorbates being similar, and yet there is still a difference in their reported values. Scanning tunneling microscopic results by Balashov *et al.* have revealed significant differences in both the magnetic moments and the anisotropy of Fe adatoms at different adsorption sites on a Pt(111) surface [94]. It can be argued that the differences in reported m_L/m_S^{eff} ratios for Fe on Cu₂N arise from the different adsorption points on the Cu₂N surface. A similar argument might be made for the data of Fe/Cu(001) and while the agreement between the present measurements and literature is lackluster, there are parameters that could not have been controlled in all of the experiments so far and would warrant a closer inspection in the future.

In comparison to these previous results, it also becomes apparent that the m_L/m_S^{eff} ratio is not just large, but exceptionally large. Only the measurements on Fe (0.015 ML)/K give a m_L/m_S^{eff} ratio that is larger than for the present adatom [81]. Recalling that in that study, good agreement between experiment and simulated spectra for a d⁷ configuration was found, and furthermore taking into account the ratio of 1 gained from the Hund's rules for a theoretical d⁷ atom, there is ample grounds to assign a mostly d⁷ configuration to the Fe adatom.

Another factor enhancing the orbital magnetic moment could be degeneracy of the out-of-plane e (d_{xz}, d_{yz}) orbitals. In an intuitive classical picture, orbital magnetic moments arise from the spatial motion of electrons (cf. [31]). For two degenerate orbitals, the electron has the possibility to hop from one orbital into the other without energy loss, given the second orbital does not already contain an electron of the same spin. This hopping brings with itself further orbital motion and thus a contribution to the orbital moment.

By adding a second Fe atom and arriving at Fe₂/Cu(001), the changes in the XAS are subtle but nonetheless visible (cf. middle column in Fig. 4.1). Firstly, the spectrum as a whole broadens, with the features at the lower energetic flanks of both peaks becoming less pronounced, while remaining discernable. This recalls the trend in the work of Hirsch *et al.*, where the spectra become increasingly bulk like as a function of increased cationic cluster size [80]. In the same manner as the broadening of the Fe₁ XAS with respect to the free cation could be traced back to increased valence electron delocalization by interaction with the surface, the broadening when going from Fe₁ to Fe₂ can be interpreted a result of increased hybridization of the d -electrons across the two atoms. This also reflects in the L_3 peak position (cf. Tab. 4.1) shifting upwards by about 0.1 eV with respect to the adatom due to the decreased screening of the

System	m_L/m_S	Source
Fe ₁ /Cu(001)	0.20 ± 0.04 (0°)	this work
	0.90 ± 0.14 (70°)	
Fe ₂ /Cu(001)	0.18 ± 0.04 (0°)	
	0.50 ± 0.09 (70°)	
Fe ₃ /Cu(001)	0.50 ± 0.05 (0°)	
	0.30 ± 0.11 (70°)	
Fe (0.025 ML)/Cu(001)	0.12 (0°)	[91]
	0.11 (70°)	
Fe (0.016 ML)/Cu(001)	0.25 ± 0.05	[90]
Fe (0.015 ML)/Cu(001)	0.36 ± 0.04 (0°)	[92]
	0.29 ± 0.03 (70°)	
d ⁶ atom ground state	0.50	Hund's rules
d ⁷ atom ground state	1.00	Hund's rules
Fe (bulk)	0.043	[86]
Fe (0.020 ML)/Pd(111)	0.12 ± 0.05	[95]
Fe (0.010 ML)/Rh(111)	0.15 ± 0.05	[95]
Fe ₁ /Ni/Cu(001)	0.17 ± 0.03	[87]
Fe (0.010 ML)/Pt(111)	0.18 ± 0.05	[92]
Fe (0.030 ML)/Li	0.20 ± 0.03	[90]
Fe (0.030 ML)/Na	0.31 ± 0.03	[90]
Fe (0.145 ML)/Cu(111)	0.16 ± 0.02	[9]
Fe (0.066 ML)/Cu(111)	0.21 ± 0.03	[9]
Fe (0.007 ML)/Cu(111)	0.30 ± 0.07 (0°)	[9]
	0.23 ± 0.09 (60°)	
Fe (0.030 ML)/Al ₂ O ₃ /Ni ₃ Al	0.53 ± 0.09 (0°)	[96]
	0.30 ± 0.07 (70°)	
Fe (0.020 ML)/Cu ₂ N/Cu(001)	0.24 ± 0.02 (0°)	[92]
	0.04 ± 0.02 (70°)	
Fe (0.020 ML)/Cu ₂ N/Cu(001)	0.33 ± 0.05 (0°)	[93]
	0.15 ± 0.06 (70°)	
Fe (0.010 ML)/Au(111)	0.35	[88]
Fe (0.015 ML)/K	0.95 ± 0.05	[81]

Tab. 4.2.: m_L/m_S^{eff} ratio extracted from the present data on pure Fe adsorbates compared to a range of reported values for Fe containing species from the literature. If there is only one value listed, that refers to the normal incidence measurement.

Coulomb interaction between core and $2p$ electrons. While this increase in excitation energy is smaller than the shift of energy in the adatom with respect to the free atomic species, it is nonetheless more than an artifact given the energy step width of 80 meV in these measurements (cf. 3.3.1).

The change both in the XAS shape and in the deduced branching ratio (cf. Tab. 4.1) is small, with the decrease of the branching ratio lying completely within the error bounds of the data. This small change is particularly interesting considering that Hirsch *et al.* found a sizable drop in the branching ratio from 0.85 to 0.80 in going from Fe_1^+ to Fe_2^+ . However, the decrease in that work is too small to conclusively tie it to a switch from a high spin to a low spin state. It is more likely that, just as was the case for the adatom in contrast to the bulk, the increased delocalization of d -electrons reduces the overlap with the $2p$ core hole and leads to a decrease of the branching ratio. Considering the change from a free cation to a dimer, the change in delocalization is significant, intuitively doubling the spatial extent of the orbitals and thereby strongly affecting the branching ratio. In contrast to this, $\text{Fe}_1/\text{Cu}(001)$ is already coordinated with four atoms on the surface layer of Cu and the addition of a second Fe atom then leads to an increase in coordination number to five, which is much less than the factor of two in the free cluster. An analogous, slight, decrease in branching ratio was found for Fe adsorbates on Cu(111) by Pacchioni *et al.*, more explicitly from 0.81 at a mean cluster size of 1.07 to a value of 0.80 at a mean cluster size of 1.82.

Furthermore, by examining the apparent spin-orbit splitting through the ΔE_{2p} value for $\text{Fe}_2/\text{Cu}(001)$ in Tab. 4.1, one can see that the value increases slightly, even if within the error bounds. While a larger spin-orbit splitting is expected to lead to the branching ratio approaching the statistical value of $2/3$ [35], it can be debated whether this is the mechanism at play here. Rather, it seems like a statistical fluctuation, given the return to the adatom's apparent spin-orbit splitting value for Fe_3 . This behaviour matches the trend in the free cationic clusters, where the apparent spin-orbit splitting does fluctuate but mostly stays the same regardless of cluster size. Based on this observation, Hirsch *et al.* have stated that most likely the change in branching ratio is not due to spin-orbit effects, but rather the screening of the Coulomb interaction between the $3d$ orbitals and $2p$ core hole that was already brought up.

Turning to the XMCD signals for Fe_2 , the first observation is that the overall magnitude of the signal decreases compared to the adatom. As all other parameters were kept fixed between the measurements of different adsorbates, this translates to a decrease in the magnetic moment. Such a quenching of the magnetic moment has been calculated in the work of Stepanyuk *et al.*, where the magnetic moment of $\text{Fe}_2/\text{Cu}(001)$ lies just slightly below $3.0 \mu_B$ compared to the adatom's value of just above $3.1 \mu_B$ [97]. In the same vein, Lazarovits *et al.* have calculated a total magnetic moment of $3.92 \mu_B$ for $\text{Fe}_1/\text{Cu}(001)$ and $3.39 \mu_B$ per atom for $\text{Fe}_2/\text{Cu}(001)$ [98]. Experimentally, Fe adsorbates on Cu(111) were found to have decreasing magnetic moments with increasing coverage, and hence mean cluster size [9]. More specifically, the total magnetic moment drops from $2.86 \mu_B$ to $2.60 \mu_B$ for the respective mean cluster sizes of 1.07 and 1.82. The overall shape of the Fe_2 XMCD at normal incidence is similar to the one found for Fe_1 , including the region of positive sign just after the L_3 peak. This is in contrast to the results of Zamudio-Bayer *et al.*, where the XMCD for free Fe_2^+ clusters shows a second dip just after the main L_3 feature [99]. While it is not exactly known, which orbital is responsible for the spectral feature at this energy, it appears as if the interaction with the Cu surface has a profound impact

on its magnetic properties.

In comparison to the normal incidence, the Fe₂ XMCD is stronger for $\theta = 70^\circ$, implying that the magnetic moment lies preferably in-plane. Furthermore, the small peak just before the main L_3 feature is not visible anymore, which points to both less localized Fe d -orbitals and a possible loss of the mainly d^7 type configuration. Hübner and Sauer have performed complete active space self-consistent field (CASSCF) calculations for the free Fe dimer and found an $^9\Sigma_g^-$ ground state with a bond length of 2.187 Å and 13 d -electrons [100]. For a dimer adsorbed on a surface, this bond will stretch further to accommodate the lattice parameters of said surface. Considering only hollow adsorption sites and ignoring surface relaxation, the interatomic distances in the clusters must conform to $a_{Cu}/\sqrt{2} = 2.56$ Å and $a_{Cu} = 3.61$ Å for nearest and second nearest neighbours respectively, with a_{Cu} the lattice parameter of fcc Cu (e.g. [101]). This bond stretching will only serve to favor this high spin state further, as GGA+U calculations by Rollmann *et al.* have shown [102]. On average, each Fe atom in this spin state then has a $d^{6.5}$ configuration, which supports the present claim of decreasing d -occupancy.

From the evaluated magnetic moments shown in Fig. 4.2, it can be seen that both magnetic moments increase with the photon incidence angle, although this effect is less pronounced for the spin magnetic moment. This manifests as an increased m_L/m_S^{eff} ratio and shows that, just as for the adatom, the dimer's spin and orbital magnetic moment couple differently to the substrate. Overall, the m_L/m_S^{eff} ratio is reduced compared to the Fe₁/Cu(001) case, which points to the loss of orbital momentum as result of lowering the local symmetry of each Fe atom from C_{4v} in the adatom to C_{2v} (at best) in the dimer. Consulting the character tables for the two groups in question (e.g. [103]), shows that the degenerate e representation of C_{4v} splits up into an b_1 and a b_2 representation in C_{2v} , each of them non-degenerate. This suppresses the hopping motion of the electrons that was presented as responsible for the enhanced orbital magnetic in the intuitive picture for the adatom. A Similar decrease in orbital moment was reported for the statistical Fe clusters on Cu(111) [9]. Comparing also to $m_L/m_S^{eff} = 0.57 \pm 0.04$ for Fe₂⁺ [99], one sees that the orbital magnetic moment becomes partially quenched upon deposition of the dimer, related once again to the symmetry reduction and subsequent splitting of all of the degenerate orbitals of $D_{\infty h}$ in the free dimer to non-degenerate orbitals of C_{2v} on the surface.

From the rightmost pair of spectra in Fig. 4.1, one can see that the trend of the Fe adsorbates' white line spectra to become less atomic-like with increasing cluster size continues for Fe₃. While the multiplet features at the L_3 edge are barely noticeable in the XAS the double structure is still clear for the L_2 peak. Again, the change is nowhere near as drastic as in the data from Hirsch *et al.*, where the XAS of Fe₃⁺ is already close to the bulk. For the statistical clusters of mean size 3.25 on Cu(111), investigated by Pacchioni *et al.*, a similar broadening, more akin to the evolution of the free clusters of [80] than the present work, can be observed [9].

While the energetic position of the L_3 peak remains constant in going from dimer to trimer, the determined branching ratio decreases slightly in comparison to the smaller adsorbates. As the energetic separation of the L -edges however matches the adatom's value again, this can not be the reason for the branching ratio's decrease (cf. Tab. 4.1). As previously mentioned, this behaviour of the apparent spin-orbit splitting is to be expected and matches with the trend in the literature values for free Fe cations [80]. However, the same can not be said for the branching ratio. Rather, Hirsch *et al.* have found the branching ratio to be increasing from 0.80 to roughly 0.82 from Fe₂ to Fe₃. Contrary to this, Pacchioni *et al.* have found the branching

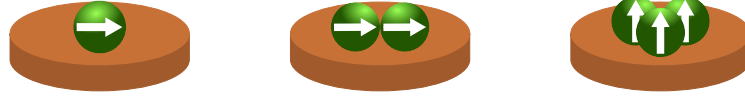


Fig. 4.3.: Proposed magnetic easy axes of the pure Fe adsorbates. From left to right, the number of Fe atoms in the clusters increases from one to three. These depictions are meant as schematics and should not be taken as quantitative.

ratio to decrease to 0.76 in going from the statistical dimer to the statistical trimer. While the trend in the free clusters goes against the established explanation of increased dynamic electron-core hole screening lowering the branching ratio, this is most likely the root of the observed lowering of the branching ratios in this work and the work by Pacchioni *et al.*. This also shows that the initial state effect of reduced static screening between the core and the $2p$ electrons and the final state effect of increased dynamic screening of the Coulomb interaction between valence electrons and core hole have an opposing effect on the excitation energy of the $2p \rightarrow 3d$ transitions, evidenced by the combined decreased branching ratio with the constant peak position.

From the panel on the lower right in Fig. 4.1 it can be seen that the strength of the normal incidence Fe_3 XMCD is larger than for the dimer, reinforcing the notion that changes in the cluster properties are not a monotonic function of cluster size. For the statistically evaporated trimer, mean cluster size of 3.25 on Cu(111), Pacchioni *et al.* have on the other hand found a lowering of the magnetic moment to $2.44 \mu_B$ compared to the dimer [9]. The present evolution of the total magnetic moment matches the results of Lazarovits *et al.* to some degree, where the magnetic moment for $\text{Fe}_3/\text{Cu}(001)$ was found to be around $3.40 \mu_B$ [98]. In contrast to this, Stepanyuk *et al.* have found the trimer's magnetic moment on Cu(001) to be smaller than the one for the dimer [97]. It should however be noted that for both these results, a linear trimer was assumed, which does not necessarily reflect the minimum energy geometry on the surface. Density functional calculations on free Fe trimers have on the contrary shown that the most stable configuration is an isocles triangle with sidelengths 2.313 \AA and 2.176 \AA [104]. Considering once again the bond lengths and angles imposed by the Cu surface, this triangle can of course not be realized. The right isocles triangle with side length $a_{\text{Cu}}/\sqrt{2} = 2.56 \text{ \AA}$ and hypotenuse $a_{\text{Cu}} = 3.61 \text{ \AA}$ is however a possibility, and it is not unreasonable that its energy is lower than that of the linear chain. The significantly smaller XMCD signal at $\theta = 70^\circ$ implies a clear out-of-plane trimer magnetization. This finding of an out-of-plane magnetization is reinforced by examining the results of the sum rules, where it can be seen that both the orbital and the spin magnetic moment decrease strongly for the grazing incidence. In addition to this, the m_L/m_S^{eff} is 0.50 ± 0.05 for $\theta = 0^\circ$, which makes it twice as large as the one for $\theta = 70^\circ$ and puts it at roughly the value of the Hund's rule ground state for the atom (cf. Tab. 4.2). Just as before for the smaller adsorbates, this signifies a weak interaction between the cluster and the surface. Considering the aforementioned trade-off between cluster-surface hybridization and intracluster hybridization leading to the branching ratio staying roughly fixed, it can be stated that there are delocalized d -orbitals connecting the three constituents of the trimer and that for a triangular cluster lying parallel to the substrate surface this entails more orbital motion in the substrate plane, leading to a larger out-of-plane orbital magnetic moment.

The clear change from in-plane to out-of-plane magnetization in going from the deposited dimer to the Fe trimer (cf. Fig. 4.3) can be viewed as continuation of the trend of magnetization reorientation in Fe thin films on Cu(001) as a function of the number of monolayers [105, 106]. Below 4 ML, Fe grows pseudomorphic to the fcc surface, with slight distortions. This is accompanied by a high spin, out-of-plane orientation of the magnetic moments. Above a thickness of 10 ML, the Fe film assumes its native bcc structure and shows a low spin in-plane magnetization. In the region between these two, the structure and magnetic properties of the film depend on the sample temperature. For low temperatures, the structure remains the same distorted fcc structures imposed by the surface, with the low spin magnetization now oriented in-plane. At higher temperatures, the Fe film assumes an fcc structure almost perfectly matching that of γ -Fe, except for the top layer, which shows a bcc reconstruction. This top layer is ferromagnetic and out-of-plane while the rest of the layers are antiferromagnetic [107].

While at the atomic level investigated in this work it is questionable to talk about bcc or fcc structures, the fact that the Cu surface constrains the structure of the adsorbates still holds, as was discussed for both the dimer and the trimer. For the adatom, the in-plane orientation of the magnetic moment appears to be a direct result of the splitting of the d -states via the crystal field of the fourfold symmetric Cu(001) surface. Starting from the dimer, the interatomic distances in the clusters induced by the Cu surface weaken this symmetry and in its place comes an interatomic effect tending towards out-of-plane easy axes. Already at the trimer, this trend is very pronounced and, without measurements on larger Fe clusters, it appears as if this continues on for a wide range of Fe coverages. In contrast to this, there is no changing of the easy axis orientation in the case of Fe adsorbates on Cu(111) [9], reinforcing the idea that this is an effect arising from the surface geometry.

4.1.2. $V_{1,2,3}$

Fig. 4.4 shows the XAS and XMCD spectra for the V adatom, dimer and trimer on Cu(001) taken in the course of this work. Compared to the spectra of free V_1 and V_1^+ [79, 80], the present data on the V adatom shows a reduced number of discernable peaks, due to the broadening of the spectrum. Still, there are pronounced multiplet features at the lower energetic flanks of both L -edges of the V adatom (cf. vertical bars in the upper left panel of Fig. 4.4), which set this spectrum aside from e.g. the spectrum of bulk V [33, 85]. The spectral broadening, together with the general energetic shift of the spectrum with respect to the free V species (compare Tab. 4.3 with 514 eV for V^+ and 516 eV for atomic V), are a result of the hybridization of the d -electrons of V with the sp band of the Cu(001) surface just as was the case for the Fe adsorbates. On the other hand, peak energies gained from dilute V atoms embedded in a Cu crystal by Huttel *et al.* match the ones for V_1 /Cu(001) almost perfectly, bolstering the explanation of the interaction with the Cu crystal as the source of the energetic shift.

From the V spectra it becomes evident that the absorption does not go to zero between the L -edges due to their small spin-orbit splitting, as has been shown for early $3d$ metals [33, 108]. It therefore becomes challenging to evaluate quantities like the branching ratio or the spin magnetic moment, as those depend on separating the $2p_{1/2} \rightarrow 3d$ from the $2p_{3/2} \rightarrow 3d$ absorption processes (cf. (2.2.17) and (2.2.12)). Seeing as the orbital sum rule does only depend on the integrals over both L -edges, this problem does not arise in that case. The lowest point of the

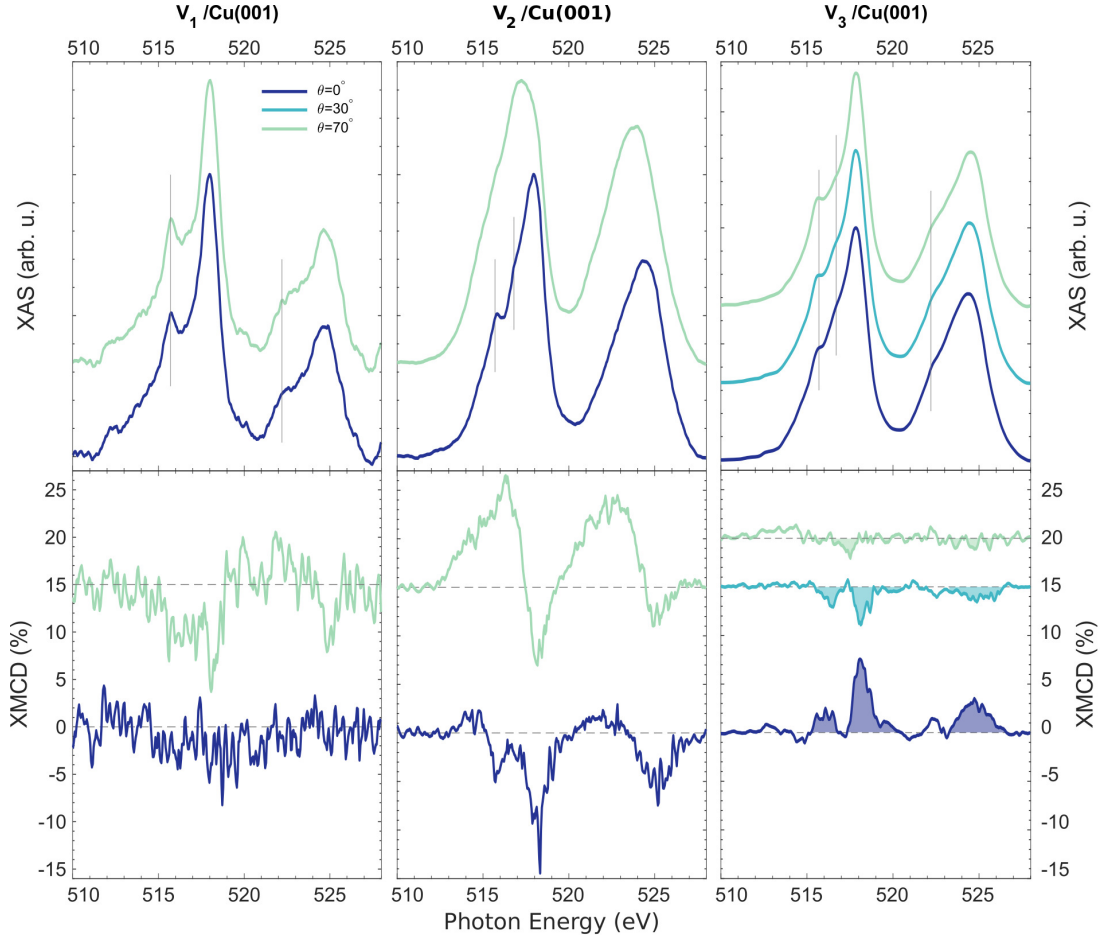


Fig. 4.4.: Background subtracted white line spectra (top row) for the V_1 adatom (left), the V_2 dimer (middle) and the V_3 trimer (right) for up to three incidence angles (see legend). The corresponding XMCD spectra in a ± 7 T field are shown in the bottom row. For better comparability, all spectra have been normalized to the L_3 peak of their respective white line and vertically offset for better clarity.

spectrum between the L -edges was chosen as the separation point in calculating the branching ratio. As the separation procedure is consistent for all V containing adsorbates in this work, the branching ratio shall nonetheless be given, especially considering that the corresponding value is less sensitive to small changes in the exact separation. The spin sum rule will however not be applied here, as the effect of the somewhat arbitrary edge separation can be more dramatic in this case.

Tab. 4.3 summarizes the results of the branching ratio calculation for the V_n adsorbates, together with the L_3 peak positions and the apparent $2p$ spin-orbit splitting, i.e. the energetic separation of the L -edges. It is interesting to see that, just as for the Fe adatom, the branching ratio matches the value of 0.66 for the free atom [79] better than it does the value of almost 0.75 for the free cationic monomer [80]. This points towards the cation gaining an electron when coming into contact with the surface, restoring a mostly atomic configuration. While the value of 0.67 ± 0.03 matches the theoretical $2/3$ ratio expected in the absence of both spin-orbit

Adsorbate	B	E(L_3)	ΔE_{2p} (eV)
V ₁	0.67 ± 0.03	518.0	6.6 ± 0.25
V ₂	0.54 ± 0.03	517.9	6.4 ± 0.25
V ₃	0.55 ± 0.03	517.8	6.6 ± 0.25

Tab. 4.3.: Branching ratios (B), L_3 peak position and energetic separation between the two L -edges (ΔE_{2p}) for the pure V adsorbates on Cu(001), extracted from the white line spectra at $\theta = 0^\circ$ in Fig. 4.4. All other incidence angles are omitted, as the values are isotropic.

interaction and electrostatic interactions in the d -states almost perfectly, this is most likely only the result of two competing effects canceling out. From the work of Thole *et al.* on branching ratios, it can be seen that the average branching ratio of a d^n configuration changes with the scaling of the atomic Slater integrals (cf. Fig. 2.8). For $n \leq 3$ in particular, the electrostatic interactions always shift the average branching ratio of a given many-electron term down and away from $2/3$. For each LS , the Hund's rules ground state term then (usually) has a higher than average branching ratio, which in the case of e.g. V can restore the value so it looks statistical again. Furthermore, there is a stark discrepancy to both the branching ratio of the bulk (0.51 [33, 85]) and 0.56 found by Huttel *et al.*. It is likely that this is due to the stronger delocalization of the V d -electrons with either the neighbouring V atoms in the bulk or the higher number of Cu atoms in the embedding matrix. It was shown that the branching ratio lowering effect of the dynamic screening of the valence-electron-core-hole interaction is more pronounced in the case of low d -counts and can thus explain the observed values in these delocalized systems [37, 38]. There is moreover the possibility of the d -count becoming lower in the two literature cases, which would in turn lower the branching ratio of the high spin state. While, in general, these assignments should be made cautiously and theoretical calculations are better suited to make comments on the electronic states, it is nonetheless possible to exclude certain possibilities. For example, the relatively high branching ratio of the adatom does support neither a low spin state for d^2 nor d^3 .

The apparent spin-orbit splitting was calculated from the maximum values of each peak, which is however a somewhat arbitrary assignment. For example in the work of Huttel *et al.*, the L_2 is too broad to make a definitive statement about the peak energy. The 6.8 eV energy difference found for the bulk [85] does however match the present value of 6.6 ± 0.25 very well (cf. right column of Tab. 4.3), which hints at the apparent spin-orbit splitting remaining mostly constant over large size ranges, as has been shown in the work of Hirsch *et al.* [80].

From the weak, but noticeable, XMCD signal at normal incidence, the existence of a magnetic moment of V₁/Cu(001) can be deduced, which is in accordance with the results by Huttel *et al.* that found a similar magnetic moment for the V atoms dispersed in a Cu matrix [109]. Additionally, theoretical investigations of V adatoms on a Cu(001) surface yielded magnetic moments of $3 \mu_B$ [97] and $3.03 \mu_B$ [110]. In contrast to this, Moore *et al.* could not find evidence for magnetic ordering in V thin films (2-5 ML) on Cu(001) [111]. The appearance of magnetism in small V systems is often a result of size reduction [112, 113], meaning that not only are the present findings supported by theoretical results, they also fit the expected trend

of V being magnetic in small systems. Due to the relatively weak XMCD signal a comparison to literature spectra (e.g. for V-Fe multilayers [108]) can not be performed conclusively, since especially the characteristic asymmetric lineshape is not present in the normal incidence case.

The stark height difference of the XMCD signals as a function of photon incidence angle leads to conclude that the magnetic moment of the V adatom has a preferred in-plane orientation. This can readily be explained making use of the crystal field model from 2.3.1. For the d^2 case, the high spin configuration is $(a_1)^1(e)^1$, so that $2p$ electrons would preferably get excited into either the d_{z^2} orbital or the degenerate d_{xz} and d_{yz} orbitals. Although the out-of-plane oriented d_{z^2} holds no orbital momentum, entailing that excitation into this orbital would not lead to an orbital magnetic moment, it's difference in spin occupancy together with the charge anisotropy would lead to an increased in-plane spin moment and a decreased out-of-plane spin moment. This effect is added onto the in-plane orbital and spin moments generated by the out-of-plane orbital of the e representation and its charge anisotropy. This would result in a preferred in-plane magnetic moment. A parallel argument can be made for the high spin d^3 configuration $(a_1)^1(e)^2$, where each of the degenerate orbitals of the e representation are singly occupied, possibly resulting in an even higher in-plane orbital moment. Thus, for both of these configurations one would expect a preferred in-plane magnetic moment.

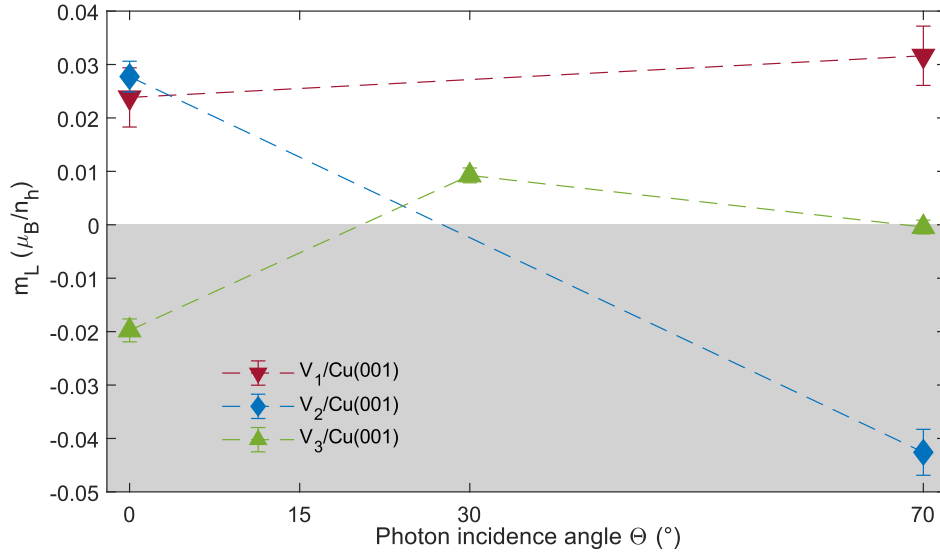


Fig. 4.5.: Orbital magnetic moments, obtained via the sum rules, for the V adatom (red circle), the V dimer (blue diamond) and the V trimer (green triangle) as a function of the photon incidence angle θ .

This is corroborated by Fig. 4.5, which shows an increased orbital magnetic moment for the grazing incidence case. Furthermore, this shows a considerable contribution of the orbital magnetic moment to the overall magnetic signal. Faced with the aforementioned difficulties in the application of the spin sum rule, the corresponding spin moment is not evaluated from the XMCD spectra.

Turning now to the adsorbed dimer (middle column of panels in Fig. 4.4), the first thing that becomes noticeable is the general broadening of the white line spectrum at $\theta = 0^\circ$. Just

as for Fe, addition of a second atom to the cluster leads to the creation of molecular orbitals spread out across the whole cluster. This delocalizes the d electrons and thereby decreases the visibility of the multiplet features. A similar trend was present in the spectra of Hirsch *et al.* when going from V_1^+ to V_2^+ [80]. A peculiar observation is that, overall, the shape of free V_2^+ matches the shape of $V_1/\text{Cu}(001)$ better than V_1^+ does. This can be attributed to the adatom being more strongly delocalized than the free cationic monomer, due to interaction with the surface. Afterwards, the addition of a second V atom to the adsorbed cluster does increase the delocalization, but not in as strong a way as it does for the free cluster. This can be viewed as the intracluster hybridization in V_2 being stronger than between the V atoms and the surface. The small shift of the L_3 peak to lower energies (cf. Tab. 4.3) can again be explained by the increased delocalization of the $3d$ electrons. The direction of the peak energy shift is however contrary to both the Fe adsorbates as well as the trend in the free clusters [80]. This can probably be attributed to the dynamic screening effect of delocalized valence electrons, favoring lower binding energies of the $2p$ electrons and lower branching ratios, being stronger in elements with less-than-half filled d -shells such as V. This effect than outweighs the static effect of the delocalized valence electrons in the initial state, which would increase the excitation energy and has been found to increase in importance for higher d -count [37, 38].

Another difference in the spectra of the free and the adsorbed dimer, is the feature at ~ 517 eV (marked with a grey bar in Fig. 4.4). It lies between the multiplet feature that was already present in the XAS for the adatom and the maximum of the L_3 peak and does not appear in either the spectrum of the adatom or the free dimer. Following the experiments from Spain *et al.* [114] and James *et al.* [115] the ground states of free V_2 and V_2^+ were determined to be $^3\Sigma_g^-$ and $^4\Sigma_g^-$ respectively. This was confirmed by density functional theory calculations by Gutsev *et al.* [116]. However, the bond length of 1.77 \AA (1.73 \AA) for the free neutral (cationic) dimer is not commensurable with the nearest neighbour distance of 2.56 \AA on the Cu(001) surface [114, 117], so that the interatomic bond has to stretch during the adsorption process. Calculations by Weber *et al.* have shown that above a bond distance of 2.20 \AA , the dimer ground state is no longer a triplet but has a spin multiplicity of 7 (i.e. $S=3$), translating to 7 d -electrons of majority spin and 1 electron of minority spin [110]. Even without taking the possible hybridization of the d -electrons of the dimer with the Cu surface into account, the mere effect of stretching the dimer bond is responsible for some of the molecular orbitals becoming singly occupied, thus opening up the possibility to excite $2p$ electrons into these orbitals, resulting in additional contributions to the spectrum like the one observed here.

The branching ratio of 0.54 ± 0.03 for the present dimer presents a significant reduction with respect to the value of both the free atom (0.66) and the adatom (0.67). While this mirrors the branching ratio's evolution in the free clusters qualitatively, there is again no quantitative agreement [80]. Yet there is very good agreement with the branching ratio of V atoms in a Cu matrix (0.56) that Huttel *et al.* reported [109]. A possible lowering of the $2p$ spin-orbit interaction can be ruled out as the source of the lowering of the branching ratio, seeing that if one considers the energetic separation of the L -edges (cf. Tab. 4.3), the value for $V_2/\text{Cu}(001)$ drops slightly, which according to Thole *et al.* should actually lead to an increase in branching ratio [35]. Rather, this lowering can reasonably be traced to the dynamic screening effect of the delocalized $3d$ electrons, just like for the lowered excitation energy. While in the work of Huttel *et al.* the delocalization was a result of the large number of Cu neighbours, in this case it

is due to the formation of molecular orbitals in the dimer itself. This reinforces the notion that the intracluster hybridization is greater than the hybridization with the substrate.

An even more striking observation in the XAS spectra of the adsorbed dimer is the strong difference between the spectrum at normal incidence and the one at grazing incidence. The peaks are strongly broadened and the lower energetic multiplet feature becomes almost imperceptible. This broadening also shifts the center of mass of the peaks to lower energies (the L_3 peak energy in this case is 517.2 eV) but keeps the branching ratio unchanged. In the absence of exact knowledge on the orbital shapes of the adsorbed dimer, a preliminary explanation for this behaviour shall be given with the help of the general form of dimer molecular orbitals shown in Fig. 4.6. The binding molecular orbitals are the result of adding atomic orbitals of the same orbital quantum number, in this case d -orbitals with $l=2$. The antibinding orbitals would show a sign switch along the interatomic axis, but otherwise have a similar spatial form (cf. for example [118]). The z -axis is taken as the surface normal and it is assumed that the dimer does not adsorb on the surface in a "standing" position, i.e. the interatomic axis is taken to be either x or y . Experimentally, there is no distinction between the two remaining axes, seeing as for the fourfold symmetric surface the dimer is equally likely to adsorb in either x - or y -direction and the absorption spectra do not resolve the azimuthal direction. The σ_g and δ_g orbitals are isotropic when looked either along the z - or the y -direction. The π_u orbitals however would show a significant anisotropy depending on the photon incidence angle. For example, the depicted $\pi_u(xz)$ orbital would contribute strongly to the grazing incidence spectra and weakly to the normal incidence spectra. For the other $\pi_u(xy)$ orbital, the situation would be reversed and there would hence be no measured anisotropy, if both orbitals are empty or partly occupied. If however, only the in-plane $\pi_u(xy)$ orbital is fully occupied, there can be no excitation of electrons into this orbital and the only measurable contribution to the absorption spectra will arise from the out-of-plane $\pi_u(xz)$ orbitals, giving rise to an anisotropic white line. By definition, the binding molecular orbitals are more strongly delocalized than their antibinding counterparts, so that the peak broadening in the grazing incidence white line spectra of $V_2/Cu(001)$ is most likely the result of the binding $\pi_u(xy)$ orbital being fully occupied and subsequent excitation of electrons into the partially occupied, delocalized, binding $\pi_u(xz)$ orbital.

The XMCD signal of $V_2/Cu(001)$ is significantly increased compared to the adatom, which is contrary to the theoretical studies of both Stepanyuk *et al.* and Weber *et al.*, where each time the magnetic moment per atom decreases to roughly $2.85 \mu_B$ [97, 110]. Up until now, this discrepancy can not be explained, even considering the higher spin state of the dimer due to elongated bond length, as this was taken into account for these studies as well. Also, there are pronounced differences between the two incidence angle spectra. While the dips at ~ 518 eV and ~ 525 eV get less intense upon increase of θ , the peaks at ~ 516 eV and ~ 522 eV gain in intensity. It could even be argued that the feature at ~ 516 eV switches its sign. The strongly asymmetric peak shapes in the XMCD spectra of V are a characteristic feature for early $3d$ transition metals [108] and have been tied to the expectation value of the spin moment by van der Laan [89]. Furthermore, this observation can be reasonably explained by an argument similar to the significant change in the isotropic lineshape for different incidence angles. The $\pi_u(xy)$ orbital, which would give rise to an out-of-plane magnetic moment, is already fully occupied before the excitation process and only the $\pi_u(xz)$ orbital contributes to the XMCD signal, leading to a mainly in-plane magnetization because the remaining molecular orbitals

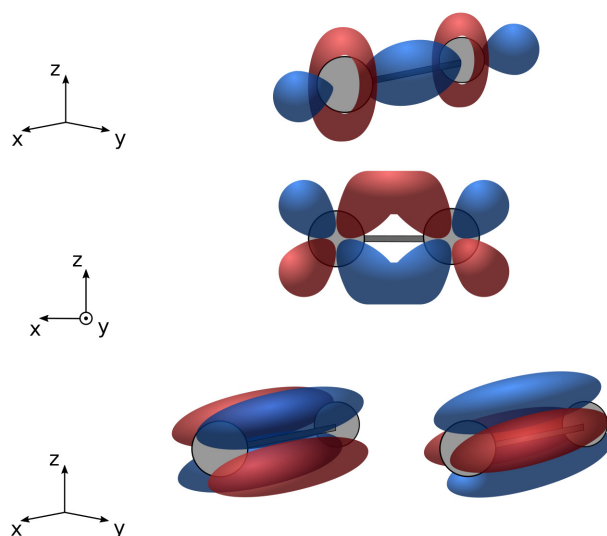


Fig. 4.6.: Schematic depiction of σ_g (top), π_u (middle) and δ_g (bottom) dimer molecular orbitals derived from the d -orbitals. The interatomic axis is taken to lie in x -direction. For π_u there exists a second orbital, which lies in the xy -plane. i.e. perpendicular to the one depicted.

do not contribute significantly to the anisotropy of the magnetic moment in this picture. Also, having mostly singly occupied orbitals with the same spin parity leads to an increased spin moment, which explains the asymmetric lineshape.

The orbital magnetic moment at $\theta = 0^\circ$ (cf. Fig. 4.5) is similar to the one for the adatom which appears contradictory to the observed stronger XMCD signal of V_2 . One can explain this by evoking the spin magnetic moment as the dominating part in the XMCD spectra of the dimer. This is hard to verify in the absence of a reliable way to obtain the spin magnetic moment from the present measurements but appears sensible, considering that due to the forced elongation of the dimer bond the ground state has $S = 3$. For the $^4F_{3/2}$ Hund's rules ground state of the atom S would be $3/2$ and while the values of the free atom and dimer can not be applied to the adsorbates straightforwardly, it can nonetheless be expected that the spin contribution to the magnetic moment is about twice as large for the dimer as it is for the adatom. This, in combination with the multipole ground state moment analysis by van der Laan [89], would in turn also explain why the peak asymmetry in the dimer's XMCD is much more pronounced than it is for the adatom,

At $\theta = 70^\circ$, the magnitude of the orbital magnetic moment is considerably larger than for normal incidence and the sign of the moment switches, meaning that the orbital moment now lies antiparallel to the external magnetic field. This can be made clearer by looking at (2.2.9):

$$\begin{aligned}
I_{XMCD} &\propto \vec{\epsilon} \cdot \vec{M} \\
&\propto \vec{B} \cdot \vec{M} \\
&\propto \vec{B} \cdot \vec{m}_S^{eff} + \vec{B} \cdot \vec{m}_L \\
&\propto B m_S^{eff} \cos(\alpha_S - \theta) + B m_L \cos(\alpha_L - \theta)
\end{aligned}
\tag{4.1.1}$$

Where in the first step, use was made of the fact that the photon polarization and the external magnetic field are kept collinear throughout the measurements. The magnetization was then expanded into the effective spin and orbital magnetic moments (cf. (2.1.4)) and in the last step the definition of the dot product was used, with $\alpha_{S,L}$ the respective angles of the spin and orbital magnetic moments with respect to the surface normal and θ the photon incidence angle. From this it can be seen that sign change in the orbital term then boils down to a sign change of $\cos(\alpha_L - \theta)$. As the sum of the orbital and spin term does not change its sign, which is evidenced by the XMCD signal keeping its general orientation, the spin term has to also keep its orientation with respect to the magnetic field and also offset the orbital moment. This entails an antiparallel alignment of the spin and orbital magnetic moments in the V dimer, matching for example results for the $\text{Fe}_{0.9}\text{V}_{0.1}$ alloy and Fe/V/Fe trilayer systems [84]. Furthermore, this matches Hund's third rule that for an atom with an outer shell that is less than half filled, the spin and orbital momenta tend to align antiparallel (cf. 2.1.2). Of course, Hund's rules can not be applied simply here, since this is neither a single atom nor is the spin-orbit coupling the main interaction. However, this serves to show that the appearance of antiparallel orbital and spin magnetic moments is not completely unreasonable.

Finally, emphasis shall be put on the absorption spectra of the adsorbed trimer (cf. the right-most panels of Fig. 4.4), starting once again with the isotropic white line spectra. In this particular case, spectra were taken at three different incidence angles, with the measurements at $\theta = 30^\circ$ serving as an intermediate step which shall become clearer later on. Just as for the Fe adsorbates before, one can see the continued trend of the lineshape becoming broader due to increased delocalization of the d -electrons. This is especially clear in the small feature at ~ 516 eV which becomes even weaker in comparison to the dimer and has now almost reverted to being a shoulder. Again, the difference is more subtle than it was in going from one atom to two, which can be rationalized by looking at the number of neighbouring atoms of each V atom. For a dimer with only hollow adsorption sites, each V atom is coordinated with four atoms of the Cu surface and one atom in the cluster. For a triangular trimer, each V atom then has six neighbours, two in the cluster and the four of the surface, which marks a 20 % increase. For free clusters on the other hand, the average number of coordination partners would double from 1 in the dimer to 2 in the triangular trimer. This strong increase in coordination number and subsequently increased electron delocalization also reflects in the difference of absorption spectra for V_2^+ and V_3^+ in the work of Hirsch *et al.*. The same reasoning can be applied to the linear trimers, where the average coordination number would increase to 16/3 for the adsorbed trimer (roughly 6 % increase) and 4/3 for the free linear trimer (33 % higher than for the dimer). It is also this increased delocalization, that is responsible for the lowering of the L_3 peak energy to 517.8 eV, a 100 meV decrease compared to the dimer.

The branching ratio of the V trimer shows a weak increase with respect to the dimer considering the experimental uncertainty. In contrast to this, the branching ratio for the free cationic trimer shows a sizeable difference to its respective dimer in the work of Hirsch *et al.* [80], also in the opposite direction of the present increase. At the present time, it can not be conclusively explained why the branching ratio increases for the adsorbed trimer, or if it is only a statistical fluctuation. Considering the evolution of the XAS peak shape, likely being a result of increased dynamic electron-core hole screening, as well as the lowered L_3 peak energy in comparison to the dimer, again due to the electron-core hole screening becoming more efficient, the branching ratio should actually drop.

From the angular evolution of the white line spectra, it can be observed that the feature at ~ 517 eV visibly decreases with increasing photon incidence angle. This feature had been identified as a possible result of the high spin ground state of the dimer, and while this lends credibility to a high spin ground state for the trimer as well, this can not be said with certainty in the absence of electronic structure calculations. Although the exact cause of this features' decrease with photon incidence angle remains to be determined, it can reasonably be explained by the binding orbitals responsible for this feature primarily lying in-plane and that the corresponding states that would be giving rise to a grazing incidence contribution are fully occupied, as was seen for the dimer.

In turning to the XMCD spectra of $V_3/Cu(001)$, the first big difference with respect to both the dimer and the adatom lies in the spectrum at $\theta = 0^\circ$ being flipped along its baseline. In accordance with (4.1.1), this can be seen as the total magnetization changing its coupling to the magnetic field. In the absence of a definite magnetic orientation to compare it to, it is however doubtful to assign either a ferromagnetic or antiferromagnetic coupling to this behaviour. Also, the strength of the XMCD signal is reduced compared to the dimer but still larger than for the trimer. While the decrease with respect to the dimer is consistent with theory, where the values were $2.76 \mu_B$ and $2.80 \mu_B$ respectively [110], the fact that the magnetization is larger than for the adatom can still not be explained. Note should be made that the assumed geometry in both of these studies was that of a linear chain, which is to be questioned given the data on the free trimers. Also, the trimer's XMCD signal presents reduced asymmetry, which could be interpreted as a reduced spin moment via the moment multipole analysis by van der Laan [89] and would fall in line with the trimer being in a low spin ground state, as was found by the calculations on free V trimers [119–121].

Since the XMCD spectrum at $\theta = 70^\circ$ is almost vanishing, implying a preferred out-of-plane orientation of the magnetization, the spectrum at $\theta = 30^\circ$ was taken. The most striking observation in this spectrum in comparison to the normal incidence one is certainly the fact that it has changed its sign, matching the one for V_1 and V_2 . To explain this switch in the XMCD signal, and the changed coupling of the magnetic moment to the magnetic field it implies, it is helpful to turn back to (4.1.1) and decompose the total magnetic moment of the trimer into the sum of the magnetic moments of each atom.

$$\begin{aligned}
I_{XMCD} &\propto \vec{B} \cdot \sum_{i=1}^3 \vec{m}_i \\
&\propto B \sum_{i=1}^3 m_i (\sin \theta \sin \alpha_i \cos(\phi - \beta_i) + \cos \theta \cos \alpha_i)
\end{aligned} \tag{4.1.2}$$

Where i is the index of the trimer's atoms and the α_i and β_i are the respective polar and azimuthal angles of each magnetic moment and θ and ϕ are the polar angle and the azimuth of the external magnetic field (cf. Fig. 4.7).

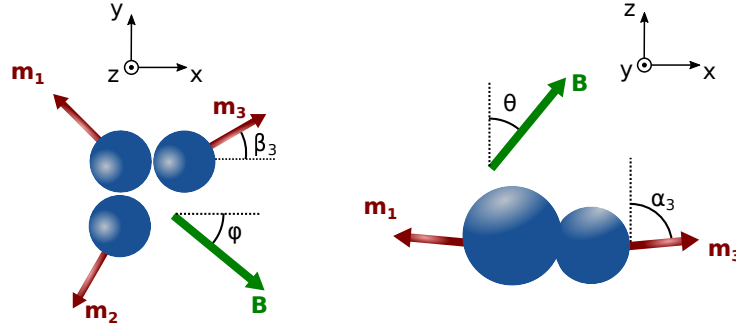


Fig. 4.7.: Schematic drawing of a pure trimer and the associated magnetic moments as a top view (left) and side view (right). The angles α_1 , α_2 , β_1 and β_2 are defined analogous to α_3 and β_3 . θ and ϕ are the polar angle and azimuth of the external magnetic field.

Since the polar angle θ of the magnetic field is confined to lie between 0° and 90° (beyond that point, the X-ray beam would not hit the sample surface anymore), both $\sin \theta$ and $\cos \theta$ remain positive at all times. The m_i are by definition vector lengths and hence positive, so the angular dependence of the sign of the XMCD signal can only come from the α_i and β_i . This leads to conclude that the reason for the observed sign change in the XMCD stems from the orientation of the individual trimer magnetic moments. Since even for the trimer in question, there are 10 parameters that can not be determined experimentally (all of the α_i , β_i , m_i and ϕ), it is futile to assign an exact magnetic configuration to the trimer. Generally, these parameters can be determined via *ab initio* theoretical techniques [122] and oftentimes, the ground states of such trimers exhibit non-collinear magnetic structures. While the sign flip encountered for V_3 could in principle be a result of non-collinear ordering, this can not be claimed with certainty as neither do all non-collinear magnetic structures lead to a sign inversion in the XMCD nor does a sign inversion have to necessarily indicate a non-collinear magnetic structure. To exemplify this, the results of (4.1.2) as a function of θ have been plotted in Fig. 4.8 for specific sets of parameters, that were either directly taken from the calculations of a Cr trimer on Fe(3 ML)/Cu(001), or are a variation thereof (cf. Tab. 4.4 for the values)[123].

Focusing solely on the sign of the XMCD strength shows that the Cr trimer in its non-collinear ground state would not lead to an inverted sign of the XMCD signal and that both collinear (FM and AFM) cases would on the other hand show such a change. Therefore, the shape of the XMCD signal alone can not be used as an indicator for non-collinear magnetic

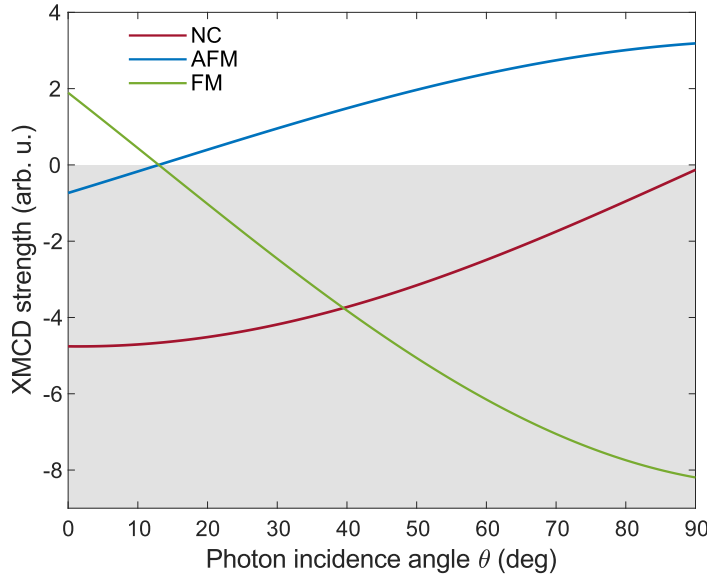


Fig. 4.8.: Simulated XMCD strength as a function of photon incidence angle for a non-collinear (NC), antiferromagnetic (AFM) and ferromagnetic (FM) trimer structure. The exact parameters are listed in Tab. 4.4. The area shaded in grey serves to highlight the sign switch in the XMCD.

	m_1 (μ_B)	$m_{2,3}$ (μ_B)	α_1 ($^\circ$)	$\alpha_{2,3}$ ($^\circ$)	$\phi - \beta_1$ ($^\circ$)	$\phi - \beta_{2,3}$ ($^\circ$)
NC	2.57	2.92	77	156	180	0
AFM	2.57	2.92	77	103	180	0
FM	2.57	2.92	77	77	180	180

Tab. 4.4.: Parameters inserted into (4.1.2) leading the three curves plotted in Fig. 4.7. The non-collinear (NC) values are taken directly from calculations by Lounis concerning $\text{Cr}_3/\text{Fe}(3 \text{ ML})/\text{Cu}(001)$ [123]. The antiferromagnetic (AFM) and ferromagnetic (FM) case are variations of those parameters to gain the desired magnetic configuration.

ordering. Furthermore, in this short exploration it was assumed that the angles of the individual magnetic moments stay fixed in place independently of the orientation of the magnetic field. This would only occur if the coupling between the magnetic moments is very large with respect to the magnetic field. In general, one would have to determine the needed parameters from e.g. Korringa-Kohn-Rostoker method calculations [122] and then insert those in (4.1.2), which is beyond the scope of this work. It can however be stated that the magnetic moments do not align with the surface normal, nor are they parallel to the surface. Rather, they show an inclination.

This behaviour of the XMCD signal of $\text{V}_3/\text{Cu}(001)$ carries over to the calculated orbital moment (cf. Fig. 4.5). For normal incidence, the orbital magnetic moment presents a negative sign and a magnitude below those of the adatom and dimer. This is consistent with the strength of the XMCD but raises a question concerning the spin moment. For the dimer, it was assumed that the spin moment dominates the magnetic response, to an extent where the sign change of

the orbital moment at grazing incidence did not register as a sign change for the total magnetic moment. In contrast to this, it can be seen that the sign of the XMCD correlates with the sign of the orbital moment. This can either mean that the spin contribution to the total magnetic moment is no longer dominant, or it could mean that the spin moment has the same angular dependence, possibly both. Seeing the weak peak asymmetry in the trimer's XMCD spectra, it is reasonable to assume that the spin contribution is reduced compared to the dimer. Again, this can not be explained conclusively from the available data and would need to be confirmed by other means.



Fig. 4.9.: Proposed magnetic easy axes of the pure V adsorbates. From left to right the number of V atoms increases from one to three. The depictions are meant as schematics and are not quantitative.

In light of the difficulties in determining the orientation of the magnetization, the proposed configurations in Fig. 4.9 should be viewed with caution.

4.2. X-ray induced spectral changes

Due to the on-the-fly measurement mode that was implemented at the beamline just before the relevant beamtimes (cf. 3.3.1), it was possible to take absorption spectra more rapidly and with lower photon doses on the sample. A side effect of this was the observation that the XAS lines of adsorbates responded to the photon beam. As is visible in Fig. 4.10, over the course of roughly 3 minutes, the signal changes its shape drastically with the changes after this point being confined to the experimental uncertainty. To better gauge the temporal evolution of the different features, the XAS lines were normalized to their respective integrated area. The indicated times on the spectra mark the exposure time, taken each time the photon energy passes 707.6 eV. Due to the spatial dimensions of the synchrotron beam, it was possible to scan the sample surface and confirm that after moving to a spot 100 μm away, the spectra on that new spot were "fresh" again and followed the same evolution to the "final" state.

There has been a sizable body of work concerning similar observations in organometallic complexes containing transition metals, most notably Fe (cf. for example [51–53]). There it was believed to be an example of soft X-ray induced excited spin state trapping (SOXIESST, cf. 2.3.2). As the name suggests, the soft X-ray irradiation promotes the transition metal from a low spin ground state to an excited high spin state, where the system can remain for several hours, depending on the overall temperature [124]. Alternatively, the sample can be reset to the low spin state by heating [52, 53]. These reports bring forth the argument that the lower energetic peak is indicative of the high spin state [125]. Applied to the present case, this would mean that $\text{Fe}_2/\text{Cu}(001)$ should switch from a high spin state to a lower one. Depending on which of the spin states is the ground state, this could imply either a SOXIESST process or the overcoming of an energy barrier in order to revert back to the true ground state in a process called reverse SOXIESST (rev-SOXIESST)[53].

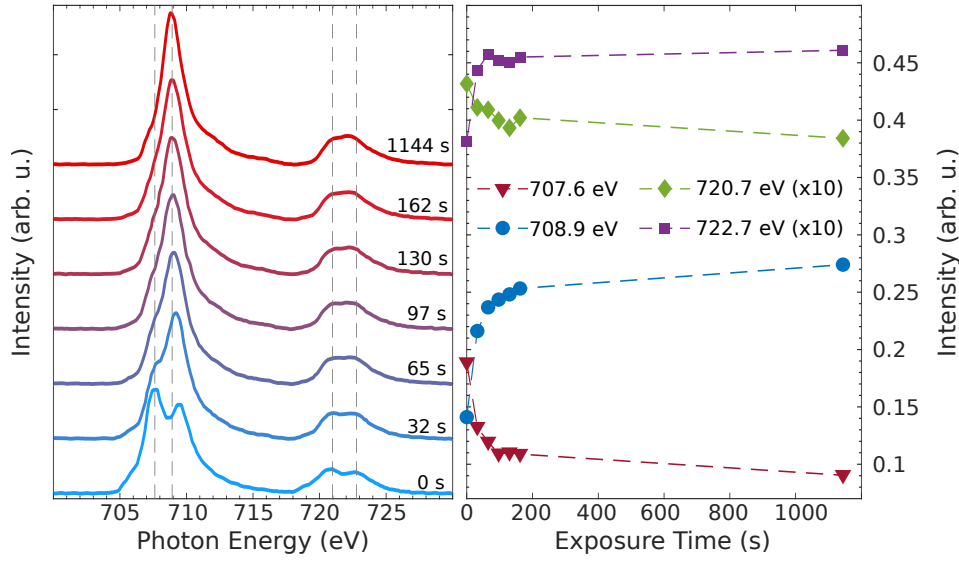


Fig. 4.10.: (Left) Time evolution of X-ray absorption spectra of Fe₂/Cu(001). All spectra were taken on the same sample spot under the same conditions, were normalized to their respective integrated area and are vertically offset for clarity. The numbers close to each spectrum indicate the X-ray exposure time on the spot, measured when the photon energy passes 707.6 eV. (Right) Temporal evolution of the XAS intensity at the energies indicated by the vertical lines in the left panel.

The right panel of Fig. 4.10 shows the evolution of features at four specific energies with exposure time. Following the work of Davesne *et al.*, the process was modelled as the interconversion between two states $S_{1,2}$ with two separate rate constants, i.e. $S_1 \xrightarrow{k_1} S_2$ and $S_2 \xrightarrow{k_2} S_1$. This leads to the differential rate equation for the amount of adsorbates in state S_2 , notated as $[S_2]$.

$$\frac{d[S_2]}{dt} = k_1[S_1] - k_2[S_2] \quad (4.2.1)$$

This equation, together with the assumptions that the system is either in S_1 or S_2 , i.e. $[S_1] = 1 - [S_2]$, and that before irradiation the system is solely in S_1 , i.e. $[S_2] = 0$ for $t = 0$, leads to expressions for the time evolution of the two states:

$$\begin{aligned} [S_1](t) &= \frac{k_2}{k_1 + k_2} + \frac{k_1}{k_1 + k_2} e^{-(k_1+k_2)t} \\ [S_2](t) &= \frac{k_1}{k_1 + k_2} \left(1 - e^{-(k_1+k_2)t} \right) \end{aligned} \quad (4.2.2)$$

Fitting of the experimental curves to these equations gives the rate constants $k_{1,2}$, as well as the characteristic time constant of the exponential evolution $1/(k_1 + k_2)$. The best fit values of all of these parameters can be found in Tab. 4.5.

Both features at the L_3 edge change on essentially the same time scale, implying that spectral weight is redistributed between these two. However, for the L_2 features the time constants

Energy (eV)	k_1 (10^{-3}s^{-1})	k_2 (10^{-3}s^{-1})	$(k_1 + k_2)^{-1}$ (s)
707.6	2.32	24.91	36.7
708.9	2.94	22.32	39.6
720.7	0.04	8.41	118.4
722.7	0.34	645.82	21.7

Tab. 4.5.: Rate constants k_1 and k_2 obtained by fitting the time evolution curves in Fig. 4.10 with the model in (4.2.2). Also included is the characteristic time constant of the exponential term.

are not consistent. This discrepancy is likely due to choosing the intensity at a single point as indicator for the evolution of the states. In the cited works concerning SOXIESST, the temporal evolution was deduced from fitting the spectrum with the spectra of pure initial and final states. Because it is not known if the spectra at the respective ends of the time series arise from pure states, this procedure can not be applied here. Consequently, the intensities can be a sum of contributions from fresh and final states and the method of extracting $[S_1]$ and $[S_1]$ would have to take this into account.

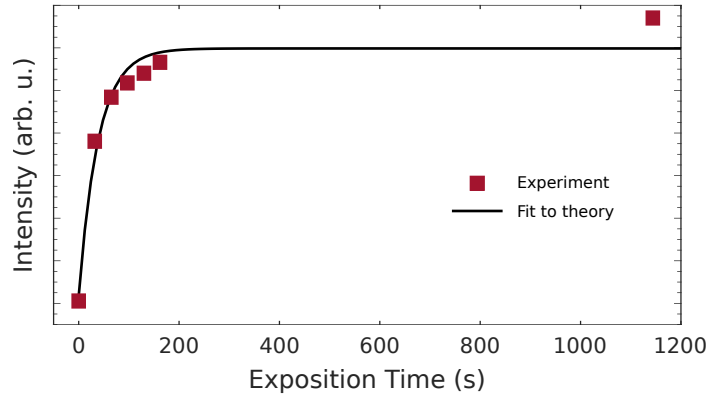


Fig. 4.11.: Temporal evolution of the XAS feature at 708.9 eV for $\text{Fe}_2/\text{Cu}(001)$ during irradiation with soft X-rays. Also depicted are best fits to the data of (4.2.2).

As can be seen for the case of the feature at 708.9 eV in Fig. 4.11, the agreement of the fit with the data is somewhat lacking. Rather, the theoretical curve levels off too early and the difference to the last data point is significant (although not shown, the same behaviour is observed for the time evolution of the other spectra). It has been brought up that spin state trapping should be viewed as a cooperative effect and that the rate constant of the $S_2 \rightarrow S_1$ conversion should be expressed as $k_2 = k_2^0 e^{-\alpha(T)[S_2]}$ with $\alpha(T)$ proportional to the inverse temperature [126, 127]. Davesne *et al.* have achieved excellent agreement between their theoretical fits and the data using this approach [52]. However, since the treatment in this work is only preliminary and data treatment based on whole spectra rather than single spectral features would be more suited (cf. the varying time constants for the L_2 and L_3 features), the necessary adaptations of the rate equations appear premature, especially given that the resulting differential equations would be rather complicated to solve, possibly leading to solutions in terms of non-elementary

Adsorbate	$m_L (\mu_B/n_h)$	$m_S^{eff} (\mu_B/n_h)$	m_L/m_S^{eff}	B
Fe ₁ , fresh	0.046 ± 0.005	0.103 ± 0.010	0.45 ± 0.05	0.84 ± 0.04
Fe ₁ , final	0.021 ± 0.003	0.105 ± 0.012	0.20 ± 0.04	0.83 ± 0.04

Tab. 4.6.: Characteristic values extracted from the Fe₁/Cu(001) XAS and XMCD spectra in Fig. 4.12 for a new measurement spot as well as after long time irradiation with X-rays.

mathematical functions.

Lehnert *et al.* have reported a somewhat similar temporal behaviour for Fe/Al₂O₃/Ni₃Al, where the spectrum height decreased over time due to what was assumed to be photon induced desorption of adsorbates [96]. While the relative weight of the spectral features remained constant in that case, it can be clearly seen from the right side of Fig. 4.10, that the height of some of the features increase while for others there is a decrease. The explanation by Lehnert *et al.* thus should not hold in this case. Also the timescale at which the desorption is happening in their work (about 6500 s) is far slower than the time scales observed in this work, despite their photon flux being $\sim 10^{13}$ photons/s, or roughly a factor of 3-4 higher than the present photon flux.

Another fact standing in the way of the observed effect being due to desorption is that the integrated area under the spectra actually increases over time. Such an increase would rather point towards the adsorbates agglomerating under the effect of the X-ray beam, forming larger structures. This would however entail that e.g. the L_3 peaks of an adatom and the final agglomerate, whatever its exact size might be, would have to be separated by around 1.3 eV. While not impossible, it appears unlikely, considering for example the results of Pacchioni *et al.* for the evolution of small Fe clusters on Cu(111), where the energetic shift of the peaks is negligible [9].

To test if the observed changes are actually the result of a spin state change in a (reverse) SOXIESST process, the XAS and XMCD spectra of Fe₁/Cu(001), both on a fresh and long-time irradiated spot, were taken in a ± 7 T magnetic field (cf. Fig. 4.12) in normal incidence of the photon beam and at full photon flux. It should be noted, that for the fresh state in Fe₂/Cu(001), the lower energetic peak is dominant, which is not the case for the fresh spectrum of the adatom. The exact cause of this is not known, it could however be an indication that there has already been a significant portion of Fe adatoms changing states before the investigation began. It can also be seen that the lower energetic L_3 peak in the XAS corresponds to a lower energetic peak in the XMCD as well, becoming smaller after photon irradiation but not disappearing. Contrary to this, the L_2 peak at ~ 522.7 eV in the XMCD spectrum for the initial spin state is almost nonexistent and only becomes sizable for the final state. At the same time, the structure at ~ 519 eV in the initial XAS and XMCD spectra vanishes completely after photon irradiation. This reinforces that the observed process is more than adsorbate desorption and that there is an interconversion between states of different magnetic configuration. It should also be noted that for the initial spectrum, the ratio of the lower L_3 peak height to the larger one in the white line is bigger than it is for the XMCD, potentially indicating a lesser magnetic contribution from that peak.

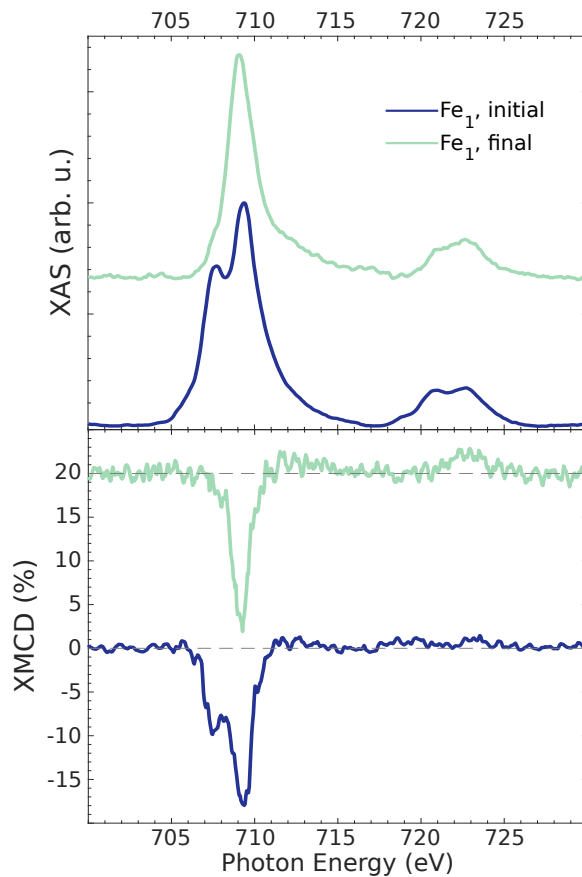


Fig. 4.12.: Background subtracted white line spectra (top) of Fe_1 on Cu(001) taken at normal incidence on a fresh sample spot and on a spot that has been irradiated for a long time. The corresponding XMCD spectra at ± 7 T are shown on the bottom. All spectra are normalized to the L_3 peak of the respective white line and vertically offset for clarity.

Via use of the sum rules, the effective spin magnetic moments of the respective XMCD spectra were extracted and can be found in Tab. 4.6, where it can be seen that they are identical within the error bounds. However, recalling the preferred in-plane magnetization of the irradiated Fe adatom (cf. Tab. 4.1) it should be noted that the spin magnetic moment of that same adatom does show significant change as a function of incidence angle. Without corresponding angle dependent data on the fresh spot, it can not be concluded if these magnetic moments are the upper limit of the adatom in the fresh spot or if the values at grazing incidence are even higher. Therefore a spin state switching can neither be confirmed nor ruled out based on these values alone. However, the branching ratio changes only slightly with photon irradiation and based on the calculations of Thole and van der Laan, one would expect the branching ratio to differ more drastically for different spin states [35]. While this casts reasonable doubts on the hypothesis that the spectral changes are a result of spin state switching, it should not be discarded entirely.

Given the X-ray absorption's sensitivity to the environment of the investigated element, the observed changes could also be a result of adsorbates moving from one adsorption site to an-

other. This effect is prominent e.g. in Fe_3O_4 , where the XAS and XMCD can be accurately described as a combination of Fe^{2+} and Fe^{3+} ions in octahedral lattice sites and Fe^{3+} ions in tetrahedral sites [128]. Considering the lower branching ratio in the longtime irradiated sample, this could signify that the adatom changes from either a top position to a position between two Cu atoms or to a hollow adsorption site, since the increased coordination with the substrate would lead to stronger delocalization of the d -electrons and lower the branching ratio. This explanation is bolstered by the orbital magnetic moment's strong decrease with photon irradiation. The spin is only indirectly coupled to the geometry of a system, via the spin-orbit interaction or via crystal field splitting, and thus would not be subject to as strong a change as the orbital moment, which is very much a reflection of the environment of an atom. Still, just as for the spin moment, it can not be stated if the extracted orbital moment is lying preferably in-plane or out-of-plane, and this assumption is to be viewed cautiously.

It can be expected that the process of adsorption site switching leads to an energetically favorable state and hence would not be reversible at low temperatures. Therefore, this should be distinguishable from a possible spin state trapping after a long enough relaxation time.

Recalling the assumed d^7 configuration of the Fe adatom, another possible effect could be that the change in the spectra stems from Fe changing from a d^6 to a d^7 configuration under the influence of the X-ray beam. In absence of XAS data for Fe d^7 species, with the exception of the results of Gambardella *et al.* [81], this hypothesis is difficult to test. However, considering the Hund's rule ground state for a d^6 configuration has $S = 2$ and the d^7 ground state has $S = 3/2$ this would go against the observed trend of the spin moments staying mostly the same.

As these spectral changes were a byproduct of the beamtimes, there was no further investigative focus put into this and there can be no conclusive answer given here. Still, this effect is intriguing and should be investigated further. In order to have reproducible results and change as few parameters as possible, the spectra analyzed in the other sections of this chapter were taken after plenty of photon irradiation, i.e. in the final state.

4.3. Alloy adsorbates

After the pure adatoms, dimers and trimers, focus shall now be put on the Fe_1V_1 dimer and the Fe_1V_2 trimer to gain information about the interplay between these species. To this end, the evaluation of the results proceeds with cluster size instead of element, as was the case before.

4.3.1. Fe_1V_1

Fig. 4.13 presents XAS and XMCD spectra for the alloy dimer at the $L_{2,3}$ edges for four different photon incidence angles, namely 0° , 15° , 30° and 70° . If one is to compare the alloy dimer to any of the pure clusters, it is most logical to also choose the pure dimers, simply because the number of constituents and the geometry are the same. Just as the addition of a second atom to the pure adsorbates led to a broadening of the spectra and loss of the multiplet features, the same can be said for the addition of a different element. Nonetheless, the amount of broadening varies quite drastically. The normal incidence XAS for V shows a stronger low energy feature compared to V_2 . In light of the explanation that this spectral broadening is a result of increas-

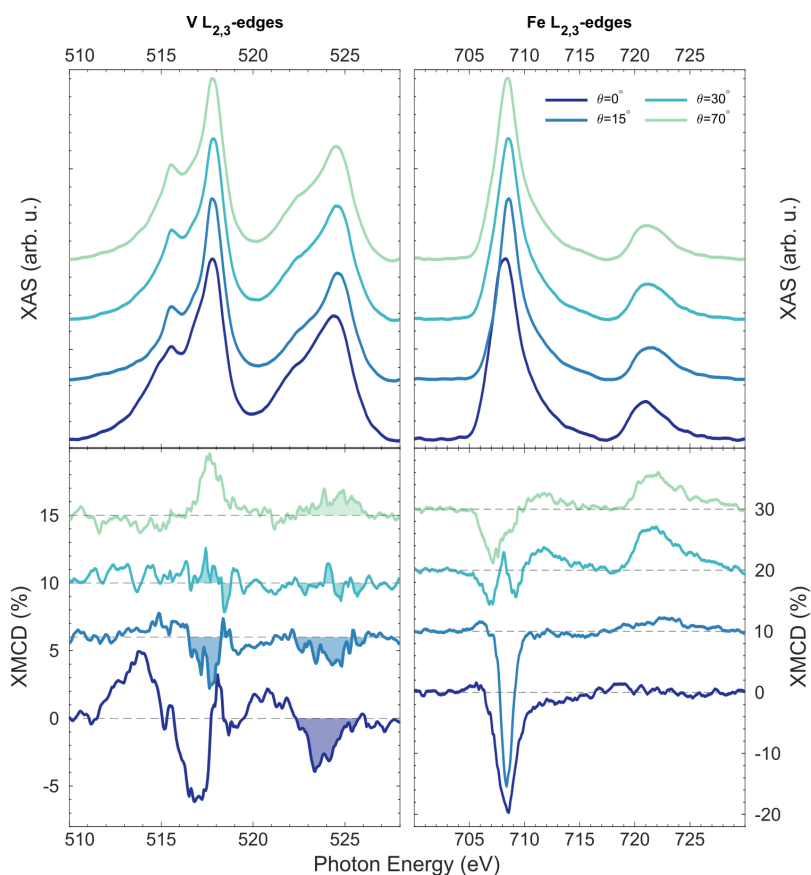


Fig. 4.13.: (Top) Background subtracted white line spectra for the Fe $L_{2,3}$ edges (right) and the V $L_{2,3}$ edges (left) of the Fe_1V_1 dimer, taken at different values of θ . (Bottom) XMCD spectra in a ± 7 T field, corresponding to the top row. All spectra have been normalized to the L_3 peak of their respective white line and vertically offset for better clarity.

ingly delocalized valence electrons, this would imply that the delocalization in the alloy dimer is less pronounced than it was for the pure V dimer. This becomes even more striking when considering that because of the higher scan speed of the beamline (cf. 3.3.1) one would expect the spectrum of the alloy cluster to be generally more broad. Additionally, the onset of the L_3 edge lies much earlier with respect to the peak as it did in the pure dimer, signifying a number of valence states that are either lower in energy than they were in V_2 , or that only appeared because of the hybridization with Fe.

Conversely, the XAS for Fe shows no multiplet features after coming into contact with V. Rather, the spectrum appears bulk-like (compare e.g. [86]). While the disappearance of the shoulder at the L_3 peak could be explained by the increased broadening due to the higher scan speed of the measurements, the same is not true for the L_2 edge. Not only does the edge lose texture but also the general shape changes, from a higher intensity at higher excitation energies for the pure dimer to a higher intensity at lower energies for the alloy.

Intuitively, this difference in behaviour can be explained by the effective nuclear charges of V

and Fe. The higher charge of the Fe nucleus with respect to V leads to the electrons becoming more tightly bound, i.e. their radial wavefunction extending less far from the nucleus. This can be quantified in terms of the effective nuclear charge Z_{eff} as calculated by Slater's rules (see for example [118]). For Fe, this yields $Z_{eff}(2p) = 21.85$ and $Z_{eff}(3d) = 6.25$ and for V $Z_{eff}(2p) = 18.85$ and $Z_{eff}(3d) = 4.30$. This implies that in case of Fe_1V_1 , because of the larger effective charge, the valence molecular orbitals derived from the atomic d -orbitals are more localized on the dimer than they are for V_2 , resulting in less broadening in the white line spectra at the V $L_{2,3}$ edges. Compared to Fe_2 , the situation is reversed and the valence molecular orbitals extend further from the alloy dimer than they would from the pure dimer, which leads to a broader white line spectrum.

Adsorbate	Edges	B	$E(L_3)$ (eV)	ΔE_{2p} (eV)
Fe_1V_1	Fe $L_{2,3}$	0.81 ± 0.04	708.3	12.7 ± 0.25
	V $L_{2,3}$	0.58 ± 0.03	517.8	6.7 ± 0.25

Tab. 4.7.: Branching ratios (B), L_3 peak positions and energetic separation between the two L -edges (ΔE_{2p}) for $\text{Fe}_1\text{V}_1/\text{Cu}(001)$, extracted from the white line spectra at $\theta = 0^\circ$ in Fig. 4.13. All other incidence angles are omitted, as the values are isotropic. The values for both constituents are listed separately.

This effect can also be seen in the branching ratios gained from the $\theta = 0^\circ$ white lines of the dimer's constituents (cf. Tab. 4.7). For V, the value of 0.58 ± 0.03 is higher than the 0.54 ± 0.03 of $\text{V}_2/\text{Cu}(001)$ which again points towards a reduced screening of the Coulomb interaction of the $3d$ electrons with the core hole, resulting from a lesser degree of delocalization. The opposite happens for the Fe branching ratio, which is lower than the 0.82 ± 0.04 of $\text{Fe}_2/\text{Cu}(001)$, albeit to a lesser extent. In this regard it is also interesting to note, that the apparent spin-orbit splitting ΔE_{2p} has undergone a drastic change for Fe and a somewhat smaller change in the opposite direction for V. Recalling that the spin-orbit coupling is proportional to the radial derivative of the atomic potential (see for example [42]), the potential acting on the Fe electrons becomes weaker when the second Fe atom is exchanged for a V atom, agreeing with the lowered Z_{eff} of V. The lowered apparent spin-orbit splitting for Fe should in principle lead to a higher branching ratio than for the pure dimer [35], however the effect of increased delocalization outweighs the reduced spin-orbit splitting in this case. For V, the same explanation holds, albeit with the signs of the effects reversed.

It is likely that this changed potential, compared to the pure dimer, is also the reason for the significant shift to lower energies in the L_3 peak of Fe, since the dynamic screening effect of the delocalized valence electrons tends to lower the excitation energy [38]. In this regard, the simultaneous drop of the V L_3 peak energy can not be explained as easily, since it would be expected that the excitation energy rises. It is possible that this is due to a delocalization effect of the $2p$ electrons in the initial state, although this can not be stated with certainty.

Upon increase of the photon incidence angle, the first thing that becomes noticeable in the spectrum of Fe is a positive energetic shift for all the spectra above 0° . This can be attributed to contributions from either more strongly bound $3d$ valence electrons at increased angles or a higher binding energy of the $2p$ electrons. While for Fe the overall spectral shape remains the

same, there are clear changes at V edge white lines. Firstly, the onset of the L_3 edge shifts to higher energies, closer to the L_3 peak. Since the L_3 peak itself does not shift, this is likely the result of low-lying, unoccupied molecular orbitals that are oriented parallel to the Cu surface and whose contributions to the white line spectra disappear at higher incidence angles.

At this point, it is helpful to identify these orbitals with the help of group theory. By its very nature, the free alloy dimer has no inversion symmetry, which reduces its point group from $D_{\infty h}$ to $C_{\infty v}$ in pure dimers. Under the same assumptions that were made for the pure V dimer adsorbed on the Cu(001) surface, the designations of the irreducible representations largely carry over (cf. Fig. 4.6), with the exception that the "g" and "u" labels are dropped. There are thus two degenerate π orbitals, corresponding to the sum of the d_{xy} and d_{xz} orbitals of the two atoms. Interaction with the surface leads to symmetry lowering to the C_s group, resulting in the splitting of the two π orbitals, with $\pi(xy)$ being parallel to the surface. Hence, it is this unoccupied (or partially occupied) $\pi(xy)$ orbital that most likely gives rise to these observed features. At the increased incidence angles, the probing of this orbital reduces significantly, leading to the disappearance of spectral intensity at these energies. This effect leads to a better visibility of the multiplet feature at ~ 515.5 eV. Furthermore, the feature at ~ 516.9 eV, which was present in the pure dimer and was taken as an indicator of a high spin ground state, is also present in this case, implying that the spins of the V atom in this alloy are also mostly parallel to each other. Also, this feature weakens with increasing photon incidence angle, which was obscured in the pure dimer but could be observed in $V_3/\text{Cu}(001)$. This decrease is likely also caused by the orbitals being probed at grazing incidence angles being already occupied and hence showing no spectral features.

Turning now to the XMCD spectra for both elements, it can be seen that the L_3 edge of V has a positive onset before going below zero. In combination with the mainly negative intensity at the Fe L_3 edge, this indicates an antiferromagnetic coupling between the two atoms. This finding agrees with the results of density functional theoretic calculations for the free Fe_1V_1 dimer [116, 129], as well as with experimental results on thin V films on Fe(100) [130], Fe/V superlattices [131] and $\text{Fe}_{0.9}\text{V}_{0.1}$ alloys and Fe/V/Fe trilayers [84]. While the general shape of the V XMCD does match the ones for the literature, there are nonetheless differences, especially in the region between the L_3 and L_2 edges (roughly 517 eV to 520 eV). A possible explanation for this is the overall more molecular system in the present work. The cited studies concern themselves with systems closer to bulk, whereas it was shown that the adsorbed dimer has remnants of the atomic species. Furthermore, the interatomic distance between Fe and V in these works was defined by the respective lattice parameters of Fe and V while the adsorbed dimer has to conform to the lattice parameter of the Cu substrate.

Just as for $V_3/\text{Cu}(001)$, the most striking result of the increased angle of incidence comes from the sign switch of the XMCD for $\theta \geq 30^\circ$. In contrast to the trimer however, this change can be clearly attributed to a non-collinear arrangement of magnetic moments. The absence of a similar sign shift for the Fe magnetic moment indicates that not only does the orientation of the V moment change from antiparallel to parallel with respect to the external field, but that its orientation with respect to the Fe magnetic moment undergoes a comparable evolution. In a way, the Fe atom serves as a probe for the magnetic moment of V, and vice versa.

In looking back to 2.1.6, the assumptions of Radwański are valid in this case, seeing as the magnetic moments of the respective sublattices are always rigidly coupled in the trivial case of

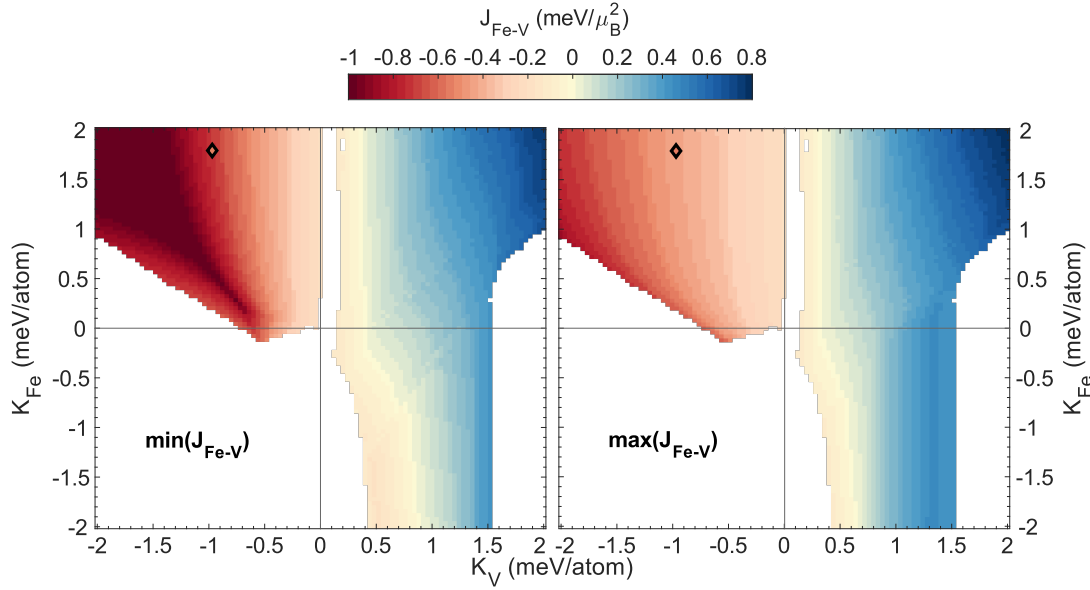


Fig. 4.14.: Results of the two magnetic sublattice model for Fe_1V_1 . The assumed magnetic moments were $2.27 \mu_B$ and $0.99 \mu_B$ for Fe and V respectively. For every pair of anisotropy constants $K_{Fe,V}$ the left (right) panel indicates the lowest (highest) J_{Fe-V} value for which the energetically lowest configuration of magnetic moments recreates the sign flip seen in the XMCD data. The diamond markers show the parameter tuple that best approaches the measured XMCD strengths.

single atoms, and one can use the two magnetic sublattices model to gain information about the exact orientation of the magnetic moments. To this end, x and y in (2.1.19) were both set to one and in the absence of absolute moments from this work, the respective magnetic moments were taken from the $\text{Fe}_{0.9}\text{V}_{0.1}$ alloy in [84]. This gives the value of $2.27 \mu_B$ for Fe and $0.99 \mu_B$ for V. The exchange constant J_{Fe-V} as well as the two anisotropy constants $K_{uni}^{Fe,V}$ were taken as free parameters and J_{Fe-V} was varied in the range of -1 to $1 \text{ meV}/\mu_b^2$. The anisotropy constants were both taken from the range of values between -2 and 2 meV/atom . For each combination of the three parameters as well as each incidence angle θ , a numerical minimization of the energy was performed in order to find the most favorable configuration of magnetic moments. The minimal angles α_{Fe} and α_V were then inserted into (2.2.9) to check if the sign of the XMCD strength resulting from those angles would recreate the observed XMCD strengths. In particular, it was searched for angles that give $\cos(\alpha_V - \theta) > 0$ when $\theta \geq 30^\circ$ while having $\cos(\alpha_{Fe} - \theta) > 0$ at all times.

If these calculations were to find suitable configurations then the corresponding parameter space would be three dimensional, because of the three free parameters. As written documents do not lend themselves to clearly show three dimensional data of this type, it was opted to show these results as a two dimensional colour coded map instead (cf. Fig. 4.14). Every colored point on these maps represents a combination of the three parameters that results in the desired sign flip of the V XMCD, with the color information encoding the exchange constant value. To convey the range of exchange constants that make up the parameter space, the lowest value of J_{Fe-V} that still produces the sign flip is shown in the left panel, while the highest possible value

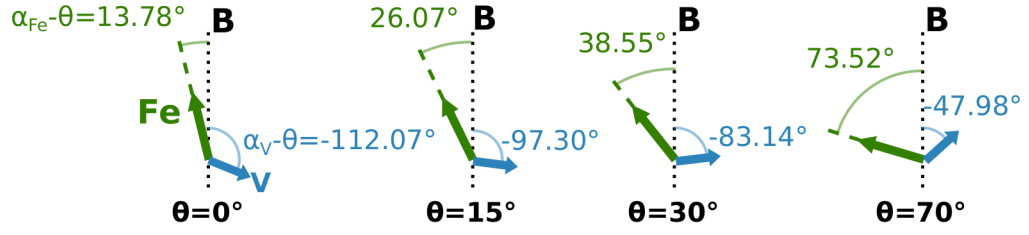


Fig. 4.15.: Calculated magnetic moment orientations resulting in minimal energy for all measurement angles. The free parameters were $J_{Fe-V} = -0.575 \pm 0.005 \text{ meV}/\mu_B^2$, $K_{uni}^{Fe} = 1.80 \pm 0.01 \text{ meV/atom}$ and $K_{uni}^V = -0.96 \pm 0.01 \text{ meV/atom}$. The angles are shown with respect to the magnetic field to increase visibility.

can be seen in the panel in the right panel .

For the parameter region with $K_{uni}^V \leq 0$ for example it can be seen that all appropriate values of J_{Fe-V} are negative, indicating an antiferromagnetic coupling between Fe and V, as has been seen in the literature. Furthermore, truncating J_{Fe-V} at $-1 \text{ meV}/\mu_B^2$ cuts off some of the parameter space, implying that for combinations of increasingly large anisotropy constants the sign switch can be achieved with bigger exchange constants. Not all parameter tuples were checked to see if the minimal energy configuration found by the calculation was, in fact, the global minimum or just a local minimum. This becomes especially apparent for the region where $K_{uni}^V > 0$ and $K_{uni}^{Fe} > 0$, meaning that for both atoms an out-of-plane orientation of the magnetic moment is favored. In combination with the positive coupling exchange constant, implying ferromagnetic coupling of the magnetic moments, this would result in the Fe and V magnetic moments being aligned parallel to each other and the surface normal. This clearly is a solution that can not produce XMCD signals of differing sign for both atoms. Indeed, looking at the complete energy landscape of the parameter configuration as a function of α_{Fe} and α_V , reveals a global minimum that does not satisfy the imposed conditions. In the region with negative K_{uni}^V however, some of the supposedly valid parameter combinations were checked at random, by looking at the complete energy landscape, always confirming the results of the minimization procedure. Thus it is probably best to restrict the parameter space to $K_{uni}^V < 0$.

This choice is confirmed by the black bordered diamond marker shown in Fig. 4.14. It is the result of not only confirming that the signs resulting from (2.2.9) for the minimum energy configuration match the measurements but also imposing that the simulated strengths of the V XMCD at $\theta = 15^\circ$ and $\theta = 30^\circ$ agree well with the peak-to-peak signal heights of the experimental results. While this would have to be confirmed by independent measurements on the parameters in question, it is reasonable that this combination of parameters gives the closest match to the actual measured alloy dimer. The values at this point are $J_{Fe-V} = -0.575 \pm 0.005 \text{ meV}/\mu_B^2$, $K_{uni}^{Fe} = 1.80 \pm 0.01 \text{ meV/atom}$ and $K_{uni}^V = -0.96 \pm 0.01 \text{ meV/atom}$. It should be noted that the marker does not lie on any of the boundaries, meaning that probable fringe behaviour of the magnetic moments' angles can be ruled out. Furthermore, the energy landscapes for each value of θ were checked by hand to confirm that the minimization algorithm converged to the global minimum. The resulting angles, shown in Fig. 4.15, reveal that Fe and V are indeed arranged in a non-collinear manner for every photon incidence angle. While this

was surmised for the V_3 adsorbate but could ultimately not be proven, it becomes quite clear in this case.

Compared to the anisotropy value of $4.8 \mu\text{eV}/\text{atom}$ in bulk bcc Fe (see for example [13]), the present value of K_{uni}^{Fe} is extremely high. However, an increase in anisotropy is expected upon lowering the symmetry group of an atom, as is the case here. This has been confirmed experimentally by Gambardella *et al.* for Co atoms on Pt(111), where $K = 9.3 \pm 1.6 \text{ meV}/\text{atom}$ was found [17], a dramatic increase compared to the $0.046 \text{ meV}/\text{atom}$ in bulk Co [13]. Similarly, Pacchioni *et al.* found $K = 1.80 \pm 0.4 \text{ meV}/\text{atom}$ for adatoms on a Cu(111) surface, matching the present results perfectly [9]. For the V constituent, the negative sign of the anisotropy constant points towards the V magnetic moment lying preferably in-plane. This shows again, that the noncollinearity results from the competition of the V moment's optimal orientation and the Fe moment's preferred out-of-plane easy axis. SQUID measurements by Farle *et al.* have yielded an anisotropy energy of $5.0 \mu\text{eV}$ for Fe_4V_4 superlattices, favoring an in-plane magnetization. In the same work, a value $2.0 \mu\text{eV}$ was found for Fe_2V_5 superlattices, this time in favor of an out-of-plane magnetization [132]. Comparing these values to the sum of the present anisotropy constants, namely 0.84 meV , shows that, just as for the Fe atoms on Cu(111) [9] and Co atoms on Pt(111) [17], the anisotropy increases drastically for adsorbates compared to extended systems as a result of the lowered symmetry. This establishes that the apparent overall anisotropy of the magnetization depends on the stoichiometry of the alloy. However, While the present Fe_1V_1 dimer has an overall out-of-plane orientation of the magnetic moments, the superlattice that resembles this at least stoichiometrically (Fe_4V_4) prefers an in-plane magnetization. This shows that comparisons between the reduced system in this work and the extended alloy systems that have been investigated before should be done cautiously.

The overall shape of the Fe XMCD and angular evolution thereof shall be of interest in the following. In normal incidence, the region of negative intensity after the main L_3 peak resembles results features that have been observed in the spectra of Co and Ni bulk compounds [108]. In that work, they were attributed to diffuse magnetism arising from the sp -band but this interpretation seems unsuited for the present case since the intensity of the feature shows angular evolution, which would not be expected if it were the result of sp -like magnetic orbitals. Considering the intensity of this feature follows a similar trend to the main L_3 peak of V, it can be argued that this stems from a binding molecular d -orbital between the two atoms. Furthermore, it can likely be identified as arising from a δ -orbital, seeing as its angular evolution undergoes a continuous evolution and a sign change rather than being isotropic, like a σ -orbital would or vanishing at either end of the incidence angle range, as one would expect for an anisotropic π -orbital. Contrary to this, the initially positive feature at the lower energetic side of the Fe L_3 peak evolves to become negative for $\theta \geq 30^\circ$, which shows that the magnetic moments arising from these two orbitals are coupled antiferromagnetically.

The flip of the V XMCD sign coincides with the appearance of a split L_3 peak of Fe, the lower energetic part of which seems to blend together with the initially positive feature mentioned before. From the white line absorption spectrum, it can be seen that the L_3 peak position does not shift, signifying that the difference is unlikely to arise from the orientation of molecular orbitals. Instead, this shows that the magnetic signatures of the molecular orbitals serving as final states are different. One reason for this difference could be that the corresponding orbitals couple differently to the surroundings, as would be the case if one considers that according

to Gutsev *et al.* the Fe_1V_1 dimer has both binding and antibinding δ -orbitals [116]. For the highest incidence angle, the separation of the two peaks decreases and the higher energetic one can only be seen as a shoulder. It should be noted that similar XMCD curves are found for Fe_3O_4 [128] and in that case they are the superposition of spectra from three different Fe species, one of which couples antiferromagnetically to the other two. Given the broad and mostly textureless XAS spectra of the Fe constituent in the alloy dimer compared to the different strong features in Fe_3O_4 , it can be argued if different adsorption sites are at the root of this observation. Nonetheless, this reinforces the notion that the magnetic coupling in the Fe dimer is complex and that the molecular orbitals give rise to magnetic moments that do not couple rigidly.

Measurements above $\theta = 15^\circ$ also reveal a very large L_2 edge, compared to the almost vanishing contribution for lower incidence angles. This reveals a strong spin imbalance in the corresponding orbitals, matching the results of Gutsev *et al.*, where two antibinding minority spin orbitals directly centered on the Fe atom were found in contrast to only one majority spin orbital. Looking at the sum rules (2.2.12), it can be seen that the area under the L_2 edge of the XMCD affects the orbital moment twice as much as it does the spin moment, and in the opposite direction. One would thus expect the spin moment to increase for these angles and the orbital moment to decrease and pass 0, in light of the weakened L_3 edge.

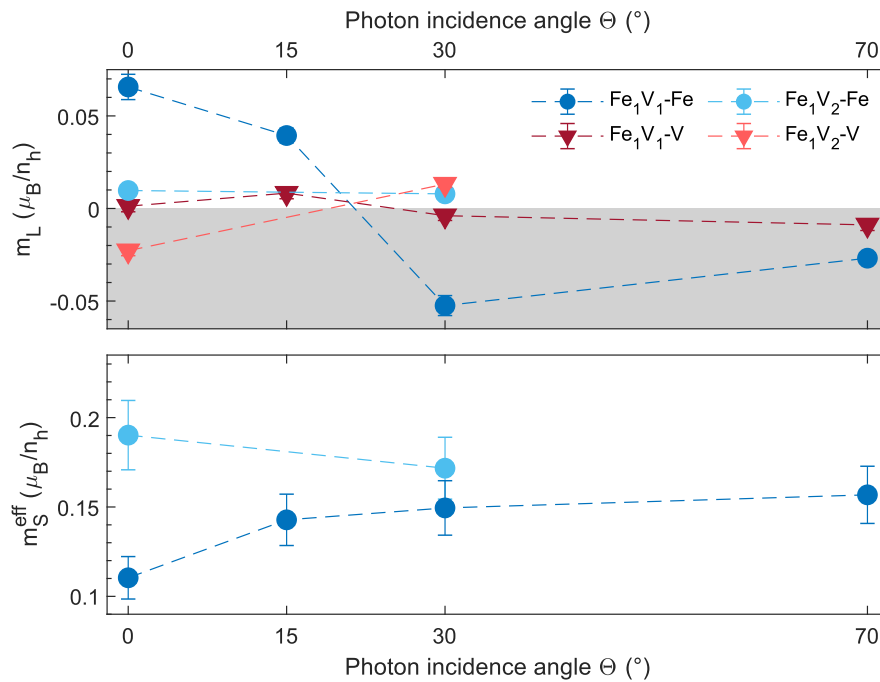


Fig. 4.16.: (Top) Orbital magnetic moments, obtained via the sum rules, for all of the XMCD signals of Fe_1V_1 and Fe_1V_2 (cf. Fig. 4.13 and Fig. 4.17) as a function of the photon incidence angle θ . The Fe and V moments are marked with circles and triangles respectively. (Lower) effective spin magnetic moments for the Fe constituents of the dimer and trimer.

From the extracted orbital and spin moments (cf. Fig. 4.16) one can see that for normal

incidence, the antiferromagnetic alignment of the constituents' total magnetic moments does not translate into an opposing sign of the orbital moments. This has also been found for $\text{Fe}_{0.9}\text{V}_{0.1}$ alloys [84] and shows once again, that the majority of the magnetization of V stems from the spin moment, as was the case for both V_2 and V_3 . The asymmetric lineshape of the XMCD signal, in combination with the multipole moment analysis results of van der Laan *et al.* [89], further solidifies this point. The strong spin moment is likely also the reason for the spectral feature at 516.9 eV, that has been associated with a high spin configuration in the pure V dimer. For $\theta \geq 30^\circ$ the sign of the orbital magnetic moments of both atoms becomes negative, opposing the spin moment for Fe. For V, this could imply that the orbital moment has now aligned with the spin moment. However, the drastically changed XMCD shape can be viewed through the lens of multipole moment analysis and attributed to a loss of spin moment. The switch in the V XMCD would then also be accompanied by the orbital moment becoming the dominant component to the magnetization, but without direct access to the spin information, all of this is speculative. For Fe, this change was expected from the large increase in the XMCD curve's L_2 area and shows that the spin magnetic moment does not couple directly to the geometry of the system but rather only experiences the influence of the surface through the spin-orbit interaction. Therefore, the spin moment of Fe is less influenced by the proximity of V and does not appear to change coupling at increased angles. Rather, the spin moment's angular evolution consists of a monotonic increase alongside θ . The magnitude of m_L/m_S^{eff} is 0.59 ± 0.06 for $\theta = 0^\circ$ and only decreases for larger values of θ (obviously the ratio changes sign for $\theta \geq 30^\circ$). For the XMCD signal, this dominance of the spin moment also obscures the antiparallel orientation of the Fe orbital and spin moments at higher incidence angles, since the main component to the total magnetic moment is always the spin, which never changes coupling with respect to the external field.

4.3.2. Fe_1V_2

Due to unforeseen problems with the measurement setup during the beamtime, it was not possible to record spectra of the Fe_1V_2 trimer at the most extreme incidence angle and therefore only results on $\theta = 0^\circ, 30^\circ$ are reported. These can be found in Fig. 4.17.

While for all of the other adsorbates the question on the preferred structure at the surface comes down to determining the lowest energy adsorption sites, the mixed trimer shows another degree of variability. There is the possibility that Fe either lies between the two V atoms, i.e. it occupies the nearest neighbour position to both of them, or it occupies one of the end positions of the adsorbed cluster, with its distance to one of the V atoms being larger than to the other. This is illustrated in Fig. 4.18, where starting from the optimized structure of the free trimer found by Shan *et al.* one of the two possible adsorption structures is attained [129]. The choice to only focus on the compact trimer in the figure comes one the one hand from the close proximity to the structure from [129] and on the other hand from theoretical results, showing that compact triangular arrangements are energetically favorable for Cr_3 on $\text{Fe}(3\text{ ML})/\text{Cu}(001)$ [123] as well as for V_3 on $\text{Cu}(111)$ [133]. Even though it is difficult to say which of the two possible geometries is favorable without explicit calculations, the longer bond length of 2.581 Å between one of the V atoms and Fe in the free trimer matches the nearest neighbour distance on the Cu surface very well. This would imply that only the shorter V-Fe bond and the

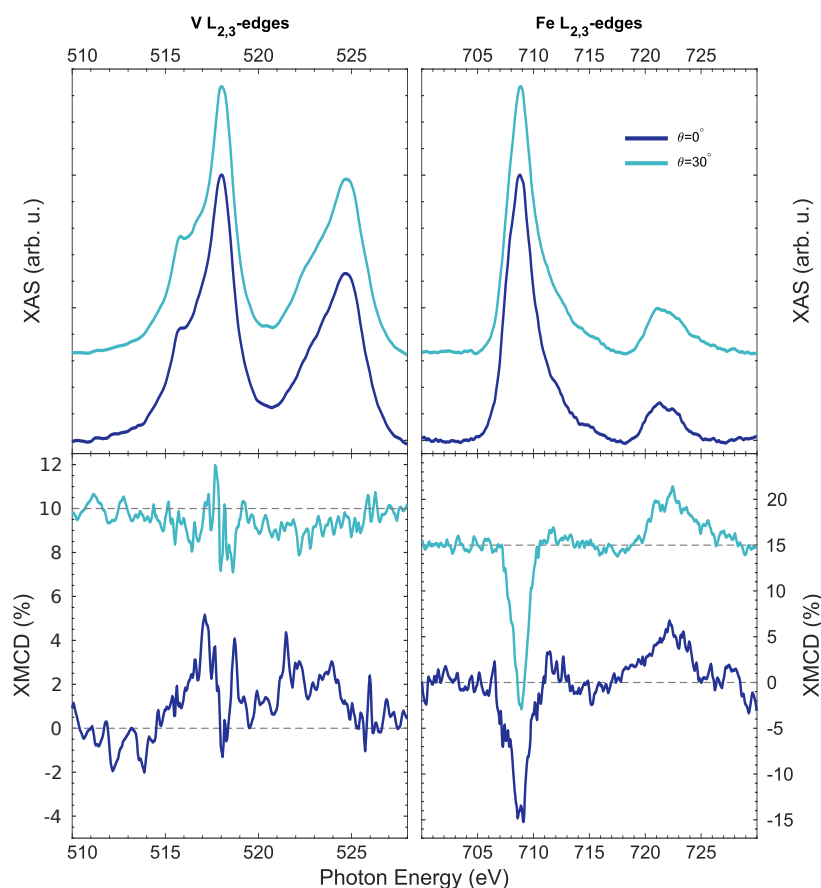


Fig. 4.17.: (Top) Background subtracted white line spectra for the Fe $L_{2,3}$ edges (right) and the V $L_{2,3}$ edges (left) of the Fe_1V_2 trimer, taken at different values of θ . (Bottom) XMCD spectra in a ± 7 T field, corresponding to the top row. All spectra have been normalized to the L_3 peak of their respective white line and vertically offset for better clarity.

V-V bond would have to accommodate to the surface in the case of the lower, more symmetric structure, whereas for the upper structure all three bonds would have to stretch, potentially resulting in a larger energy increase. It is therefore reasonable that the trimer adopts the more symmetric structure with the Fe atom at the corner of the right triangle (i.e. the lower one in Fig. 4.18).

The Fe_1V_2 trimer can be conceptualized mainly in two different ways, depending on which atoms are grouped together and what it should be compared to. One such way would be to view it as a V_2 dimer with an added Fe atom, in which case it would make sense to compare it to V_2 and V_3 , where instead of an Fe atom another V was added. Using the main multiplet feature at ~ 515.9 eV as a means of comparison, it is found that addition of a Fe atom to the V_2 dimer reduces the intensity of this feature, indicating a stronger delocalization of the $3d$ electrons on the V atoms. This points towards the formation of binding orbitals between the V atoms and Fe. This effect is however less pronounced than for the pure V_3 trimer, where both delocalization and hence suppression of the multiplet feature are clearer. This mirrors the behaviour in the

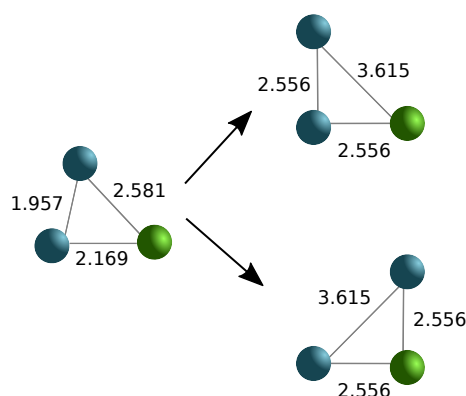


Fig. 4.18.: Schematic showing the emergence of two different adsorption geometries of the compact Fe_1V_2 cluster. Fe is depicted in green and V in blue. The structure of the free cluster on the left was taken from [129]. The two structures on the right derive from the compact adsorption geometry on a $\text{Cu}(001)$ surface. The indicated numbers give the bond lengths in Å.

dimers, where the combination of a Fe atom and a V atom led to a weaker spectral broadening in the alloy dimer as for pure V_2 and just as for the Fe_1V_1 dimer, an explanation for this would be the higher effective nuclear charge on the Fe atom reducing the radial spread of the wavefunction, leading to a lesser degree of delocalization of the valence electrons than a V atom does.

From the point of view of the Fe atom, the addition of a V dimer leads to a significant loss of multiplet features, seen in the corresponding Fe white line. The lower energetic shoulder of the L_3 peak is reduced below visibility and for the L_2 edge the higher energetic feature is barely noticeable (compare Fig. 4.1). However, visibility of this feature is still better than for the alloy dimer, which would imply that the delocalization is not as strong here as it was for the dimer. This is intriguing in that one would expect that presence of molecular orbitals encompassing the complete trimer would lead to more delocalized electrons. A possible explanation would be that the bonding between Fe and V in the trimer is considerably weaker than between the V atoms themselves. The Fe $3d$ -orbitals would then contribute less to the molecular orbitals of the trimer and would be more strongly localized on the Fe atom.

Given the branching ratio obtained from the V white line of the alloy trimer, it appears that the increase of the branching ratio of V_3 trimer with respect to V_2 could be more than a statistical anomaly since upon addition of the Fe atom, the branching ratio of V goes from 0.54 ± 0.03 to 0.56 ± 0.03 . It is not clear why this should happen, given that before, the branching tended to drop upon increasing the adsorbate size. The apparent spin-orbit splitting of the V edges (cf. Tab. 4.8) increases alongside the branching ratio and can thus not help to explain this observation either, as these two values would typically be inversely proportional to each other [35].

For the Fe atom on the other hand, the branching ratio increases significantly to 0.86 ± 0.04 , attaining the highest value of all the Fe constituents in this work. The assumed lower participation of the Fe atomic orbitals in the molecular orbitals would not suffice to explain this strong increase, especially not since the delocalization in the alloy trimer is still larger than for the

pure Fe adatom, which would on the contrary give a lowered branching ratio in the trimer case. Rather, it is possible that the increased branching ratio in relation to the adatom stems from the lowered spin-orbit splitting (compare the 12.5 ± 0.25 eV for the trimer to 13.5 ± 0.25 eV for the adatom) as such a lowering is generally associated with an increased branching ratio [35, 37, 85]. Another possibility is that Fe is present in a mostly d^8 configuration in the trimer leading to a generally higher branching ratio, as has been shown in the seminal work of Thole *et al.* [35]. While the density functional calculations performed by Shan *et al.* on free Fe_1V_2 alloys reveal a Mulliken charge of 6.792 in the $3d$ orbitals of Fe, which does not match the assumption of a d^8 [129], these results do however not take into account that the elongation of the trimer bonds in the adsorption process can favor electronic structures with higher spins, as has been found theoretically for both Fe and V dimers [102, 110] making a d^8 configuration at least plausible.

Thinking of Fe_1V_2 as a Fe_1V_1 with an added V atom on the other hand, one sees that the feature at ~ 517 eV for V vanishes almost completely. This feature was associated with a possible high spin configuration in the previous V species and so its absence would be indicative of the absence of such a high spin state. This matches the findings of Shan *et al.*, where the spin populations of the V atoms in the free trimer were opposite and almost equal in magnitude [129], nearly cancelling out. Such a situation could not be resolved in XAS and would present itself as a low spin state. Looking at the branching ratios of V in the two alloy clusters, there is a slight decrease for the trimer, which can be explained by the improved overlap of the V constituents and the subsequent stronger delocalization of valence electrons and, finally, better dynamic screening of the valence electron-core hole interaction. This is similar to the case in the pure V adsorbates.

For the Fe constituent, the comparison of the alloy dimer and trimer has already been done briefly in a preceding paragraph but focussing on the branching ratios, one sees that the increase in going from the alloy dimer to the alloy trimer is even larger than in comparing the adatom to the alloy trimer. At the same time, the apparent spin-orbit splitting is decreasing only slightly after the addition of a second V atom. Therefore, it is unlikely that the large value of the Fe branching ratio in the trimer is only a result of the lowered spin-orbit splitting but that there is another factor at play. In 4.3.1, a tentative explanation was given in for the low branching ratio in comparison to the spin-orbit splitting. The strong overlap of the Fe and V orbitals in that case could have led to a lowered branching ratio. Considering that this overlap seems to be weakened in the trimer case, as seen for example by the multiplet features in the white line, one would expect the branching ratio to increase. This effect of the reduced spread has also been shown for the pure Fe adsorbates, in that the branching ratio lowered for increasing cluster size. Another possibility would be that there is increased d -electron occupation in the Fe atom. Nevertheless, the upwards energy shift of the L_3 peak between Fe_1V_1 and Fe_1V_2 shows that Fe becomes more akin to the adatom as a possible result of the overlap between the V atoms being better than between the different elements.

In increasing the incidence angle of the synchrotron beam, the V edges show small changes, mainly in that the features before the main peaks become more apparent, signalling a stronger contribution from out-of-plane orbitals. For Fe, the biggest change lies in the L_3 peak itself, where a weak shoulder at normal incidence vanishes completely for $\theta = 30^\circ$. Considering that a feature in the XAS signal arises from excitation into a particular orbital one can state that, in combination with the changes in the V signal, this signifies that the molecular orbitals of the

Adsorbate	B	Edges	E(L_3) (eV)	ΔE_{2p} (eV)
Fe ₁ V ₂	Fe $L_{2,3}$	0.86 ± 0.04	708.8	12.5 ± 0.25
	V $L_{2,3}$	0.56 ± 0.03	518.0	6.7 ± 0.25

Tab. 4.8.: Branching ratios (B), L_3 peak positions and energetic separation between the two L -edges (ΔE_{2p}) for Fe₁V₂/Cu(001), extracted from the white line spectra at $\theta = 0^\circ$ in Fig. 4.17. All other incidence angles are omitted, as the values are isotropic. The values for both constituents are listed separately.

trimer have a stronger Fe contribution at normal incidence, whereas at elevated angles, the Fe orbitals are mostly centered on the Fe atom itself.

Moving on to the XMCD spectra in the lower panels of Fig. 4.17 it firstly becomes obvious that the signal for V is weaker than it was for example for the alloy dimer. In the work of Shan *et al.*, the free Fe₁V₂ trimer was found to have a larger magnetic moment than the corresponding dimer ($4 \mu_B$ vs. $1 \mu_B$) which does however not originate from a higher magnetic moment of the V atoms, as the electronic populations of the two V atoms almost cancel [129]. The weak magnetic signal, as well as the lack of the XAS feature, assumed to be a result of the high spin configuration, can both be seen as results of this antiferromagnetic coupling of the respective V atoms' magnetic moments. The average of the two magnetic contributions, probed by the XMCD spectra, would therefore present as a weak, if not vanishing, magnetic signal at the V edges. While the alloy dimer showed a clearly asymmetric XMCD lineshape at normal incidence, this is not the case here and it is therefore difficult to assign the observed magnetic signal to the spin imbalance in the $3d$ orbitals of V. Looking at the magnetic moments of the trimer gained from the use of the sum rules (cf. Fig. 4.16), rather an orbital moment can be found, which could imply that the observed weak magnetism in the V constituents of the trimer is due to orbital imbalance rather than spin.

The Fe XMCD shows a strength similar to the adatom, albeit with a broader linewidth at the L_3 peak specifically. In combination with the slight shoulder in the XAS peak, this broadening of the XMCD peak can indicate the existence of a mostly in-plane, magnetic orbital. Furthermore, just as the pure adatom, Fe in the trimer also presents the positive overshoot after the main L_3 peak, with its root surmised to be spin polarization in the $3d$ orbitals [89]. The results of Shan *et al.*, finding a spin polarization of 41 % in the d -orbitals [129], support this. A notable difference between the adatom and the alloy trimer however comes in the form of the L_2 peak of the XMCD signal in the Fe constituent of Fe₁V₂, which is extremely large while the XAS contribution of the same peak is rather small. While this points towards a strong spin polarization in the corresponding $3d$ orbitals, it is not clear why the discrepancy is so pronounced for the L_2 but not the L_3 peak.

Comparing the overall shapes of the V and Fe XMCD would lead to conclude an antiferromagnetic alignment of the magnetic moments of the constituents. However, the weak signal at the V edges casts doubt on the validity of this finding and the calculations in [129] would favor a parallel alignment of the Fe and V magnetic moments. In the absence of calculations on the actual adsorbed trimer systems, it is yet possible that the changed geometry leads to an antiferromagnetic alignment between the Fe magnetic moment and the resulting sum of the V

magnetic moments.

Application of the sum rules shows that the orbital contribution to the magnetic moment of Fe is close to zero. This quenching of the orbital magnetic moment can be attributed to the reduction of symmetry brought about by the two neighbouring V atoms, in a similar fashion as in the pure Fe trimer compared to the Fe adatom. However, the reduction is far more pronounced in this case even though in both cases the resulting symmetry on the surface would be C_s for the compact trimers, indicating that there is another effect at play here. Furthermore, the spin magnetic moment of Fe in this trimer has the highest value of any Fe containing species in this work. Considering that d^n configurations with $n > 5$ necessarily have electrons with antiparallel spins and that this creates a trend of decreasing total spin in the corresponding d -shell with higher d -count, this would point towards a lowered d occupation compared to e.g. the free adatom. This does however not match that the spin polarization in the d -orbitals, seen as the positive XMCD region after the L_3 edge, is smaller than it was for example for the alloy dimer. A lowered d -shell occupation would be expected to increase the spin imbalance, seeing as for d^5 there is possibility that all d -orbitals are singly occupied with parallel spins, maximizing both overall spin and spin imbalance. Also, a lowered d -count goes partly against the high branching ratio obtained from the analysis of the XAS, which would rather attribute a d^8 configuration to the Fe atom and can not easily be explained in the case of a lowered d -orbital occupation.

At $\theta = 30^\circ$, the V XMCD would suggest that once again the magnetic moment of V changes its orientation with respect to the magnetic field, which might indicate a non-collinear arrangement of the separate magnetic moments of the trimer (cf. 4.3.1). Additionally, the orbital magnetic moment of the V atoms in the trimer shows the same sign change with increased angle, bolstering this hypothesis. A clear statement regarding this noncollinearity is however difficult, not only because of the weak overall signal, becoming even weaker at this higher incidence angle, but also because such claims can not be made solely on the sign of the XMCD signal alone, as was shown for the V_3 trimer (cf. 4.1.2). It is also worth noting that for the alloy dimer, the orbital magnetic moments of the V and Fe constituents presented the same sign over the whole range of measurement angles, which is not the case for the present trimer and could imply that there is no non-collinear coupling. As there have been so far no other XMCD measurements on systems exhibiting such a possible non-collinear coupling, there is a lack of clear signs either for or against the hypothesis of noncollinearity in this case. While the two magnetic sublattice model helped to clear up the behaviour of the magnetic moments in the case of the Fe_1V_1 dimer, the assumption that all magnetic moments of a given sublattice are coupled rigidly is not necessarily valid here. Rather, it is possible that the V magnetic moments exhibit a noncollinearity between themselves as well as to the Fe atom and that the particular angles are not constant in changing the orientation of the external magnetic field. Such a behaviour has been observed theoretically for transition metal trimers on Cu(111) [133, 134] and on Fe(3 ML)/Cu(001) [123]. Obviously, more sophisticated theoretical methods are needed to answer these questions, yet this is beyond the scope of this thesis.

In comparison to the alloy dimer, the angular evolution of the Fe XMCD in the trimer is considerably less drastic. The strongly visible shoulders at the L_3 edge in normal incidence vanish almost completely, indicating that the orbitals giving rise to these magnetic moments are possibly oriented out-of-plane and have only little contribution at higher angles. This reflects the evolution of the shoulder in the white line. Furthermore, the strength of the positive overshoot

after the L_3 peak decreases for the higher incidence angle which could in turn signify that the Fe orbitals that give rise to these magnetic moments are more evenly occupied with spin up and spin down electrons. The decrease in the effective spin moment of the Fe constituent (cf. Fig. 4.16) supports this interpretation. It would be interesting to see if this trend continues for $\theta = 70^\circ$. While from the height of the XMCD peaks alone, one could conclude that the easy axis of the Fe magnetization lies more in-plane. From the calculated magnetic moments, it is however obvious that the spin moment decreases significantly for higher incidence angle and that the orbital moment can at least not offset this decrease, leading to an overall lower magnetic moment at $\theta = 30^\circ$ and signifying a preferred out-of-plane easy axis.

In contrast to the alloy dimer, there is up until $\theta = 30^\circ$ no sign of a strong peak splitting, which shows that the strongly different coupling situations for the different Fe orbitals, assumed in the case of the dimer, are not given here.

5. Summary and Perspective

This thesis set out to investigate the electronic and magnetic properties of small $3d$ adsorbates on non-magnetic surfaces. Since that is a wide scope, it was narrowed down by focusing on Cu(001) surfaces and Fe_mV_n adsorbates where $m+n \leq 3$. The investigation of these adsorbates was done by performing X-ray absorption measurements across the $L_{2,3}$ edges of Fe and V. This way, information could be gathered about the $3d$ states of the adsorbates in an element specific manner, allowing a fundamental view into these systems and possible comparison to theoretical calculations. Changing the photon angle of incidence on the sample made it possible to discern the contributions of orbitals that lie either parallel or antiparallel to the sample surface.

Comparison of the pure $\text{Fe}_{1,2,3}$ adsorbates showed, that the current setup does indeed produce adsorbates of well-defined sizes in this atomic size regime and that their respective properties differed quite a bit. As a first result, multiplet features were found in the absorption spectra of the adsorbates. In earlier experiments on size-selected adsorbates, the use of strongly interacting Ni surfaces inhibited these features, which are indicative of an electronic structure closer to the atomic case than the bulk. For all of the adsorbates, a large branching ratio was found, suggesting that all three of them are in a high spin ground state, in accordance with Hund's rules. A striking example of the fluctuating nature of cluster properties with size was found in the anisotropy of the adsorbates' magnetic moments. While Fe_1 showed a strong tendency to have its magnetic moment aligned in-plane with the substrate surface, this became much weaker in the case of Fe_2 and already for Fe_3 the magnetization became strongly out-of-plane. A very simple model of the electrostatic field of the crystal substrate and its influence on the electrons of Fe_1 was established to explain this anisotropy and for Fe_2 a qualitative explanation based on symmetry arguments was given. This behaviour was also compared to the well-documented evolution of the magnetic anisotropy in thin films of Fe on Cu(001), where the anisotropy is in-plane for thin layers and becomes out-of-plane after a certain thickness. As the gap between these samples in the monolayer thickness range and the present data is quite significant, it would be interesting to investigate larger clusters of adsorbed Fe and see if the trend of an out-of-plane magnetic easy axis remains for long.

For the pure V_1 adatom, a similar in-plane magnetic anisotropy to the Fe adatom was found and could be rationalized in a similar way due to the crystal field. Also, the branching ratio of the V adatom was close to the statistical case, which matches the results on free clusters. This was explained via two competing effects cancelling. For V_2 , a strongly anisotropic absorption signal was found, where at shallow incidence angles the multiplet features disappeared almost entirely and the spectra appeared bulk like. This was accompanied by a mostly in-plane magnetization where a separate evaluation of the orbital magnetic moment showed a change in alignment to the external field and to the spin moment. Considering Hund's rules, an antiparallel alignment of orbital and spin magnetic moment appears plausible and by invoking the basic shapes of dimer molecular orbitals an argument for the origin of the angular dependence could be made.

For the V_3 adsorbate, the main result is a switch of the total magnetic moment with increasing incidence angle. While this could be an indicator for a possible non-collinear arrangement of the trimer's magnetic moments, so far this could however not be proven beyond doubt. Dedicated theoretical efforts could probably clear this up, which is why this should be pursued in the near future. It was however determined that the alignment of the trimer's magnetic moments shows a complex dependence on the external magnetic field.

The Fe_1V_1 dimer adsorbate once again confirmed that, in the realm of quantum mechanics, the whole has tendency to be more than the sum of its parts. Not only did the multiplet features of both materials mostly vanish, this didn't happen symmetrically for Fe and V. Rather the effect on Fe was far stronger, resulting in bulk like features whereas for V, the spectra showed stronger multiplet features than in the case of the dimer. An explanation for this was given via the strong delocalization of the molecular wavefunction caused by the weaker ionic charge on the V atom compared to the Fe atom. This led to the orbitals being more spread out than they would for Fe_2 but less so than they would for V_2 . An even more important result, possibly the single most important one of this work, was the sign change of the V XMCD signal at higher incidence angles. In contrast to the situation in V_3 , here the Fe atom could be used to make clear statements about the direction of the V magnetic moment. It was concluded that the reason for this change lies in a non-collinear arrangement of magnetic moments between both atoms, resulting from a spin flop phase. Numerical minimization of the energy of a theoretical model, based on two magnetic sublattices of a material with negative exchange interaction, was used to find a range of anisotropy and exchange constants that would explain the experimental results. By fitting these constants to the observations, the canting angles of the individual magnetic moments could be determined. This marks the first time that such an effect could be observed on this size scale.

For the Fe_1V_2 trimer, a similar sign change in the V XMCD could be seen. However, problems during the measurements as well as the failure of the simple model for the spin flop made it impossible to conclusively tie this to a spin flop phase. This was also complicated by the fact that for an alloy trimer on a fourfold symmetric surface, there exist twice as many possible adsorption geometries, which has a large influence on the electronic structure. Yet, it was hypothesized that the magnetic moments of both V atoms in the trimer would be coupled antiferromagnetically and that the magnetic moment of Fe was largely that of an adatom, where however the orbital magnetic moment was largely quenched. Considering the possible spin flop phase encountered in the alloy trimer, it would be certainly interesting to check if the evolution of the orientation of the magnetic moments continues for higher incidence angles. Measurements on Fe_2V_1 would also be of interest to gauge if this non-collinearity of the magnetic moments remains in the case that there are more Fe magnetic moments than V. Going to even larger alloy clusters, together with more in-depth theoretical calculations, could give valuable insight into the complex interplay of competing interactions at the atomic scale, in this case exchange interaction and magnetocrystalline anisotropy.

As a side effect of the newly introduced "On the fly" measurement procedure, a photon induced change in the spectra of e.g. adatoms and adsorbed dimers could be observed. Taking inspiration from measurements on metallorganic complexes, this was identified as a spin crossover effect, where the energy of the soft X-rays helped the system to overcome the barrier between two separate states in the crystal field of the surface. Using a simple kinetic model, the

time dependence of this transition could be explained in a somewhat satisfying manner, showing that the changes happen on a scale of 30–120 s. As this was not anticipated, the measurements on this were however scarce and in the future, it would be interesting to focus more intently on this to clear up if this is indeed a spin crossover transition, if the final states reached were stable or excited states that would revert back to a ground state and if this effect persists for larger adsorbates. To this end, it would be helpful to fit the measured spectra as the sum of pure initial and final state, where the initial state could possibly be investigated more in detail with the use of lower photon flux.

3.2.1 showed that the cooling power of the sample setup can be improved and it will be interesting to see if the early results with the new cryostat translate to a lower base temperature of the sample. This would put the experiment within reach of achieving magnetic saturation even for dilute samples and greatly improve the reproducibility and comparability of this setup's results.

The ability to perform hysteresis measurements on the samples in the HFK would be a welcome addition. With the OTF mode of the beamline, this should not prove too difficult once the magnetic field strength of the HFK magnet can reliably be logged during the measurement process.

A. Wigner 3- j symbols

General formulae

Racah has established a general rule to calculate the 3- j symbols [23]:

$$\begin{aligned} \begin{pmatrix} j_1 & j_2 & j_3 \\ m_1 & m_2 & m_3 \end{pmatrix} &= (-1)^{j_1-j_2-m_3} \sqrt{\frac{(j_1+j_2-j_3)!(j_1-j_2+j_3)!(-j_1+j_2+j_3)!}{(j_1+j_2+j_3+1)!}} \times \\ &\times \sqrt{(j_1+m_1)!(j_1-m_1)!(j_2+m_2)!(j_2-m_2)!(j_3+m_3)!(j_3-m_3)!} \times \\ &\times \sum_t \frac{(-1)^t}{x} \end{aligned} \quad (\text{A.1})$$

where

$$x = t!(j_3 - j_2 + m_1 + t)!(j_3 - j_1 - m_2 + t)!(j_1 + j_2 - j_3 - t)!(j_1 - m_1 - t)!(j_2 + m_2 - t)! \quad (\text{A.2})$$

And the sum extends over all t for which none of the factorials involving t have nonnegative arguments. From this, it follows that the symbols vanish unless the following conditions hold:

$$\begin{aligned} m_i &\in \{-j_i, -j_i + 1, \dots, j_i - 1, j_i\} \quad \forall i \\ m_1 + m_2 + m_3 &= 0 \\ |j_1 - j_2| &\leq j_3 \leq j_1 + j_2 \\ (j_1 + j_2 + j_3) &\text{ is an integer} \\ (j_1 + j_2 + j_3) &\text{ is an even integer if } m_1 = m_2 = m_3 = 0 \end{aligned} \quad (\text{A.3})$$

Evaluation for $j_1 = j_3 = 2$

The Wigner 3- j symbols $\begin{pmatrix} 2 & k & 2 \\ -m & q & m' \end{pmatrix}$ that pertain to the crystal field calculations in the present thesis are listed here. The results are grouped by values of k and presented as a matrix for each value of q .

$k = 0$

$$\begin{array}{c} m_l \backslash m'_l \\ -2 \\ -1 \\ 0 \\ 1 \\ 2 \end{array} \begin{array}{c} \left(\begin{array}{ccc} 2 & 0 & 2 \\ -m_l & 0 & m'_l \end{array} \right) = \end{array} \begin{array}{c} -2 \quad -1 \quad 0 \quad 1 \quad 2 \\ \left(\begin{array}{ccccc} \frac{1}{\sqrt{5}} & 0 & 0 & 0 & 0 \\ 0 & \frac{1}{\sqrt{5}} & 0 & 0 & 0 \\ 0 & 0 & \frac{1}{\sqrt{5}} & 0 & 0 \\ 0 & 0 & 0 & \frac{1}{\sqrt{5}} & 0 \\ 0 & 0 & 0 & 0 & \frac{1}{\sqrt{5}} \end{array} \right) \end{array} \quad (\text{A.1})$$

$k = 2$

$$\begin{array}{c} m_l \backslash m'_l \\ -2 \\ -1 \\ 0 \\ 1 \\ 2 \end{array} \begin{array}{c} \left(\begin{array}{ccc} 2 & 2 & 2 \\ -m_l & 0 & m'_l \end{array} \right) = \end{array} \begin{array}{c} -2 \quad -1 \quad 0 \quad 1 \quad 2 \\ \left(\begin{array}{ccccc} \sqrt{\frac{2}{35}} & 0 & 0 & 0 & 0 \\ 0 & \frac{1}{\sqrt{70}} & 0 & 0 & 0 \\ 0 & 0 & -\sqrt{\frac{2}{35}} & 0 & 0 \\ 0 & 0 & 0 & \frac{1}{\sqrt{70}} & 0 \\ 0 & 0 & 0 & 0 & \sqrt{\frac{2}{35}} \end{array} \right) \end{array} \quad (\text{A.2})$$

$k = 4$

$$\begin{array}{c} m_l \backslash m'_l \\ -2 \\ -1 \\ 0 \\ 1 \\ 2 \end{array} \begin{array}{c} \left(\begin{array}{ccc} 2 & 4 & 2 \\ -m_l & -4 & m'_l \end{array} \right) = \end{array} \begin{array}{c} -2 \quad -1 \quad 0 \quad 1 \quad 2 \\ \left(\begin{array}{ccccc} 0 & 0 & 0 & 0 & 1/3 \\ 0 & 0 & 0 & 0 & 0 \\ 0 & 0 & 0 & 0 & 0 \\ 0 & 0 & 0 & 0 & 0 \\ 0 & 0 & 0 & 0 & 0 \end{array} \right) \end{array} \quad (\text{A.3})$$

$$\begin{array}{c} m_l \backslash m'_l \\ -2 \\ -1 \\ 0 \\ 1 \\ 2 \end{array} \begin{array}{c} \left(\begin{array}{ccc} 2 & 4 & 2 \\ -m_l & 0 & m'_l \end{array} \right) = \end{array} \begin{array}{c} -2 \quad -1 \quad 0 \quad 1 \quad 2 \\ \left(\begin{array}{ccccc} \frac{1}{3\sqrt{70}} & 0 & 0 & 0 & 0 \\ 0 & \frac{2}{3}\sqrt{\frac{2}{35}} & 0 & 0 & 0 \\ 0 & 0 & \sqrt{\frac{2}{35}} & 0 & 0 \\ 0 & 0 & 0 & \frac{2}{3}\sqrt{\frac{2}{35}} & 0 \\ 0 & 0 & 0 & 0 & \frac{1}{3\sqrt{70}} \end{array} \right) \end{array} \quad (\text{A.4})$$

$$\begin{array}{c} m_l \backslash m'_l \\ -2 \\ -1 \\ 0 \\ 1 \\ 2 \end{array} \begin{array}{c} \left(\begin{array}{ccc} 2 & 4 & 2 \\ -m_l & 4 & m'_l \end{array} \right) = \end{array} \begin{array}{c} -2 \quad -1 \quad 0 \quad 1 \quad 2 \\ \left(\begin{array}{ccccc} 0 & 0 & 0 & 0 & 0 \\ 0 & 0 & 0 & 0 & 0 \\ 0 & 0 & 0 & 0 & 0 \\ 0 & 0 & 0 & 0 & 0 \\ 1/3 & 0 & 0 & 0 & 0 \end{array} \right) \end{array} \quad (\text{A.5})$$

Bibliography

- [1] J. Jortner, “Cluster size effects”, *Z. Phys. D—Atoms, Molecules and Clusters* **24**, 247–275 (1992) <https://doi.org/10.1007/BF01425749>.
- [2] J. T. Lau, J. Rittmann, V. Zamudio-Bayer, M. Vogel, K. Hirsch, P. Klar, F. Lofink, T. Möller, and B. v. Issendorff, “Size dependence of $L_{2,3}$ branching ratio and $2p$ core-hole screening in x-ray absorption of metal clusters”, *Phys. Rev. Lett.* **101**, 153401 (2008) <https://link.aps.org/doi/10.1103/PhysRevLett.101.153401>.
- [3] H. Brune and P. Gambardella, “Magnetism of individual atoms adsorbed on surfaces”, *Surf. Sci.* **603**, 1812–1830 (2009) <https://doi.org/10.1016/j.susc.2008.11.055>.
- [4] F. Donati, S. Rusponi, S. Stepanow, C. Wäckerlin, A. Singha, L. Persichetti, R. Baltic, K. Diller, F. Patthey, E. Fernandes, J. Dreiser, Ž. Šljivančanin, K. Kummer, C. Nistor, P. Gambardella, and H. Brune, “Magnetic remanence in single atoms”, *Science* **352**, 318–321 (2016) <https://www.science.org/doi/abs/10.1126/science.aad9898>.
- [5] J. Stöhr, “X-ray magnetic circular dichroism spectroscopy of transition metal thin films”, *J. Electron Spec. Relat. Phenom.* **75**, 253–272 (1995) [https://doi.org/10.1016/0368-2048\(95\)02537-5](https://doi.org/10.1016/0368-2048(95)02537-5).
- [6] S. M. Dubiel and J. Cieślak, “Sigma-phase in Fe-Cr and Fe-V alloy systems and its physical properties”, *Critical Reviews in Solid State and Materials Sciences* **36**, 191–208 (2011) <https://doi.org/10.1080/10408436.2011.589232>.
- [7] R. Barco, P. Pureur, G. L. F. Fraga., and S. M. Dubiel, “Extended scaling in the magnetic critical phenomenology of the σ -phase Fe_{0.53}–Cr_{0.47} and Fe_{0.52}–V_{0.48} alloys”, *J. Phys.: Condens. Matter* **24**, 046002 (2012) <https://doi.org/10.1088/0953-8984/24/4/046002>.
- [8] J. R. Smith, J. G. Gay, and F. J. Arlinghaus, “Self-consistent local-orbital method for calculating surface electronic structure: application to Cu (100)”, *Phys. Rev. B* **21**, 2201–2221 (1980) <https://doi.org/10.1103/PhysRevB.21.2201>.
- [9] G. E. Pacchioni, L. Gragnaniello, F. Donati, M. Pivetta, G. Autès, O. V. Yazyev, S. Rusponi, and H. Brune, “Multiplet features and magnetic properties of Fe on Cu(111): from single atoms to small clusters”, *Phys. Rev. B* **91**, 235426 (2015) <https://doi.org/10.1103/PhysRevB.91.235426>.
- [10] B. T. Thole, P. Carra, F. Sette, and G. van der Laan, “X-ray circular dichroism as a probe of orbital magnetization”, *Phys. Rev. Lett.* **68**, 1943–1946 (1992) <https://doi.org/10.1103/PhysRevLett.68.1943>.

- [11] P. Carra, B. Thole, M. Altarelli, and X. Wang, “X-ray circular dichroism and local magnetic fields”, *Phys. Rev. Lett.* **70**, 694–697 (1993) <https://doi.org/10.1103/PhysRevLett.70.694>.
- [12] J. Stöhr and H. Siegmann, *Magnetism: From Fundamentals to Nanoscale Dynamics*, 1st ed., Vol. 152, Springer Series in Solid-State Sciences (Springer-Verlag Berlin Heidelberg, 2006), <https://doi.org/10.1007/978-3-540-30283-4>.
- [13] S. Blundell, *Magnetism in condensed matter*, Oxford Master Series in Condensed Matter Physics (Oxford University Press, 2001).
- [14] J. H. van Vleck, “On the anisotropy of cubic ferromagnetic crystals”, *Phys. Rev.* **52**, 1178–1198 (1937) <https://link.aps.org/doi/10.1103/PhysRev.52.1178>.
- [15] J. M. D. Coey, *Magnetism and magnetic materials*, 1st ed. (Cambridge University Press, 2010), 10.1017/CB09780511845000.
- [16] I. G. Rau, S. Baumann, S. Rusponi, F. Donati, S. Stepanow, L. Gragnaniello, J. Dreiser, C. Piamonteze, F. Nolting, S. Gangopadhyay, O. R. Albertini, R. M. Macfarlane, C. P. Lutz, B. A. Jones, P. Gambardella, A. J. Heinrich, and H. Brune, “Reaching the magnetic anisotropy limit of a 3d metal atom”, *Science* **344**, 988–992 (2014) <https://www.science.org/doi/abs/10.1126/science.1252841>.
- [17] P. Gambardella, S. Rusponi, M. Veronese, S. S. Dhesi, C. Grazioli, A. Dallmeyer, I. Cabria, R. Zeller, P. H. Dederichs, K. Kern, C. Carbone, and H. Brune, “Giant magnetic anisotropy of single cobalt atoms and nanoparticles”, *Science* **300**, 1130–1133 (2003) <https://doi.org/10.1126/science.1082857>.
- [18] G. van der Laan, “Microscopic origin of magnetocrystalline anisotropy in transition metal thin films”, *J. Phys.: Condens. Matter* **10**, 3239–3253 (1998) <https://doi.org/10.1088/0953-8984/10/14/012>.
- [19] R. J. Radwański, “Anisotropic ferrimagnets in high magnetic fields”, *Physica B+C* **142**, 57–64 (1986) [https://doi.org/10.1016/0378-4363\(86\)90225-1](https://doi.org/10.1016/0378-4363(86)90225-1).
- [20] A. C. Thompson, D. Attwood, E. Gullikson, M. Howells, J. B. Kortright, A. L. Robinson, J. H. Underwood, K.-J. Kim, J. Kirz, I. Lindau, P. Pianetta, H. Winick, G. Williams, and J. Scofield, *X-ray Data Booklet* (Lawrence Berkeley National Laboratory, University of California, Berkeley, CA, 2009).
- [21] J. Stöhr, *NEXAFS spectroscopy*, 1st ed., Vol. 25, Springer Series in Surface Sciences (Springer-Verlag Berlin Heidelberg, 1992).
- [22] J. Stöhr and Y. Wu, “X-ray magnetic circular dichroism: basic concepts and theory for 3d transition metal atoms”, in *New directions in research with third-generation soft x-ray synchrotron radiation sources*, edited by A. S. Schlachter and F. J. Wuilleumier (Springer Netherlands, Dordrecht, 1994), pp. 221–250, https://doi.org/10.1007/978-94-011-0868-3_9.
- [23] G. Racah, “Theory of complex spectra. II”, *Phys. Rev.* **62**, 438–462 (1942) <https://doi.org/10.1103/PhysRev.62.438>.

- [24] E. König and S. Kremer, “Irreducible tensor operator methods in intermediate-field coupling”, *Int. J. Quantum Chem.* **8**, 347–362 (1974) <https://doi.org/10.1002/qua.560080304>.
- [25] H. Ebert, “Circular magnetic x-ray dichroism in transition metal systems”, in *Spin—orbit-influenced spectroscopies of magnetic solids*, edited by H. Ebert and G. Schütz (1996), pp. 159–177, <https://doi.org/10.1007/BFb0102347>.
- [26] J. L. Erskine and E. A. Stern, “Calculation of the M_{23} magneto-optical absorption spectrum of ferromagnetic nickel”, *Phys. Rev. B* **12**, 5016–5024 (1975) <https://link.aps.org/doi/10.1103/PhysRevB.12.5016>.
- [27] G. Schütz, W. Wagner, W. Wilhelm, P. Kienle, R. Zeller, R. Frahm, and G. Materlik, “Absorption of circularly polarized x rays in iron”, *Phys. Rev. Lett.* **58**, 737–740 (1987) <https://doi.org/10.1103/PhysRevLett.58.737>.
- [28] C. T. Chen, F. Sette, Y. Ma, and S. Modesti, “Soft-X-ray magnetic circular dichroism at the $L_{2,3}$ edges of nickel”, *Phys. Rev. B* **42**, 7262–7265 (1990) <https://doi.org/10.1103/PhysRevB.42.7262>.
- [29] H. A. Dürr, G. Y. Guo, B. T. Thole, and G. van der Laan, “Magnetocrystalline anisotropy of ultrathin Fe films on Ni(110)”, *J. Phys.: Condens. Matter.* **8**, L111 (1996) <https://doi.org/10.1088/0953-8984/8/8/003>.
- [30] C. Brouder, “Angular dependence of x-ray absorption spectra”, *J. Phys.: Condens. Matter* **2**, 701–738 (1990) <https://doi.org/10.1088/0953-8984/2/3/018>.
- [31] J. Stöhr, “Exploring the microscopic origin of magnetic anisotropies with X-ray magnetic circular dichroism (XMCD) spectroscopy”, *J. Magn. and Magn. Mater.* **200**, 470–497 (1999) [https://doi.org/10.1016/S0304-8853\(99\)00407-2](https://doi.org/10.1016/S0304-8853(99)00407-2).
- [32] B. T. Thole and G. van der Laan, “Linear relation between x-ray absorption branching ratio and valence-band spin-orbit expectation value”, *Phys. Rev. A* **38**, 1943–1947 (1988) <https://link.aps.org/doi/10.1103/PhysRevA.38.1943>.
- [33] J. Fink, T. Müller-Heinzerling, B. Scheerer, W. Speier, F. U. Hillebrecht, J. C. Fuggle, J. Zaanen, and G. A. Sawatzky, “2p absorption spectra of the 3d elements”, *Phys. Rev. B* **32**, 4899–4904 (1985) <https://doi.org/10.1103/PhysRevB.32.4899>.
- [34] J. Zaanen, G. A. Sawatzky, J. Fink, W. Speier, and J. C. Fuggle, “ $L_{2,3}$ absorption spectra of the lighter 3d transition metals”, *Phys. Rev. B* **32**, 4905–4913 (1985) <https://doi.org/10.1103/PhysRevB.32.4905>.
- [35] B. T. Thole and G. van der Laan, “Branching ratio in x-ray absorption spectroscopy”, *Phys. Rev. B* **38**, 3158–3171 (1988) <https://doi.org/10.1103/PhysRevB.38.3158>.
- [36] D. W. Lynch and R. D. Cowan, “Effect of hybridization on $4d \rightarrow 4f$ spectra in light lanthanides”, *Phys. Rev. B* **36**, 9228–9233 (1987) <https://doi.org/10.1103/PhysRevB.36.9228>.

- [37] J. Schwitalla and H. Ebert, “Electron core-hole interaction in the x-ray absorption spectroscopy of $3d$ transition metals”, *Phys. Rev. Lett.* **80**, 4586–4589 (1998) <https://doi.org/10.1103/PhysRevLett.80.4586>.
- [38] A. L. Ankudinov, A. I. Nesvizhskii, and J. J. Rehr, “Dynamic screening effects in x-ray absorption spectra”, *Phys. Rev. B* **67**, 115120 (2003) <https://doi.org/10.1103/PhysRevB.67.115120>.
- [39] P. Rao and J. Waber, “Surface field analysis of splitting of orbitals of atoms and ions approaching a metal surface”, *Surf. Sci.* **28**, 299–320 (1971) [https://doi.org/10.1016/0039-6028\(71\)90101-4](https://doi.org/10.1016/0039-6028(71)90101-4).
- [40] B. C. Carlson and G. S. Rushbrooke, “On the expansion of a Coulomb potential in spherical harmonics”, *Math. Proc. Camb. Philos. Soc.* **46**, 626–633 (1950) <https://doi.org/10.1017/S0305004100026190>.
- [41] Z. Yang and Q. Wei, “On the relations between the crystal field parameter notations in the “Wybourne” notation and the conventional ones for $3d^N$ ions in axial symmetry crystal field”, *Physica B* **370**, 137–145 (2005) <https://doi.org/10.1016/j.physb.2005.09.002>.
- [42] W. Nolting, *Grundkurs Theoretische Physik 5/2: Quantenmechanik - Methoden und Anwendungen*, 6th ed., Springer-Lehrbuch (Springer Berlin Heidelberg New York, 2006).
- [43] K. Bockasten, “Mean values of powers of the radius for hydrogenic electron orbits”, *Phys. Rev. A* **9**, 1087–1089 (1974) <https://doi.org/10.1103/PhysRevA.9.1087>.
- [44] L. Cambi and L. Szegö, “Über die magnetische Suszeptibilität der komplexen Verbindungen”, *Ber. dtsh. Chem. Gesellschaft A/B* **64**, 2591–2598 (1931) <https://doi.org/10.1002/cber.19310641002>.
- [45] P. Atkins and J. de Paula, *Atkins’ physical chemistry*, 8th ed. (W. H. Freeman and Company, 2006).
- [46] J. J. Scepaniak, T. D. Harris, C. S. Vogel, J. Sutter, K. Meyer, and J. M. Smith, “Spin crossover in a four-coordinate Iron(II) complex”, *J. Am. Chem. Soc.* **133**, 3824–3827 (2011) <https://doi.org/10.1021/ja2003473>.
- [47] F. Milocco, F. de Vries, H. S. Siebe, S. Engbers, S. Demeshko, F. Meyer, and E. Otten, “Widening the window of spin-crossover temperatures in Bis(formazanate)iron(II) complexes via steric and noncovalent interactions”, *Inorg. Chem.* **60**, 2045–2055 (2021) <https://doi.org/10.1021/acs.inorgchem.0c03593>.
- [48] L. Cambi and L. Szegö, “Über die magnetische Suszeptibilität der komplexen Verbindungen (II. Mitteil.)”, *Ber. dtsh. Chem. Gesellschaft A/B* **66**, 656–661 (1933) <https://doi.org/10.1002/cber.19330660508>.
- [49] T. Granier, B. Gallois, J. Gaultier, J. A. Real, and J. Zarembowitch, “High-pressure single-crystal x-ray diffraction study of two spin-crossover iron(II) complexes: $\text{Fe}(\text{Phen})_2(\text{NCS})_2$ and $\text{Fe}(\text{Btz})_2(\text{NCS})_2$ ”, *Inorg. Chem.* **32**, 5305–5312 (1993) <https://doi.org/10.1021/ic00075a058>.

- [50] S. Decurtins, P. Gütllich, C. Köhler, H. Spiering, and A. Hauser, “Light-induced excited spin state trapping in a transition-metal complex: the hexa-1-propyltetrazole-iron (II) tetrafluoroborate spin-crossover system”, *Chem. Phys. Lett.* **105**, 1–4 (1984) [https://doi.org/10.1016/0009-2614\(84\)80403-0](https://doi.org/10.1016/0009-2614(84)80403-0).
- [51] D. Collison, C. David Garner, C. M. McGrath, J. Frederick W. Mosselmans, M. D. Roper, J. M. W. Seddon, E. Sinn, and N. A. Young, “Soft X-ray induced excited spin state trapping and soft X-ray photochemistry at the iron $L_{2,3}$ edge in $[\text{Fe}(\text{phen})_2(\text{NCS})_2]$ and $[\text{Fe}(\text{phen})_2(\text{NCSe})_2]$ (phen = 1,10-phenanthroline)”, *J. Chem. Soc., Dalton Trans.*, 4371–4376 (1997) <https://doi.org/10.1039/A703728G>.
- [52] V. Davesne, M. Gruber, T. Miyamachi, V. Da Costa, S. Boukari, F. Scheurer, L. Joly, P. Ohresser, E. Otero, F. Choueikani, A. B. Gaspar, J. A. Real, W. Wulfhekel, M. Bowen, and E. Beaurepaire, “First glimpse of the soft x-ray induced excited spin-state trapping effect dynamics on spin cross-over molecules”, *J. Chem. Phys.* **139**, 074708 (2013) <https://doi.org/10.1063/1.4818603>.
- [53] L. Kipgen, M. Bernien, F. Nickel, H. Naggert, A. J. Britton, L. M. Arruda, E. Schierle, E. Weschke, F. Tuzek, and W. Kuch, “Soft-x-ray-induced spin-state switching of an adsorbed Fe(II) spin-crossover complex”, *J. Phys.: Condens. Matter* **29**, 394003 (2017) <https://doi.org/10.1088/1361-648x/aa7e52>.
- [54] H.-J. Kim, J.-H. Park, and E. Vescovo, “Oxidation of the Fe(110) surface: An $\text{Fe}_3\text{O}_4(111)/\text{Fe}(110)$ bilayer”, *Phys. Rev. B* **61**, 15284–15287 (2000) <https://doi.org/10.1103/PhysRevB.61.15284>.
- [55] H.-U. Ehrke, “Mononumerische Metallcluster: Erzeugung und Röntgenspektroskopische Messungen”, PhD thesis (Technische Universität München, 2000).
- [56] J. T. Lau, A. Achleitner, H.-U. Ehrke, U. Langenbuch, M. Reif, and W. Wurth, “Ultra-high vacuum cluster deposition source for spectroscopy with synchrotron radiation”, *Rev. Sci. Instrum.* **76**, 063902 (2005) <https://doi.org/10.1063/1.1921551>.
- [57] J. T. Lau, A. Föhlisch, R. Nietubyc, M. Reif, and W. Wurth, “Size-dependent magnetism of deposited small iron clusters studied by x-ray magnetic circular dichroism”, *Phys. Rev. Lett.* **89**, 057201 (2002) <https://doi.org/10.1103/PhysRevLett.89.057201>.
- [58] L. Glaser, K. Chen, S. Fiedler, M. Wellhöfer, W. Wurth, and M. Martins, “Magnetic properties of small size-selected Co and CoPt clusters on Ni”, *Phys. Rev. B* **86**, 075435 (2012) <https://doi.org/10.1103/PhysRevB.86.075435>.
- [59] T. Beeck, “Small, size-selected and deposited clusters on magnetic and non-magnetic 3d transition metal surfaces”, PhD thesis (Universität Hamburg, 2015).
- [60] K. Chen, T. Beeck, S. Fiedler, I. Baev, W. Wurth, and M. Martins, “Oxidation-induced spin reorientation in Co adatoms and CoPd dimers on Ni/Cu(100)”, *Phys. Rev. B* **93**, 144421 (2016) <https://doi.org/10.1103/PhysRevB.93.144421>.
- [61] A. Wucher, M. Wahl, and H. Oechsner, “The mass distribution of sputtered metal clusters: I. Experiment”, *Nucl. Instr. and Meth. B* **83**, 73–78 (1993) [https://doi.org/10.1016/0168-583X\(93\)95910-W](https://doi.org/10.1016/0168-583X(93)95910-W).

- [62] S. Schippers et al., “Absolute cross sections for photoionization of Xe^{q+} ions ($1 \leq q \leq 5$) at the 3d ionization threshold”, *J. Phys. B: At. Mol. Opt. Phys.* **47**, 115602 (2014) <https://doi.org/10.1088/0953-4075/47/11/115602>.
- [63] J. T. Lau, W. Wurth, H.-U. Ehrke, and A. Achleitner, “Soft landing of size-selected clusters in rare gas matrices”, *Low Temp. Phys.* **29**, 223–227 (2003) <https://doi.org/10.1063/1.1542443>.
- [64] S. Fedrigo, W. Harbich, and J. Buttet, “Soft landing and fragmentation of small clusters deposited in noble-gas films”, *Phys. Rev. B* **58**, 7428–7433 (1998) <https://doi.org/10.1103/PhysRevB.58.7428>.
- [65] T. T. Tsong, “Experimental studies of the behaviour of single adsorbed atoms on solid surfaces”, *Rep. Prog. Phys.* **51**, 759–832 (1988) <https://doi.org/10.1088/0034-4885/51/6/001>.
- [66] M. Reif, L. Glaser, M. Martins, and W. Wurth, “Size-dependent properties of small deposited chromium clusters by x-ray absorption spectroscopy”, *Phys. Rev. B* **72**, 155405 (2005) <https://doi.org/10.1103/PhysRevB.72.155405>.
- [67] M. Martins, M. Reif, L. Glaser, and W. Wurth, “Magnetic properties of deposited gadolinium atoms, dimers and their monoxides”, *Eur. Phys. J. D* **45**, 539–546 (2007) <https://doi.org/10.1140/epjd/e2007-00255-9>.
- [68] K. Chen, S. Fiedler, I. Baev, T. Beeck, W. Wurth, and M. Martins, “Hybridization and magnetism in small FePt alloy clusters”, *New J. Phys.* **14**, 123005 (2012) <https://doi.org/10.1088/1367-2630/14/12/123005>.
- [69] T. Beeck, I. Baev, S. Gieschen, H. Meyer, S. Meyer, S. Palutke, P. Feulner, K. Uhlig, M. Martins, and W. Wurth, “New experimental perspectives for soft x-ray absorption spectroscopies at ultra-low temperatures below 50 mK and in high magnetic fields up to 7 T”, *Rev. Sci. Instrum.* **87**, 045116 (2016) <https://doi.org/10.1063/1.4947516>.
- [70] J. Viehhaus, F. Scholz, S. Deinert, L. Glaser, M. Ilchen, J. Seltmann, P. Walter, and F. Siewert, “The variable polarization XUV beamline P04 at PETRA III: optics, mechanics and their performance”, *Nucl. Instrum. Methods Phys. Res. Sect. A* **710**, 151–154 (2013) <https://doi.org/10.1016/j.nima.2012.10.110>.
- [71] F. Pobell, *Matter and Methods at Low Temperatures*, 3rd ed. (Springer Berlin Heidelberg New York, 2007).
- [72] Y. Zhang, J. R. G. Evans, and S. Yang, “Corrected values for boiling points and enthalpies of vaporization of elements in handbooks”, *Journal Chem. Eng. Data* **56**, 328–337 (2011) <https://doi.org/10.1021/je1011086>.
- [73] J. E. Jensen, W. A. Tuttle, R. B. Stewart, H. Brechna, and A. G. Prodel, *Brookhaven National Laboratory selected cryogenic data notebook: Volume 1, Sections 1-9*, tech. rep. (Brookhaven National Laboratory, 1980).
- [74] H. Franz, O. Leupold, R. Röhlsberger, S. Roth, O. Seeck, J. Spengler, J. Stempffer, M. Tischer, J. Viehhaus, E. Weckert, and T. Wroblewski, “Technical Report: PETRA III: DESY’s New High Brilliance Third Generation Synchrotron Radiation Source”, *Synchrotron Radiat. News* **19**, 25–29 (2006) <https://doi.org/10.1080/08940880601064984>.

- [75] G. Margaritondo, “A Primer in Synchrotron Radiation: Everything You Wanted to Know about SEX (Synchrotron Emission of X-rays) but Were Afraid to Ask”, *J. Synchrotron Rad.* **2**, 148–154 (1995) <https://doi.org/10.1107/S0909049595001701>.
- [76] T. Tanaka, Y. Kida, R. Kinjo, T. Togashi, H. Tomizawa, S. Hashimoto, S. Miyamoto, S. Okabe, and Y. Tanaka, “Development of an undulator with a variable magnetic field profile”, *J. Synchrotron Rad.* **28**, 404–409 (2021) <https://doi.org/10.1107/S1600577521000989>.
- [77] S. Malerz, H. Haak, F. Trinter, A. B. Stephansen, C. Kolbeck, M. Pohl, U. Hergenhahn, G. Meijer, and B. Winter, “A setup for studies of photoelectron circular dichroism from chiral molecules in aqueous solution”, *Rev. Sci. Instrum.* **93**, 015101 (2022) <https://doi.org/10.1063/5.0072346>.
- [78] Z. Bubnicki, *Modern Control Theory*, 1st ed. (Springer Berlin Heidelberg New York, 2005).
- [79] M. Martins, K. Godehusen, T. Richter, P. Wernet, and P. Zimmermann, “Open shells and multi-electron interactions: core level photoionization of the 3d metal atoms”, *J. Phys. B* **39**, R79–R125 (2006) <https://doi.org/10.1088/0953-4075/39/5/r01>.
- [80] K. Hirsch, V. Zamudio-Bayer, J. Rittmann, A. Langenberg, M. Vogel, T. Möller, B. v. Issendorff, and J. T. Lau, “Initial- and final-state effects on screening and branching ratio in $2p$ x-ray absorption of size-selected free $3d$ transition metal clusters”, *Phys. Rev. B* **86**, 165402 (2012) <https://doi.org/10.1103/PhysRevB.86.165402>.
- [81] P. Gambardella, S. S. Dhesi, S. Gardonio, C. Grazioli, P. Ohresser, and C. Carbone, “Localized magnetic states of Fe, Co, and Ni impurities on alkali metal films”, *Phys. Rev. Lett.* **88**, 047202 (2002) <https://doi.org/10.1103/PhysRevLett.88.047202>.
- [82] H.-V. Roy, P. Fayet, F. Patthey, W.-D. Schneider, B. Delley, and C. Massobrio, “Evolution of the electronic and geometric structure of size-selected Pt and Pd clusters on Ag(110) observed by photoemission”, *Phys. Rev. B* **49**, 5611–5620 (1994) <https://doi.org/10.1103/PhysRevB.49.5611>.
- [83] J. Lau, A. Achleitner, and W. Wurth, “Electronic and geometric structure of chromium clusters deposited onto Ru(001) studied by soft X-ray absorption spectroscopy”, *Surface Science* **467**, L834–L840 (2000) [https://doi.org/10.1016/S0039-6028\(00\)00790-1](https://doi.org/10.1016/S0039-6028(00)00790-1).
- [84] A. Scherz, H. Wende, K. Baberschke, J. Minár, D. Benea, and H. Ebert, “Relation between $L_{2,3}$ XMCD and the magnetic ground-state properties for the early $3d$ element V”, *Phys. Rev. B* **66**, 184401 (2002) <https://doi.org/10.1103/PhysRevB.66.184401>.
- [85] A. Scherz, E. K. U. Gross, H. Appel, C. Sorg, K. Baberschke, H. Wende, and K. Burke, “Measuring the kernel of time-dependent density functional theory with x-ray absorption spectroscopy of $3d$ transition metals”, *Phys. Rev. Lett.* **95**, 253006 (2005) <https://doi.org/10.1103/PhysRevLett.95.253006>.

- [86] C. T. Chen, Y. U. Idzerda, H.-J. Lin, N. V. Smith, G. Meigs, E. Chaban, G. H. Ho, E. Pellegrin, and F. Sette, “Experimental Confirmation of the X-Ray Magnetic Circular Dichroism Sum Rules for Iron and Cobalt”, *Phys. Rev. Lett.* **75**, 152–155 (1995) <https://doi.org/10.1103/PhysRevLett.75.152>.
- [87] S. Fiedler, “Magnetische Momente massenselektierter CoPd und FePt legierungscluster auf Ni/Cu(100) untersucht mittels XMCD”, PhD thesis (Universität Hamburg, 2010).
- [88] P. Ohresser, N. B. Brookes, S. Padovani, F. Scheurer, and H. Bulou, “Magnetism of small Fe clusters on Au(111) studied by x-ray magnetic circular dichroism”, *Phys. Rev. B* **64**, 104429 (2001) <https://doi.org/10.1103/PhysRevB.64.104429>.
- [89] G. van der Laan, “Line shape of 2p magnetic-x-ray-dichroism spectra in 3d metallic systems”, *Phys. Rev. B* **55**, 8086–8089 (1997) <https://doi.org/10.1103/PhysRevB.55.8086>.
- [90] L. Claude, “Construction d’un microscope à effet tunnel à basse température et études d’impuretés magnétiques en surfaces”, PhD thesis (École Polytechnique Fédérale de Lausanne, 2005), <https://doi.org/10.5075/epfl-thesis-3276>.
- [91] P. Gambardella, S. Stepanow, A. Dmitriev, J. Honolka, F. M. de Groot, M. Lingenfelder, S. S. Gupta, D. Sarma, P. Bencok, S. Stanesco, et al., “Supramolecular control of the magnetic anisotropy in two-dimensional high-spin Fe arrays at a metal interface”, *Nature Mater.* **8**, 189–193 (2009) <https://doi.org/10.1038/nmat2376>.
- [92] A. Lehnert, “Magnetism of individual atoms and of epitaxial monolayers”, PhD thesis (École Polytechnique Fédérale de Lausanne, 2009), <https://doi.org/10.5075/epfl-thesis-4411>.
- [93] M. Etzkorn, C. F. Hirjibehedin, A. Lehnert, S. Ouazi, S. Rusponi, S. Stepanow, P. Gambardella, C. Tieg, P. Thakur, A. I. Lichtenstein, A. B. Shick, S. Loth, A. J. Heinrich, and H. Brune, “Comparing XMCD and DFT with STM spin excitation spectroscopy for Fe and Co adatoms on Cu₂N/Cu(100)”, *Phys. Rev. B* **92**, 184406 (2015) <https://doi.org/10.1103/PhysRevB.92.184406>.
- [94] T. Balashov, T. Schuh, A. F. Takács, A. Ernst, S. Ostanin, J. Henk, I. Mertig, P. Bruno, T. Miyamachi, S. Suga, and W. Wulfhekel, “Magnetic anisotropy and magnetization dynamics of individual atoms and clusters of Fe and Co on Pt(111)”, *Phys. Rev. Lett.* **102**, 257203 (2009) <https://doi.org/10.1103/PhysRevLett.102.257203>.
- [95] P. Błoński, A. Lehnert, S. Denler, S. Rusponi, M. Etzkorn, G. Moulas, P. Bencok, P. Gambardella, H. Brune, and J. Hafner, “Magnetocrystalline anisotropy energy of Co and Fe adatoms on the (111) surfaces of Pd and Rh”, *Phys. Rev. B* **81**, 104426 (2010) <https://doi.org/10.1103/PhysRevB.81.104426>.
- [96] A. Lehnert, S. Rusponi, M. Etzkorn, S. Ouazi, P. Thakur, and H. Brune, “Magnetic anisotropy of Fe and Co adatoms and Fe clusters magnetically decoupled from Ni₃Al(111) by an alumina bilayer”, *Phys. Rev. B* **81**, 104430 (2010) <https://doi.org/10.1103/PhysRevB.81.104430>.

- [97] V. Stepanyuk, W. Hergert, P. Rennert, K. Wildberger, R. Zeller, and P. Dederichs, “Metamagnetic states of 3d nanostructures on the Cu(001) surface”, *J. Magn. and Magn. Mater.* **165**, 272–274 (1997) [https://doi.org/10.1016/S0304-8853\(96\)00527-6](https://doi.org/10.1016/S0304-8853(96)00527-6).
- [98] B. Lazarovits, L. Szunyogh, P. Weinberger, and B. Újfalussy, “Magnetic properties of finite Fe chains at fcc Cu(001) and Cu(111) surfaces”, *Phys. Rev. B* **68**, 024433 (2003) <https://doi.org/10.1103/PhysRevB.68.024433>.
- [99] V. Zamudio-Bayer, K. Hirsch, A. Langenberg, A. Ławicki, A. Terasaki, B. v. Issendorff, and J. T. Lau, “Electronic ground states of Fe²⁺ and Co²⁺ as determined by x-ray absorption and x-ray magnetic circular dichroism spectroscopy”, *J. Chem. Phys.* **143**, 244318 (2015) <https://doi.org/10.1063/1.4939078>.
- [100] O. Hübner and J. Sauer, “Confirmation of $^9\Sigma_g^-$ and $^8\Sigma_u^-$ ground states of Fe₂ and Fe₂⁻ by CASSCF/MRCI”, *Chem. Phys. Lett.* **358**, 442–448 (2002) [https://doi.org/10.1016/S0009-2614\(02\)00673-5](https://doi.org/10.1016/S0009-2614(02)00673-5).
- [101] C. Kittel, *Einführung in die Festkörperphysik* (Oldenbourg Verlag, 2006).
- [102] G. Rollmann, H. C. Herper, and P. Entel, “Electron correlation effects in the Fe dimer”, *J. Phys. Chem. A* **110**, 10799–10804 (2006) <https://doi.org/10.1021/jp061794s>.
- [103] M. S. Dresselhaus, G. Dresselhaus, and A. Jorio, *Group theory: application to the physics of condensed matter* (Springer Berlin Heidelberg, 2007).
- [104] S. Chrétien and D. R. Salahub, “Kohn-Sham density-functional study of low-lying states of the iron clusters Fe_n⁺/Fe_n/Fe_n⁻ ($n = 1 - 4$)”, *Phys. Rev. B* **66**, 155425 (2002) <https://doi.org/10.1103/PhysRevB.66.155425>.
- [105] R. Allenspach and A. Bischof, “Magnetization direction switching in Fe/Cu(100) epitaxial films: temperature and thickness dependence”, *Phys. Rev. Lett.* **69**, 3385–3388 (1992) <https://doi.org/10.1103/PhysRevLett.69.3385>.
- [106] J. Thomassen, F. May, B. Feldmann, M. Wuttig, and H. Ibach, “Magnetic live surface layers in Fe/Cu(100)”, *Phys. Rev. Lett.* **69**, 3831–3834 (1992) <https://doi.org/10.1103/PhysRevLett.69.3831>.
- [107] D. Li, M. Freitag, J. Pearson, Z. Q. Qiu, and S. D. Bader, “Magnetic phases of ultra-thin Fe grown on Cu(100) as epitaxial wedges”, *Phys. Rev. Lett.* **72**, 3112–3115 (1994) <https://doi.org/10.1103/PhysRevLett.72.3112>.
- [108] W. L. O’Brien, B. P. Tonner, G. R. Harp, and S. S. P. Parkin, “Experimental investigation of dichroism sum rules for V, Cr, Mn, Fe, Co, and Ni: Influence of diffuse magnetism”, *J. Appl. Phys.* **76**, 6462–6464 (1994) <https://doi.org/10.1063/1.358224>.
- [109] Y. Huttel, G. van der Laan, C. M. Teodorescu, P. Bencok, and S. S. Dhesi, “Magnetic V embedded in copper evidenced by x-ray magnetic circular dichroism”, *Phys. Rev. B* **67**, 052408 (2003) <https://doi.org/10.1103/PhysRevB.67.052408>.
- [110] S. E. Weber, B. K. Rao, P. Jena, V. S. Stepanyuk, W. Hergert, K. Wildberger, R. Zeller, and P. H. Dederichs, “Magnetism of free and supported vanadium clusters”, *J. Phys.: Condens. Matter* **9**, 10739–10748 (1997) <https://doi.org/10.1088/0953-8984/9/48/016>.

- [111] D. Moore, O. Ozturk, F. Schumann, S. Morton, and G. Waddill, “Ultrathin vanadium films on Cu(001): structure and magnetism”, *Surf. Sci.* **449**, 31–42 (2000) [https://doi.org/10.1016/S0039-6028\(99\)01249-2](https://doi.org/10.1016/S0039-6028(99)01249-2).
- [112] H. Akoh and A. Tasaki, “Appearance of magnetic moments in hyperfine particles of vanadium metal”, *J. Phys. Soc. Jpn.* **42**, 791–795 (1977) <https://doi.org/10.1143/JPSJ.42.791>.
- [113] F. Liu, S. N. Khanna, and P. Jena, “Magnetism in small vanadium clusters”, *Phys. Rev. B* **43**, 8179–8182 (1991) <https://doi.org/10.1103/PhysRevB.43.8179>.
- [114] E. M. Spain, J. M. Behm, and M. D. Morse, “The 846 nm $A'{}^3\Sigma_u^- \leftarrow X^3\Sigma_g^-$ band system of jet-cooled V2”, *J. Chem. Phys.* **96**, 2511–2516 (1992) <https://doi.org/10.1063/1.462002>.
- [115] A. M. James, P. Kowalczyk, E. Langlois, M. D. Campbell, A. Ogawa, and B. Simard, “Resonant two photon ionization spectroscopy of the molecules V2, VNb, and Nb2”, *J. Chem. Phys.* **101**, 4485–4495 (1994) <https://doi.org/10.1063/1.468462>.
- [116] G. L. Gutsev, M. D. Mochena, P. Jena, C. W. Bauschlicher, and H. Partridge, “Periodic table of 3d-metal dimers and their ions”, *J. Chem. Phys.* **121**, 6785–6797 (2004) <https://doi.org/10.1063/1.1788656>.
- [117] D. S. Yang and P. A. Hackett, “Zeke spectroscopy of free transition metal clusters”, *J. Electron Spectrosc. Relat. Phenom.* **106**, 153–169 (2000) [https://doi.org/10.1016/S0368-2048\(99\)00073-0](https://doi.org/10.1016/S0368-2048(99)00073-0).
- [118] G. L. Miessler, P. J. Fischer, and D. A. Tarr, *Inorganic chemistry*, 5th ed. (Pearson, 2014).
- [119] H. Grönbeck and A. Rosén, “Geometric and electronic properties of small vanadium clusters: a density functional study”, *J. Chem. Phys.* **107**, 10620–10625 (1997) <https://doi.org/10.1063/1.474177>.
- [120] A. H. Pakiari and F. Eshghi, “Geometric and electronic structures of vanadium sub-nano clusters, Vn (n = 2-5), and their adsorption complexes with CO and O2 ligands: a DFT-NBO study”, *Phys. Chem. Res.* **5**, 601–615 (2017) <https://doi.org/10.22036/pcr.2017.80624.1364>.
- [121] A. Diaz-Bachs, M. I. Katsnelson, and A. Kirilyuk, “Kramers degeneracy and relaxation in vanadium, niobium and tantalum clusters”, *New J. Phys.* **20**, 043042 (2018) <https://doi.org/10.1088/1367-2630/aab5ca>.
- [122] S. Lounis, “Non-collinear magnetism induced by frustration in transition-metal nanostructures deposited on surfaces”, *J. Phys.: Condens. Matter.* **26**, 273201 (2014) <https://doi.org/10.1088/0953-8984/26/27/273201>.
- [123] S. Lounis, M. Reif, P. Mavropoulos, L. Glaser, P. H. Dederichs, M. Martins, S. Blügel, and W. Wurth, “Non-collinear magnetism of Cr nanostructures on Fe_{3ML}/Cu(001): first principles and experimental investigations”, *EPL (Europhysics Letters)* **81**, 47004 (2008) <https://doi.org/10.1209/0295-5075/81/47004>.

- [124] L. Kipgen, M. Bernien, S. Ossinger, F. Nickel, B. A. J., L. M. Arruda, H. Naggert, C. Luo, C. Lotze, H. Ryll, F. Radu, E. Schierle, E. Weschke, F. Tuczerk, and W. Kuch, “Evolution of cooperativity in the spin transition of an iron(II) complex on a graphite surface”, *Nature Communications* **9**, 2984 (2018) <https://doi.org/10.1038/s41467-018-05399-8>.
- [125] C. Cartier dit Moulin, P. Rudolf, A. M. Flank, and C. T. Chen, “Spin transition evidenced by soft x-ray absorption spectroscopy”, *J. Phys. Chem.* **96**, 6196–6198 (1992) <https://doi.org/10.1021/j100194a021>.
- [126] A. Hauser, P. Adler, S. Deisenroth, P. Gütlich, C. Hennen, H. Spiering, and A. Vef, “Intersystem crossing in Fe(II) coordination compounds”, *Hyperfine Interact.* **90**, 77 (1994) <https://doi.org/10.1007/BF02069119>.
- [127] A. Desaix, O. Roubeau, J. Jęftic, J. G. Haasnoot, K. Boukheddaden, E. Coddjovi, J. Linares, M. Noguès, and F. Varret, “Light-induced bistability in spin transition solids leading to thermal and optical hysteresis”, *Eur. Phys. J. B* **6**, 183–193 (1998) <https://doi.org/10.1007/s100510050540>.
- [128] J. Chen, D. J. Huang, A. Tanaka, C. F. Chang, S. C. Chung, W. B. Wu, and C. T. Chen, “Magnetic circular dichroism in Fe 2*p* resonant photoemission of magnetite”, *Phys. Rev. B* **69**, 085107 (2004) <https://doi.org/10.1103/PhysRevB.69.085107>.
- [129] R. Shan, J. Lv, and H. S. Wu, “Structural, electronic and magnetic properties of small FemVn ($m + n \leq 6$) clusters: first-principles calculation”, *Int. J. Modern Phys. B* **32**, 1850295 (2018) <https://doi.org/10.1142/S0217979218502958>.
- [130] P. Fuchs, K. Totland, and M. Landolt, “Induced magnetization in thin epitaxial V films on Fe (100)”, *Phys. Rev. B* **53**, 9123–9126 (1996) <https://doi.org/10.1103/PhysRevB.53.9123>.
- [131] M. M. Schwickert, R. Coehoorn, M. A. Tomaz, E. Mayo, D. Lederman, W. L. O’Brien, T. Lin, and G. R. Harp, “Magnetic moments, coupling, and interface interdiffusion in Fe/V(001) superlattices”, *Phys. Rev. B* **57**, 13681–13691 (1998) <https://doi.org/10.1103/PhysRevB.57.13681>.
- [132] M. Farle, A. N. Anisimov, K. Baberschke, J. Langer, and H. Maletta, “Gyromagnetic ratio and magnetization in Fe/V superlattices”, *Europhys. Lett.* **49**, 658–664 (2000) <https://doi.org/10.1209/epl/i2000-00201-y>.
- [133] A. Bergman, L. Nordström, A. B. Klautau, S. Frota-Pessôa, and O. Eriksson, “Non-collinear magnetisation of V clusters supported on a Cu(111) surface: Theory”, *Surf. Sci.* **600**, 4838–4842 (2006) <https://doi.org/10.1016/j.susc.2006.08.004>.
- [134] A. Bergman, L. Nordström, A. Burlamaqui Klautau, S. Frota-Pessôa, and O. Eriksson, “Magnetic structures of small Fe, Mn, and Cr clusters supported on Cu(111): Non-collinear first-principles calculations”, *Phys. Rev. B* **75**, 224425 (2007) <https://doi.org/10.1103/PhysRevB.75.224425>.

Acknowledgements

The days of the secluded and solitary physicist are long past and a thesis such as this one is impossible without the work of a lot of people. While I might be the one writing this down, I want to take the opportunity to mention the people that have, in various forms, contributed significantly to this work.

First of all, I want to thank Wilfried Wurth for giving me this opportunity and creating an amazing and warm work environment. His great knowledge in all things physics was something to strive for, as was his kind attitude. He taught me that one should stop and ponder explanations and theories to check them for their assumptions and validity at any given instant, no matter how often they were repeated and by whom. It saddens me deeply that he can not witness the end of the path this thesis took. You will be greatly missed.

Michael Martins, for introducing me to the world of cluster physics and of course for being my supervisor during this thesis. For letting me pursue leads and ideas, however far fetched they might have appeared. Your first instinct was to always say: "sounds promising, you should try it." and you live that for yourself as well, which made working with you and following your vision very easy.

I want to thank Ivan Baev for teaching me the things that go into the work of a scientist and that one can not find in books, like the hands-on of operating an experimental chamber, especially an UHV one. Every single beamtime I have been a part of during the years of my thesis have been with you, and in every single one of them you managed to surprise me and teach me something invaluable. Your dedication was almost as inspiring as witnessing you do something completely unorthodox and succeeding. You kept pushing the boundaries of what setups can deliver and that made a lot of measurements possible in the first place. Your coffee helped a lot, too.

I would like to thank Torben Beeck for building this wonderful setup and for taking me in at the start of my master thesis, where this journey began. Your quick thinking helped us through many night shifts and your abilities at the kicker table are unmatched in the group. Taking over the HFK after you left was no easy task, but I hope I managed.

"Physiker haben tolle Ideen, Ingenieure stellen sicher, dass das Ganze auch einen Wirkungsgrad hat." With this, I would like to thank Sven Gieschen and Holger Meyer for all their work in making sure that the wild ideas of a group of physicists become efficient, or even become reality at all. Not only your hard work but also your input and the long talks turned the beamtimes into successes.

A big thank you has to go to Marlis Fölck, who handled all the administrative work in a way that none of us could remotely achieve. Believe me, we tried, it was horrible. On top of that I want to thank you for being an amazingly warm and caring person, who made sure that we look after ourselves and reminded us that there still were leftover holidays we could take.

I want to thank Steffen Palutke and Dmytro Kutnyakhov for sacrificing their nights to help

out during beamtimes, even though that was not even close to their projects. Karolin Baev for reminding me to see the big picture behind the everyday calculations and analysis and think about what it all means at the end of the day. Also, for all of the great talks we had during and after lunch.

I would like to thank Julius Schwarz and Matz Nissen for their help with the experiments and for the discussions we had, be it about physics or about completely unrelated things (*2001: A Space Odyssey* is still a masterpiece, Julius). Also thank you for indulging in my sometimes weird sense of humor, at slightly unreasonable times.

All the people mentioned thus far have in common that they are (or were) part of the work group, but they of course do not make up all of the group. I want to thank Friederike Albrecht, Adrian Benz, Deniza Chekrygina, Michael Heber, Florian Hieke, Stephan Klumpp, Giuseppe Mercurio, Christina Ossig, Federico Pressacco, Simon Reinwardt, Lukas Wenthaus and Nils Wind for always making it a pleasure to come to work. The relaxed atmosphere and the endless talks during lunch or coffee breaks were very fruitful, but more importantly, they always were fun and welcoming.

I want to thank Moritz Hoesch, Jens Viefhaus, Jörn Seltman, Frank Scholz, Jens Buck, Florian Trinter and everyone at the P04 beamline I might have forgotten. As a user, I always felt well treated and taken care of, and your incessant work ensured smooth operation of the beamline and successful beamtimes.

I am grateful for Prof. Nils Huse agreeing to review this thesis on such a short notice. I also want to thank him, Prof. Ralf Röhlberger and Prof. Michael Rübhausen for being member of my thesis defense committee. A special thank is in order for Prof. Michael Potthoff for taking up the mantle of head of said committee.

I want to thank Simon Dörner, Niklas Lucht, Jan-Hendrik Rüscher, Alexander Fröhlich and Kaja Schubert for their help in keeping me, relatively, sane while writing a PhD thesis during a global pandemic. And before, and hopefully after.

A huge thank you goes to my family, especially my parents who sparked my curiosity when I was little and set me on the path to become a researcher at some point. At times when I doubted my choice, you showed me how proud of what I had already achieved, and that kept me going.

My deepest gratitude goes to Nauka, the wonderful woman by my side. During this work, before, and hopefully for a lifetime to come. Without your support, I would not have stood a chance to do this, not during the beamtimes and certainly not during the process of writing this thesis. I owe you more than I can ever repay, but I will try.

Eidesstattliche Erklärung / Declaration on oath

Hiermit versichere ich an Eides statt, die vorliegende Dissertationsschrift selbst verfasst und keine anderen als die angegebenen Hilfsmittel und Quellen verwendet zu haben.

Hamburg, den 14.02.2022

Unterschrift der Doktorandin / des Doktoranden